

POLITECNICO DI TORINO

DOCTORAL SCHOOL

Ph.D IN FLUID DYNAMICS - XVI Cycle

THESIS

**Perturbation dynamics in laminar and  
turbulent flows. Initial value problem analysis**



Francesca De Santi

**Advisor**  
Prof. Daniela Tordella

March 2015

# Contents

<b>Introduction</b>	<b>2</b>
<b>I Laminar flows</b>	<b>4</b>
<b>1 Linear stability analysis of sheared flow</b>	<b>5</b>
1.1 Perturbed flow and linearized disturbance equations . . . . .	7
1.2 Modal analysis . . . . .	12
1.2.1 Three-dimensionality and Squires theorem . . . . .	13
1.3 Transient dynamics and Initial value problem . . . . .	14
1.4 Perturbative analysis . . . . .	16
1.5 Numerical method . . . . .	17
<b>2 Two dimensional base flow</b>	<b>20</b>
2.1 Physical problem . . . . .	22
2.2 Dispersive to non dispersive transition . . . . .	23
2.2.1 The energy equation . . . . .	25
2.3 Phase velocity transient dynamics . . . . .	27
2.4 Acceleration-deceleration general scheme . . . . .	32
<b>3 Intermediate transient</b>	<b>35</b>
3.1 Intermediate transient . . . . .	36
3.2 Scaling propriety inside the intermediate transient . . . . .	37
3.3 Power law scaling of the energy spectrum . . . . .	41
<b>4 Cross Flow Boundary Layer</b>	<b>46</b>
4.1 Physical Problem . . . . .	48
4.1.1 Mean flow configurations . . . . .	48
4.1.2 Initial-value problem and modal analysis . . . . .	52
Codes Validation and confirmation of previous results . . . . .	52

---

4.2	Transient dynamics and role of the obliquity angle . . . . .	53
4.3	Long-term behaviour . . . . .	56
4.4	Perturbed pressure transient . . . . .	59
<b>Conclusions - Part I</b>		<b>62</b>
<b>II Stratified turbulent flows</b>		<b>66</b>
<b>5</b>	<b>Stratified flows</b>	<b>67</b>
5.1	The Boussinesq approximation . . . . .	68
5.2	Density vertical variation and fluid motion . . . . .	72
5.2.1	The Froude number . . . . .	73
<b>6</b>	<b>Transition to turbulence from counter-rotating vortex pair in a stratified fluid</b>	<b>77</b>
6.1	Rationale and state of the art . . . . .	79
6.2	Methods . . . . .	80
6.3	The Zig-Zag instability . . . . .	82
6.4	Vertically shifted perturbation and second instability . . . . .	86
6.5	Concluding remarks and future work . . . . .	91
<b>7</b>	<b>Turbulent mixing in stratified flows. An application to cloud dynamics</b>	<b>93</b>
7.1	Rationale . . . . .	95
7.2	The physical problem . . . . .	98
7.3	Results . . . . .	102
7.3.1	The onset of a kinetic energy pit . . . . .	103
7.3.2	Entrainment . . . . .	104
7.4	Conclusion . . . . .	105
<b>Concluding Remarks</b>		<b>108</b>
<b>Bibliography</b>		<b>111</b>

# Abstract

Stability and turbulence are often studied as separate branches of fluid dynamics, but they are actually the two faces of the same coin: the existence of equilibrium, laminar in one case and steady in the mean in the other. The link between these two faces is transition. Initial value problems are considered to analyse the dynamics of disturbances in the three phases.

In the context of stability, linearised equations of motion can be used. Although this is a substantial simplification, the results that are obtained with this analysis are far from being trivial. The transition to turbulence through the dynamics of disturbances is discussed in the context of the zig-zag instability: a particular kind of instability that occurs in geophysical flows. Eventually, the perturbations dynamics in turbulent flows is used to analyse the mixing process between water-vapour in clouds and clear air in the surroundings, in the presence of a meteorological inversion.

# Introduction

The evolution of the spatial-temporal perturbations is a topic of interest for most physical systems. From a physical point of view, in fact, disturbances are always present in reality and can not be eliminated or ignored, whether or not they are infinitesimal. Is therefore essential to study their spatial-temporal evolution in the two main flow regimes: laminar and turbulent.

Stability, transition and turbulence are often studied as separate strands of fluid dynamics. Stability and turbulence are actually faces of the same coin. The existence of equilibrium: in one case is laminar, in the other one is steady in the mean. The link between these two faces is transition. In this thesis initial value problems are solved in order to analyse the dynamics of disturbances acting in these three different phases.

In the context of stability, assuming that the velocity and pressure of the perturbations are small in comparison to those of the main flow, it is possible to use the linearised motion equations. In this way the physics is significantly simplified since the interactions between disturbances co-existing in the system (including the self- interaction) and those between the disturbances and the base flow are neglected. Although this is a substantial simplification, the results that are obtained with this analysis are far from being trivial. The transients can be very complex: for example the perturbation can initially lose kinetic energy, subsequently be amplified for a long time-interval and eventually completely decay when the asymptotic state is reached. This is just one of the possible scenarios that may occur by introducing travelling waves as perturbations in different types of shear flows: two-dimensional bounded (Poiseuille flow) or unbounded (Blasius boundary layer and wake flows) and three-dimensional (boundary layer in cross flow).

When the base flow is two-dimensional, the temporal evolution of the perturbative waves is analysed in terms of the velocity at which the phase of any one frequency component of the wave travels, this is named the phase velocity. This has been poorly investigated so far. Indeed traditional studies are mostly interested in identify whether a perturbation can be stable or not. However, also the phase velocity can lead to interesting considerations. In fact, generally in laminar system more than a disturbance can coexist at the same time and therefore wave packets can form. The two main features that describe the dynamics of wave packets are precisely the phase velocity and the group velocity, the velocity with which the overall shape of the waves' amplitudes propagates through space. The relation between these velocities gives

us information about how the energy is "transported" by the packet.

Always under the (realistic) assumption that at any moment in the laminar system can coexist many small perturbations that evolve independently from each other is also interesting to investigate how the energy is distributed between the different length scales and how much it differs from the case of fully developed turbulence.

When in turns a three-dimensional the base flow is considered the direction in which the disturbance propagates plays a fundamental role in determining its evolution in the transient as well as the asymptote.

The transition to turbulence through the dynamics of disturbances can be studied in the context of the zig-zag instability, which is a particular kind of instability that can occur by perturbing two counter-rotating columns vortex in the presence of a stable stratification. The vortices are stretched and bended in such a way as to assume a zig-zag shape. This zig-zag shape in turn favours the occurrences of a second instability, the Kelvin Helmholtz instability, which leads to the formation of smaller scales. This brings us to a turbulent regime. Analysing this flow, we wondered if it is possible to explain and model the obtained inhomogeneous, anisotropic and stratified turbulence.

Eventually we analyse the perturbations dynamics in a turbulent stratified flow where the stratification is expressed in terms of temperature. A particular initial condition on the temperature fluctuation is imposed such as to be able to represent an inversion layer that is a deviation from the normal change of the atmospheric temperature with altitude. An inversion layer can lead to pollution such as smog being trapped close to the ground, with possible adverse effects on health. An inversion can also suppress convection by acting as a "cap." and it can deeply modify the interaction between the clouds and the surrounding air.

We try to model this physical problem by study the flow generated by the juxtaposition of two turbulent regions that have different kinetic energy. In the region with the highest kinetic energy a concentration of passive scalar is also introduced in order to represent the water vapour inside the clouds.

The thesis is divided into two main sections. It will first consider laminar flows. A brief introduction on laminar stability analysis of sheared flows will be given in Chapter 1. The asymptotic and the transient evolution of three dimensional travelling waves acting on two dimensional base flow will be discussed in Chapter 2. In Chapter 3, it will then go on to describe a particular time interval which is common in all transients and in which interesting scaling properties are observed. The case where the base flow is three-dimensional will be treated in Chapter 4. Some conclusions on the perturbation dynamics in laminar flows will follow.

The second part will concern stratified flows. A brief introduction about these flows will be in Chapter 5. The transition to turbulence that may result from the zig-zag instability will be discussed in Chapter 6; while turbulent mixing through a temperature inversion layer will be discussed in Chapter 7.

Finally, general concluding remarks will follow.

**Part I**

**Laminar flows**

## Chapter 1

# Linear stability analysis of sheared flow: history, mathematical framework and rationale

The hydrodynamic stability of fluid flow is an important subject in different fields, such as aerodynamics, mechanics, astrophysics, oceanography, atmospheric sciences, and biology. Stability can be defined as the ability of a dynamical system to be immune to small disturbances [10]. In general, a system excited with infinitesimal perturbations is considered stable if the initial state of equilibrium, in the short or long term, is reached again. On the contrary, a system is unstable if, subject to small oscillations, it departs from any state of equilibrium.

The central issue of the stability analysis is to understand the underlying reasons for the breakdown of laminar flow and its subsequent transition to turbulence. Although many improvements have been made over a hundred years, this remains an open question and a definitive means for prediction is still to be found.

The fundamental property of linearity has been often applied in literature to the stability analysis of flows. Disturbances superposed on the laminar flow are assumed to be small so that perturbation higher order terms are negligible, and this implies a simplification of the governing equations. Moreover, from a physical point of view, the assumption of small disturbances is supported by the fact that these infinitesimal oscillations are always present in a dynamical system and cannot be eliminated.

Anyhow, as the disturbance velocity grows, non-linear effects become important and the linear equations no longer accurately predict the perturbation evolution. Although the linear theory is important in identifying the onset and a possible development of the instability, but not in considering its following evolution. Indeed, when a perturbation sets in, after a possible initial transient growth, it shows an exponential behaviour. However, the subsequent temporal evolution is modified by the non-linear dynamics. This interaction makes the perturbations assume



a behaviour which is no longer exponential.

First important contributions to the hydrodynamic stability are due to Helmholtz [54], Kelvin [64, 65] and Rayleigh [114]. In the early twentieth century, independently, Orr [107, 108] and Sommerfeld [128] framed the basis of the normal mode theory. Although the stability has been widely recognized as an initial-value problem, for several years the attention was mainly focused on the final fate of disturbances imposed. It was considered sufficient to know whether or not a flow is asymptotically stable or unstable. In this context, normal mode analysis turns out to be a powerful and synthetic means to predict the perturbation asymptotic behaviour.

Only lately the transient growth has become of great interest and its importance for the complete temporal evolution of the perturbed system has been widely accepted. Recent shear flows studies have shown that instability can be due to transient growth of disturbances [21, 28] long before the growing exponential mode occurs. In principle, this kind of behaviour could cause perturbation amplitude that violates the assumption of linearity and promote rapid transition, phenomenon known as bypass transition. An example of this possible scenario is represented by the pipe flow. Linear modal analysis assures stability for all the Reynolds numbers [36], but this result is in contrast with the experimental evidence, which shows that the flow becomes turbulent at sufficiently large Reynolds numbers. The disagreement between the linear modal prediction and laboratory results has motivated several recent works [38, 57, 37] that focus on transient travelling waves and their link to the transition process. In general, it is now considered possible that inside the transient life of travelling waves some important events for the stability of the flow can take place.

The present work is developed within the linear theory framework and the laminar flows here considered for the stability analysis are:

- the two-dimensional wake past an infinite circular cylinder,
- the plane Poiseuille flow,
- the Cross-flow boundary layer.

These flows are an important prototype of free shear flow for the study as well as for the applications in environmental, engineering and biological fluid dynamics.

The interest is focused on the behaviour of disturbances through both normal mode analysis and an initial-value problem to capture the early transient as well as the asymptotic behaviour of any disturbance initially imposed. The common aspect to both these analyses is the base flow description. The fundamental aspect of the normal mode approach is the assumption of an exponential time dependence, which allows the transformation of the linear initial-value problem into a corresponding eigenvalue problem. This hypothesis yields the temporal asymptotic behaviour, once the most unstable mode is established, but is lacking information on the

transient growth. On the contrary, the initial-value problem formulation for the stability analysis proposed by Criminale and Drazin [28] does not provide any a priori evolution in time, and the governing equations are expressed in terms of partial differential equations. In like fashion, the temporal evolution of disturbances initially imposed can be observed at any time.

As a very preliminary comment, the normal mode analysis turns out to be a powerful and synthetic approach to observe whether or not a flow is asymptotically stable or unstable. In the initial-value problem formulation both the early transient growth as well as the asymptotic behaviour are directly taken into account. However, the latter approach is less concise than the modal analysis, as different parameters have to be considered. In next chapters both the approach will be used to perform a perturbative analysis on typical two- and three-dimensional base flows.

In the following section the linear stability analysis is introduced for two-dimensional viscous incompressible steady parallel flows. In section 1.2 it is carried on through the modal analysis, while the transient dynamics is treated in section 1.3. The physical quantities needed to describe the perturbations evolution are introduced in section 1.4. In section 1.5 the numerical methods are discussed.

## 1.1 Perturbed flow and linearized disturbance equations

Stability theory uses perturbation analysis in order to test whether or not the equilibrium flow is unstable. Consider the flows that are incompressible, time independent and parallel or almost parallel by defining the mean state in Cartesian coordinate as

$$\left\{ \begin{array}{l} U = U(y) \\ V = 0 \\ W = 0 \\ P = P(x, y, z) \end{array} \right.$$

where  $U(y)$  is the  $x$  direction with  $y$  the coordinate that defines the variation of the mean flow,  $z$  is in the transverse direction and  $P$  is the mean pressure. For some flows, such as that of channel flow, this result is exact; for the case of boundary layer or unbounded flows then this is only an approximation but the  $U$  component of the velocity is such that  $U \gg V, W$  and  $U$  varying only weakly with  $x$ , and then the designation of almost parallel flow. For the sake of simplicity here we refer only to bounded flow where both  $x$  and  $z$  range from minus to plus infinity with  $y$  giving the location of the solid boundaries.  $P$  is the mean pressure and the density is taken a constant.

In particular, in this thesis the channel base flow is represented by the plane Poiseuille solution

$$U(y) = 1 - y^2. \quad (1.1)$$

As a wake basic flow, we use the first two order terms of the Navier–Stokes asymptotic solution described in [136] and reported below:

$$U(y; x_0, Re) = C_0 - \frac{1}{\sqrt{x_0}} C_1 e^{-Re y^2/(4x_0)} \quad (1.2)$$

where  $C_0 = 1$  and  $C_1 = 1.22 + 0.000067Re^2$ .

Now assume that there are disturbances to this flow that are fully three dimensional, and hence

$$\begin{cases} u = U(y) + \tilde{u}(x, y, t) \\ v = \tilde{v}(x, y, t) \\ w = \tilde{w} \\ p = P(x, y) + \tilde{p}(x, y, t) \end{cases}$$

can be written for the velocity and pressure of the instantaneous flow. Here the tilde superscripts indicate fluctuation components that are small with respect to the corresponding mean system quantities ( $|\tilde{u}/U \ll 1$  and  $|\tilde{p}/P \ll 1$ ). By writing the continuity and the Navier–Stokes equations for the perturbed flow and then subtracting from these the corresponding ones for the base flow, one obtains the following equations

$$\partial_x \tilde{u} + \partial_y \tilde{v} + \partial_z \tilde{w} = 0 \quad (1.3)$$

$$\partial_t \tilde{u} + U \partial_x \tilde{u} + U' \tilde{v} + \tilde{u} \partial_x \tilde{u} + \tilde{v} \partial_y \tilde{u} + \tilde{w} \partial_z \tilde{u} + \partial_x \tilde{p} = \frac{1}{Re} \nabla^2 \tilde{u} \quad (1.4)$$

$$\partial_t \tilde{v} + U \partial_x \tilde{v} + \tilde{u} \partial_x \tilde{v} + \tilde{v} \partial_y \tilde{v} + \tilde{w} \partial_z \tilde{v} + \partial_y \tilde{p} = \frac{1}{Re} \nabla^2 \tilde{v} \quad (1.5)$$

$$\partial_t \tilde{w} + U \partial_x \tilde{w} + \tilde{u} \partial_x \tilde{w} + \tilde{v} \partial_y \tilde{w} + \tilde{w} \partial_z \tilde{w} + \partial_z \tilde{p} = \frac{1}{Re} \nabla^2 \tilde{w} \quad (1.6)$$

where  $Re$  is the the Reynolds number the dimensionless parameter that represents the ratio of inertial forces to viscous forces and consequently quantifies the relative importance of these two types of forces for given flow conditions. It is defined as

$$Re = \frac{U_{ref} L_{ref}}{\nu}$$

where  $U_{ref}$  is a typical velocity of the base flow,  $L_{ref}$  a typical length scale of the physical problem and  $\nu$  the kinematic viscosity. The symbols  $\partial_x$ ,  $\partial_y$  and  $\partial_z$  are respectively the partial derivative in the direction  $x$ ,  $y$  and  $z$ , while  $\nabla^2$  is the laplacian operator. The system of equations 1.3-1.6 has to be combine with proper initial and boundary condition. In bounded flows we impose no-slip boundary conditions, while for the wake flow uniformity at infinity

and finiteness of the energy are imposed:

$$u(\pm y_f) = v(\pm y_f) = w(\pm y_f) = 0 \quad \text{in bounded flow} \quad (1.7)$$

$$u(\pm\infty) = v(\pm\infty) = w(\pm\infty) = U_\infty \quad \text{in unbounded flow} \quad (1.8)$$

where  $\pm y_f$  are the domain limit in bounded flow and  $U_\infty$  is the undisturbed velocity in the free stream for unbounded flow. The system of equations 1.3-1.6 is non-linear with respect to the disturbance terms. The non-linear terms are products of the fluctuating velocities and their derivatives. If the oscillation has frequency  $\omega$ , these terms will have frequency 0 or  $2\omega$ . This interaction will either modify the base flow (mean-flow distortion) and feedback to the fluctuating components or introduce higher harmonics. Such difficulties are overcome with the assumption that the perturbations are small in comparison with the base flow. As a consequence the products of the fluctuations and their derivatives (the terms  $\tilde{u}\partial_x\tilde{u}$ ,  $\tilde{u}\partial_x\tilde{v}$ ,  $\tilde{u}\partial_x\tilde{w}$ ,  $\tilde{v}\partial_y\tilde{u}$ ,  $\tilde{v}\partial_y\tilde{v}$ ,  $\tilde{v}\partial_y\tilde{w}$ ,  $\tilde{w}\partial_z\tilde{u}$ ,  $\tilde{w}\partial_z\tilde{v}$  and  $\tilde{w}\partial_z\tilde{w}$ ) are negligible in comparison with the other terms as a small disturbance multiplied by a small disturbance results in a term of smaller order of magnitude and no longer influences the equations to this order of approximation.

The linear system is

$$\partial_x\tilde{u} + \partial_y\tilde{v} + \partial_z\tilde{w} = 0 \quad (1.9)$$

$$\partial_t\tilde{u} + U\partial_x\tilde{u} + U'\tilde{v} + \partial_x\tilde{p} = \frac{1}{Re}\nabla^2\tilde{u} \quad (1.10)$$

$$\partial_t\tilde{v} + U\partial_x\tilde{v} + \partial_y\tilde{p} = \frac{1}{Re}\nabla^2\tilde{v} \quad (1.11)$$

$$\partial_t\tilde{w} + U\partial_x\tilde{w} + \partial_z\tilde{p} = \frac{1}{Re}\nabla^2\tilde{w} \quad (1.12)$$

The perturbations applied to the system will evolve independently because the non-linear terms, that would permit interaction, have been neglected. The same fundamental property of linearity occurs in other fields (acoustics, electromagnetism, ...), but non-linear equations must often be retained to capture the essential physics.

Luckily, the solution of the linear system is sufficient to describe problems where small oscillations influence the base flow. Moreover, it should be reminded that the infinitesimal perturbations cannot be removed and are always present in any physical system. However, as soon as the perturbation energy grows, the non-linear equations are required to correctly capture the perturbative evolution. For this reason, only the onset and not the following temporal evolution of a possible instability is the aim of the linear stability theory.

Any velocity vector field can be decomposed into its solenoidal, rotational and harmonic component. For the problems being discussed here there is no solenoidal part due to the fact that fluid is incompressible and  $\nabla \cdot \mathbf{u} = 0$ . On physical grounds the rotational part of the veloc-

ity corresponds to the perturbation vorticity with the harmonic pressure related to the pressure. The reasoning for the decomposition of the velocity can be best understood by actually using the definitions for the divergence and the curl. First, operate on 1.10-1.12 by taking the divergence and use 1.9 to give

$$\nabla^2 \tilde{p} = -2U' \partial_x \tilde{v} \quad (1.13)$$

The relation 1.13 is an equation for the perturbation pressure and has an inhomogeneous term that is effectively a source for the pressure due to interaction of the fluctuating and mean strain rates. When neither is strained then the pressure is harmonic. If the velocity had not been solenoidal, than factors relating to the compressibility of the fluid would come into play.

Now the definition of the perturbation vorticity components are

$$\omega_x = \partial_y w - \partial_z v \quad (1.14)$$

$$\omega_y = \partial_z u - \partial_x w \quad (1.15)$$

$$\omega_z = \partial_x v - \partial_y u \quad (1.16)$$

Using this definitions and the operation of the curl on the same set of equations for the momenta, the following equations are obtained:

$$\partial_t \tilde{\omega}_x + U \partial_x \tilde{\omega}_x - \frac{1}{Re} \nabla^2 \tilde{\omega}_x = -U' \partial_x w \quad (1.17)$$

$$\partial_t \tilde{\omega}_y + U \partial_x \tilde{\omega}_y - \frac{1}{Re} \nabla^2 \tilde{\omega}_y = -U' \partial_z v \quad (1.18)$$

$$\partial_t \tilde{\omega}_z + U \partial_x \tilde{\omega}_z - \frac{1}{Re} \nabla^2 \tilde{\omega}_z = +U'' v + U' \partial_x u + U' \partial_y v \quad (1.19)$$

where  $-U' = \Omega_z$  is the single component of the mean vorticity and is in the  $z$  direction. Each of these equations has the expected transport by the mean velocity and diffusion but, in case there is also an inhomogeneous term that is due to the interaction of the fluctuating strain and the mean vorticity. Just as in the pressure relation, these interactions are needed for any generation of the respective fluctuating component. But, it is important to note, such generation here is due to three-dimensionality. If there was neither the  $w$  component of the velocity nor the spatial dependence in the transverse  $z$ -direction, as it would be for the two-dimensional problem, then the fluctuating vorticity component, except for  $\omega_z$ , could only be advected and diffused regardless of any initial input.

In order to seek a solution for this problem, the number of equations needs to be reduced. There are several ways to do this, but one in particular is more than efficient. From kinematics, it can be shown that

$$\nabla^2 \tilde{v} = \partial_x \tilde{\omega}_z - \partial_z \tilde{\omega}_x \quad (1.20)$$

Thus by combining equations 1.17 and 1.19 and using 1.20, then

$$\partial_t \nabla^2 v + U \partial_x \nabla^2 v + U'' \partial_x v = \frac{1}{Re} \nabla^2 \nabla^2 v \quad (1.21)$$

can be obtained and. Although still in a partial differential equation form equation 1.21 is the **Orr-Sommerfield equation** of stability theory. It is fortuitous that this equation uncouples in such a way as to only be fourth order and homogeneous in the  $v$  dependent variable. The solution of 1.21 is the first requirement that must be met. These solutions are then to be used in 1.18 for the solution of  $\omega_y$ . In like manner, the results found for  $\omega_y$  are combined with  $v$  and the problem is complete when these are used in 1.15 and 1.9 to determine  $u$  and  $w$ .

If proper initial data and the boundary condition are satisfied, the problem is complete and the query as to stability can now be answered.

One last observation should be noted here. Equation 1.18 is actually the **Squire equation** that is known to accompany that Orr-Sommerfield. In this form, however, the dependent variable is the component of the vorticity that is perpendicular to the  $x - z$  plane and is only of interest in the full three dimensional perturbation problem, strictly speaking.

It is recognized that the coefficient in 1.21 are function of  $y$  only. Therefore, since the extent of the planes perpendicular to  $y$  defined by  $x, z$  spatial variables is doubly infinite,  $v$  can be Laplace (Fourier) transformed in this two variables. Accordingly define

$$\hat{v}(\alpha, \gamma; y; t) = \int_{-\infty}^{\infty} \int_{-\infty}^{\infty} \tilde{v}(x, y, z, t) e^{i(\alpha x + \gamma z)} dx dz \quad (1.22)$$

where we have introduced the wavenumbers  $\alpha$  and  $\gamma$  respectively in the  $x$  and  $z$  directions. The far field boundary conditions in these directions, namely boundedness, are satisfied by the rigid conditions for the Fourier transforms with  $\alpha$  and  $\gamma$ . Although here is no general restriction to real or complex wave numbers, in this thesis we will consider the spatial wavenumbers both real. The boundary conditions in  $y$  direction in term of transversal velocity and vorticity are derived by equations 1.9, 1.18 and 1.7

$$v'(\pm y_f) + \alpha u(\pm y_f) + \gamma w(\pm y_f) = 0 \quad \rightarrow v'(\pm y_f) \quad (1.23)$$

$$\omega_y(\pm y_f) = \gamma u(\pm y_f) - \alpha w(\pm y_f) = 0 \quad (1.24)$$

Summarizing the Orr-Sommerfeld and Squire problem is described by the system of equations

$$\left\{ \begin{array}{l} (\partial_t + i\alpha U)(\partial_{yy} \hat{v} - k^2 \hat{v}) - i\alpha U'' \hat{v} = \frac{1}{Re} (\partial_{yyyy} \hat{v} - 2k^2 \partial_{yy} \hat{v} + k^4 \hat{v}) \\ (\partial_t + i\alpha U) \hat{\omega}_y + i\beta U' \hat{v} = \frac{1}{Re} (\partial_{yy} \hat{\omega}_y - k^2 \hat{\omega}_y) \\ \hat{v}(t=0) = v_0, \quad \hat{\omega}_y(t=0) = \omega_{y0} \\ \hat{v}(\pm y_f) = \hat{v}'(\pm y_f) = \hat{\omega}_y(\pm y_f) = 0 \end{array} \right. \quad (1.25)$$

where  $k = \sqrt{\alpha^2 + \gamma^2}$  is the polar wavenumber.

The governing equation are now a partial differential equation in terms of the variables  $y$  and  $t$  only.

## 1.2 Modal analysis

Traditionally, investigations of disturbances in shear flows have been characterized using classical linear stability analysis. However, instead of considering the complete temporal evolution of the perturbations and analysing the physical cause of a possible instability, the attention has been widely focused on determining whether or not the flow is asymptotically unstable. If only the question of stability is to be answered, the modal analysis is the easiest method to use.

First contributions have been given by Orr [107, 108] and Sommerfeld [128] who separately derived the now-famous Orr-Sommerfeld equation 1.21. In the framework of the modal analysis, the solution of the linearized perturbative equations turns into the resolution of an eigenvalue problem. Introducing wavelike solution of the form

$$v(x, y, z, t) = \hat{v}(y)e^{i(\alpha x + \gamma z - \sigma t)} \quad (1.26)$$

$$\omega_y(x, y, z, t) = \hat{\omega}_y(y)e^{i(\alpha x + \gamma z - \sigma t)} \quad (1.27)$$

results in the following pair of equations

$$\begin{cases} i(\alpha U - \sigma)(\partial_{yy}\hat{v} - k^2\hat{v}) - i\alpha U''\hat{v} = \frac{1}{Re}(\partial_{yyyy}\hat{v} - 2k^2\partial_{yy}\hat{v} + k^4\hat{v}) \\ i(i\alpha U - \sigma)\hat{\omega}_y + i\beta U'\hat{v} = \frac{1}{Re}(\partial_{yy}\hat{\omega}_y - k^2\hat{\omega}_y) \end{cases} \quad (1.28)$$

The frequency  $\sigma$  appears as the eigenvalue in the Orr Sommerfeld equation, and together with the associated eigenfunction  $\hat{v}$  is generally complex. The same hold true for the Squire equation. It is important to note that the Orr Sommerfeld equation is homogeneous. On the other hand, the Squire equation for the normal vorticity is forced by solutions of Orr-Sommerfeld equation. We can also write equation 1.28 in easier compact notation. We will start by introducing the vectorial quantity

$$\hat{\mathbf{q}} = \begin{pmatrix} \hat{v} \\ \hat{\omega}_y \end{pmatrix} \quad (1.29)$$

which allows us to write the Orr Sommerfeld and Squire equation in a matrix form as

$$-i\sigma \underbrace{\begin{pmatrix} k^2 - \partial_{yy} & 0 \\ 0 & 1 \end{pmatrix}}_{\mathbf{M}} \begin{pmatrix} \hat{v} \\ \hat{\omega}_y \end{pmatrix} + \underbrace{\begin{pmatrix} \mathcal{L}_{OS} & 0 \\ i\gamma U' & \mathcal{L}_{SQ} \end{pmatrix}}_{\mathbf{L}} \begin{pmatrix} \hat{v} \\ \hat{\omega}_y \end{pmatrix} = 0 \quad (1.30)$$

where

$$\mathcal{L}_{OS} = i\alpha U(k^2 - \partial_{yy}) + i\alpha U'' + \frac{1}{Re}(k^2 - \partial_{yy})^2 \quad (1.31)$$

$$\mathcal{L}_{SQ} = i\alpha U + \frac{1}{Re}(k^2 - \partial_{yy}) \quad (1.32)$$

$$(1.33)$$

Here  $\mathbf{M}$  is a positive definite operator. The generalized eigenvalue problem can be expressed in compact and recognizable form:

$$\mathbf{L}\hat{\mathbf{q}} = i\sigma\mathbf{M}\hat{\mathbf{q}} \quad (1.34)$$

The solution of 1.28 can be divided into two classes of eigenmodes:

$$\left( \begin{matrix} \hat{v}_n \\ \hat{\omega}_{y_n}^p \end{matrix} \right)_{n=1}^N \text{ OS modes} \quad \left( \begin{matrix} 0 \\ \hat{\omega}_{y_m} \end{matrix} \right)_{m=1}^M \text{ SQ modes} \quad (1.35)$$

The first class is the set of the Orr-Sommerfeld (OS) modes where  $\hat{v}_n$  and  $\sigma_n$  are found by solving the Orr-Sommerfeld equation. The corresponding normal vorticity  $\hat{\omega}_{y_n}^p$  is found by solving the inhomogeneous Squire equation with  $\hat{v}_n$  is the forcing term. The superscript  $p$  emphasizes that is equivalent of a particular solution of the driven Squire equation. The second class of eigenmodes in the set of Squire (SQ) modes where the solution of the Orr Sommerfeld equation is identically zero, implying that the squire equation is homogeneous. The two set have in general different eigenvalues.

### 1.2.1 Three-dimensionality and Squires theorem

In the framework of the normal mode theory, only two-dimensional perturbations are usually considered. This simplify the eigenvalue problem since it is reduced only in the Orr sommerfeld equation. In addition in 1933 Squire [129] recognized that through a simple transformation (now known as Squire transformation) the three-dimensional Orr-Sommerfeld equation can be reduced to the same form as the two-dimensional Orr-Sommerfeld equation.

First, this implies that a three-dimensional problem can be reduced to a two-dimensional one. Second, for parallel flows, only the two-dimensional problem has to be studied for determining stability, as two-dimensional and three-dimensional quantities are linked together



through the Squire transformation. Third, the two-dimensional and three dimensional problems have the same formulation, except that the two-dimensional problem has a lower value of the Reynolds number. Finally, the wave velocity remains unscaled for the three-dimensional and the two-dimensional problems. All these remarks are summed up in the following theorem

**Squires Theorem (1933):**

*If an exact two-dimensional parallel flow admits an unstable three-dimensional disturbance for a certain value of the Reynolds number, it also admits a two-dimensional disturbance at a lower value of the Reynolds number.*

In other words the theorem could also be stated as *The minimum Reynolds number for instability will be higher for an oblique three-dimensional wave than for a purely two-dimensional one or To each unstable three-dimensional perturbation there corresponds a two-dimensional one with a lower Reynolds number (and with a higher longitudinal wavenumber).*

Anyhow, it should be reminded that the Squire theorem only applies to parallel flows. For more complicated flows, such as three-dimensional or curved mean flows, three-dimensional perturbations have to be considered. Moreover, the theorem does not rule out the possibility that, for high enough Reynolds number, an unstable oblique oscillation can occur even though the purely two-dimensional one (with the same longitudinal wavenumber) is damped. This point was treated by Watson [147] as well as Betchov and Criminale [10], but has not been exploited to date.

### 1.3 Transient dynamics and Initial value problem

In the normal mode analysis the main goal is to determine whether or not the flow is asymptotically unstable, and therefore to find the most unstable mode, for fixed values of the parameters (e.g.  $Re$ ) is enough for the stability question to be answered. Only relative recently the transient dynamic of perturbations has become of some importance in stability theory. Since the very complexities of mathematics and the lack of adequate computing in the early stage of the development, it was piratically impossible to actually accomplish this task. At the same time, traditional thought on this matter did not indicate that this aspect could have any bearing on the ultimate behaviour and was simply ignored.

Nowadays it is quite clear that the results of stability calculation in the modal form are really more for the purpose of predicting of the finale state of any disturbance and the transient dynamics can have and do lead to events that make this part of the problem even more of interest than it ever was.

If we are interested in solve an arbitrary initial value problem, i.e the problem 1.25 with any choice of initial conditions it is done traditionally using a functions expansion. If we can find a set of solutions of the Orr-Sommerfield equation,  $\phi_i$ , that form a base in the space of the solutions then any solution can be expressed as a series expansion of these base functions and the unknowns disappear. However, the application of this procedure is not trivial: for a specific

initial-value designation, there is the question of exactly how express arbitrary functions or even what set of functions are to be used for expansion of this given initial condition.

Intuitively the set of base functions can be sought among the eigen-modes, but we must be certain that they are a base and such as able to describe any function belonging to space of solutions, namely they must be a **complete** set.

In flows with bounded domain all eigenvalues are **discrete** and infinite in number. DiPrima and Habbetler [35] showed that this set is complete. Any initial disturbance can be expanded in terms of normal modes and thus the complete solution can be expressed in terms of them. For unbounded domains, general completeness theorems do not exist. However, Miklavcic and Williams [93, 94] proved rigorously that if the mean flow decays exponentially to a constant in the free-stream, then only a finite number of eigenvalues exists for a fixed  $Re$ , while if the mean flow decays algebraically, then there exists an infinite discrete set of eigenvalues. In the first case, a **continuum** must exist for a complete set to span the space solution, while in the latter case no continuum exists.

As an alternative to modal expansion for solving the initial value problem 1.25 is the use of the Laplace transform in time as proposed by Gustavsson in boundary layer flows [49]. In this way the problem results completely specified and, in principle, can be made tractable. Unfortunately, only general properties can actually be found using this approach since the ordinary differential equation that must be solved is the same as 1.30. However, the important algebraic behaviour is shown to exist along with the exponential modes and is due to the existence of a continuous spectra since he showed that branch cuts as well as poles must exist when the inversion back to the real space is to be made. This implies the existence of a continuous spectrum and the transient behaviour associated to it [49]. Lately Grosch and Salwen [120] showed (not rigorously) that for unbounded flows the set consisting of the discrete modes and the continuum is complete. According to this result, to complete the solution the continuum part has to be included. This can be exploited considering the Orr-Sommerfeld equation with bounded solutions at infinity. For the discrete set  $\hat{v}$  and  $\hat{v}'$  are required to vanish when  $|y| \rightarrow \infty$ , while for the continuous spectrum  $\hat{v}$  and  $\hat{v}'$  are required to be bounded when  $|y| \rightarrow \infty$ . Therefore any solution of 1.25 can be written as

$$\hat{v}(\alpha, \gamma; y; t) = \sum_{n=1}^N C_n e^{i\sigma_n t} v_n(y) + V_c(y, t) \quad (1.36)$$

where  $N$  is the number of discrete eigenvalues,  $v_n$  are the eigenfunctions,  $C_n$  depends on the initial condition and  $V_c$  is the continuum. An example of continuum spectra is shown in Figure 1.2 for the Blasius Boundary layer flow. Once computed, the transient dynamic of perturbations reveals that in the early transient an algebraic behaviour is observed. It can arise for different reason. First three-dimensional perturbations the eigenfunctions are mutually non-orthogonal since the operators that describe the linearized equations 1.30 are not selfadjoint. Second, for three-dimensional perturbations, resonance between Orr-Sommerfeld equation set of solutions

and those of the Squire equation can occur. Resonance has been demonstrated to be possible for channel flow [50, 51, 7] but does not occur for the boundary layer. Resonance in the free shear flows is yet to be determined. With the unbounded flow the continuous spectrum contributes to such behaviour as well.

We have seen how the transient dynamics has been treated traditionally and how the eigenvalue problem can be associated to the transient life (we will return to better illustrate this concept in the following chapter). Indeed, although this procedure where travelling wave normal modes are assumed as solutions is mathematically correct, it is of limited use when actually studying transient behaviour because of the underlying difficulties in the expansion process once the eigenfunctions are obtained numerically. In other words the adoption of non-orthogonal eigenfunctions in the try to build any real arbitrary initial condition introduces unnecessary mathematical complications. We therefore prefer to follow the approach of Criminale [29] and use arbitrary initial conditions that can be specified without having to recur to eigenfunction expansions. Within our framework, for any initial small-amplitude three-dimensional disturbance, this method allows the determination of the complete temporal behaviour, including both the early and intermediate transients and the long-time asymptotics.

## 1.4 Perturbative analysis

To measure the growth of the perturbations, we define the kinetic energy density,

$$e(t; \alpha, \gamma) = \frac{1}{4y_f} \int_{-y_f}^{+y_f} (|\hat{u}|^2 + |\hat{v}|^2 + |\hat{w}|^2) dy, \quad (1.37)$$

where  $-y_f$  and  $y_f$  are the computational limits of the domain, while  $\hat{u}(y, t; \alpha, \gamma)$ ,  $\hat{v}(y, t; \alpha, \gamma)$  and  $\hat{w}(y, t; \alpha, \gamma)$  are the transformed velocity components of the perturbed field. For the channel flow, which is bounded, the computational limits coincide with the walls ( $y_f = 1$ ). The wake is an unbounded flow and the value  $y_f$  is defined so that the numerical solutions are insensitive to further extensions of the computational domain size ( $y_f = 20$  for short waves and  $y_f$  up to 150 for longer waves). We then introduce the amplification factor,  $G$ , as the kinetic energy density normalized with respect to its initial value,

$$G(t; \alpha, \gamma) = e(t; \alpha, \gamma) / e(t = 0; \alpha, \gamma). \quad (1.38)$$

Assuming that the temporal asymptotic behaviour of the linear perturbations is exponential, the temporal growth rate,  $r$ , that corresponds to the imaginary part of the eigenvalues of the modal analysis, can be defined as

$$r(t; \alpha, \gamma) = \log(e) / (2t). \quad (1.39)$$

The frequency,  $\omega$ , of the perturbation is defined as the temporal derivative of the unwrapped

wave phase,  $\theta(y, t; \alpha, \gamma)$ , at a specific spatial point along the  $y$  direction. The wrapped phase,

$$\theta_w(y, t; \alpha, \gamma) = \arg(\hat{v}(y, t; \alpha, \gamma)), \quad (1.40)$$

is a discontinuous function of  $t$  defined in  $[-\pi, +\pi]$ , while the unwrapped phase,  $\theta$ , is a continuous function obtained by introducing a sequence of  $2\pi$  shifts on the phase values in correspondence to the periodical discontinuities. In the case of the wake we use as reference transversal observation point  $y_0 = 1$  or  $y_0 = 5$ , and in the case of the channel flow the point  $y_0 = 0.5$ . The frequency ([122]) is thus

$$\omega(t; y_0, \alpha, \gamma) = |d\theta(t; y_0, \alpha, \gamma)|/dt \quad (1.41)$$

It corresponds to the real part of the eigenvalues of the modal analysis.

It should be noted that when  $r$  and  $\omega$  become constant, the asymptotic state is reached. In the asymptotic limit, in respect to the modal analysis, the IVP can only select the mode which has the largest growth rate.

The phase velocity is defined as

$$\mathbf{C} = (\omega/k)\hat{\mathbf{k}}, \quad (1.42)$$

where  $\hat{\mathbf{k}} = (\cos(\phi), \sin(\phi))$  is the unitary vector in the  $k$  direction, and represents the rate at which the phase of the wave propagates in space.

The eigenvalues,

$$\sigma = \sigma_r + i\sigma_i$$

and the eigenfunctions of the Orr-Sommerfield and Squire equations as defined in 1.30 are also computed.

## 1.5 Numerical method

Equations 1.25 are numerically solved in two ways: by the method of lines and, for the Poiseuille flow where the discrete spectrum is complete, also by an eigenfunction expansion method of the fifth order based on Chandrasekhar functions [23].

The method of lines [1] is a convenient numerical method: the equations are first discretized in the spatial domain using a second-order finite difference scheme, and then integrated in time. For the temporal integration we use an adaptative one-step solver, the Bogacki-Shampine method [19], which is an explicit Runge-Kutta method of order three using approximately three function evaluations per step. It has an embedded second-order method which can be used to implement adaptive step size. This method is implemented in the ode23 Matlab function [127] and is a good compromise between non-stiff solvers, which give a higher order of accuracy, and stiff solvers, which can in general be more efficient.

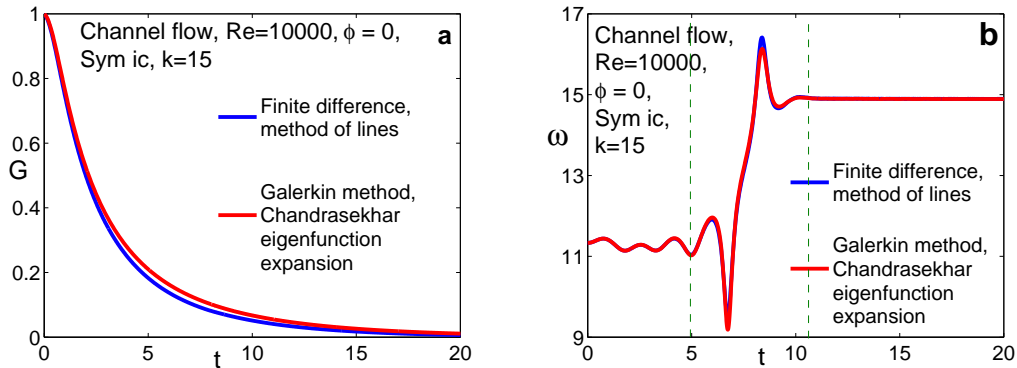


Figure 1.1: Comparison between results obtained via the finite difference method and the Galerkin method. in term of (a) amplification factor and (b) frequency of the perturbation.

In the second case, a Galerkin method is used to obtain a weak formulation based on a finite number (around 200) of modes [40]. Differently from the previous method, this one can be used only for confined flows. However the agreement between the two method is really good

Two different numerical methods are used to compute the spectra of the Orr-Sommerfeld equation. In Figure 1.2 we report a comparison with literature results as a validation of our schemes. As mentioned before, for unbounded flows it has been shown by [48] that a continuous spectrum can be analytically found, if the boundary conditions are relaxed to  $\hat{v}$  *unbounded* as  $y \rightarrow \infty$ . If homogeneous or exponential ( $\hat{\Gamma} = 0$ ) boundary conditions are imposed and therefore only the class of decaying solutions is considered, the continuous part of the spectrum is approximated in a discrete way. If the boundary conditions are imposed far from the wake, the approximation is very good. In the present work we use a finite differences scheme of fourth order of accuracy, and the Galerkin method with Chandrasekhar functions described above. The last method is here successfully adapted for the wake flow or for the boundary layer flow and refined non uniform grids have been used.

Since no spectra with our wake base flow [136] have been found in literature, the schemes have been validated with the Blasius boundary layer flow (see Figure 1.2, panel a). For channel flow, the comparison with a hybrid spectral collocation method based on Chebyshev polynomials [125] are shown in Figure 1.2, panel b.

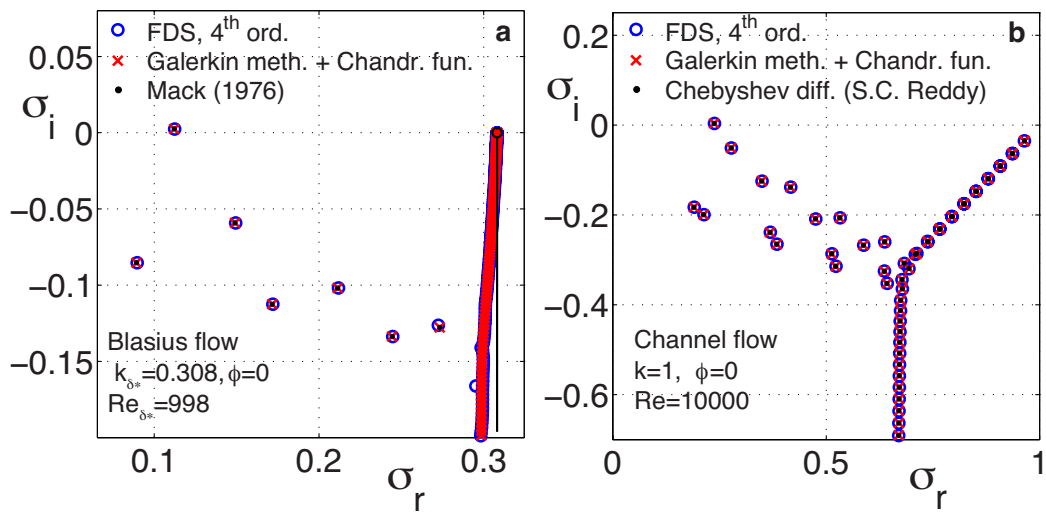


Figure 1.2: Spectra of eigenvalues ( $\sigma = \sigma_r + i\sigma_i$ ) of the Orr-Sommerfeld equation. Comparison of different numerical methods: 4<sup>th</sup> order finite differences scheme on uniform grid (blue circles); 5<sup>th</sup> order Galerkin method on non-uniform grid (red x); a Chebyshev spectral collocation method (code by S.C. Reddy, black points on panel (b)); results by [85] (black points on panel (a)). (a) Blasius boundary layer flow,  $Re_{\delta^*} = 998$ ,  $k_{\delta^*} = 0.308$ ,  $\phi = 0$ . The continuous part of the spectrum is discretely approximated. The black line represents the analytical solution, obtainable only if the boundary condition at  $y \rightarrow \infty$  is relaxed to  $\hat{v}_{y \rightarrow \infty}$  unbounded. As  $Re_{\delta^*}$  and  $k_{\delta^*}$  increase, particular attention is needed to avoid spurious eigenvalues due to the spectrum intrinsic sensibility. Refined non-uniform grids may result necessary, especially for large domains. (b) Channel flow,  $Re = 10000$ ,  $k = 1$ ,  $\phi = 0$ .

## Chapter 2

# Two-dimensional shear flows: transient dynamics and dispersion relation

In this chapter, we focus on the asymptotic behaviour and on the temporal evolution of the wave frequency and phase velocity in two archetypical shear flows, the plane channel flow and the bluff-body plane wake.

As mentioned in Chapter 1, the traditional approach of the stability analysis in shear flows lies in solving the eigenvalue problem which is obtained by imposing a time exponential solution, with complex exponent, to the Orr-Sommerfeld equations. The focus is therefore on the sign of the imaginary part of the eigenvalue with maximum imaginary part, which in our formulation correspond to the grow rate. If it is positive perturbation is unstable if it is negative is stable. On the contrary, our analysis concentrates on the real part of the that eigenvalue, that is the rate at which the phase of the perturbation wave propagates in space, i.e. its phase velocity. We found the existence of a wavenumber threshold ( $k_d$ , in the following) that separates the waves which propagate in a dispersive way from the waves that propagate in a non-dispersive way. If a wave-packet is only composed by waves of the second kind, it can propagate without deformation. If it is centred in  $k_d$  the velocity with which the overall shape of the waves' packet amplitudes propagates through space, the group velocity, can be very high. Well as being of interest for the study of wave packets the existence of this dispersive-non dispersive transition can also affect the transient dynamics of the travelling waves.

Although both Kelvin [64, 65] and Orr [107, 108] recognized that the early transient contains important information, only in recent decades many contributions have been devoted to the study of the transient dynamics of three-dimensional perturbations in shear flows [125, 30]. An example of this possible scenario is represented by the pipe flow. Linear modal analysis assures stability for all the Reynolds numbers [36], but this result is in contrast with the experi-

mental evidence, since the flow becomes turbulent at sufficiently large Reynolds numbers. The disagreement between the linear modal prediction and laboratory results has motivated several recent works [38, 57, 37] that focus on transient travelling waves and their link to the transition process. In general, it is now considered possible that inside the transient life of travelling waves some important events for the stability of the flow can take place [21, 8, 52, 28, 115]. In fact, early algebraic growth can show exceptionally large amplitudes long before an exponential mode is able to set in. It is believed that this kind of behaviour is able to promote rapid transition to fluid turbulence, a phenomenon known as bypass transition [11, 55, 73, 80]. Transient decay of asymptotically unstable waves is also possible, which makes the situation rich and complex at the same time.

Throughout this work, we investigate the temporal evolution of small perturbations acting on the plane channel flow and the bluff-body plane wake, with particular emphasis on the phase velocity transients. Indeed, the frequency or phase velocity transient has been poorly investigated so far. For instance, in the wake flow the attention was mainly devoted to the frequency of vortex shedding for the most unstable spatial scales [148, 109, 130]. Only very recently, subcritical wake regimes (up to values 30% below the critical value) of the vortex shedding of transiently amplified perturbations were studied by considering the spatio-temporal evolution of wave packets [89]. The situation is quite different within the context of atmosphere and climate dynamics. Here, the interaction between low-frequency and high-frequency phenomena, which is related to the existence of very different spatial and temporal scales, is believed to be one of the main reasons for planetary-scale instabilities [131, 101]. However, due to the inherent strong nonlinearity, the evolution of single scales cannot be observed in the geophysical systems and thus also these studies usually do not account for the frequency transient evolution of a single wave.

In this study, the transition between the early transient and the asymptotic state is considered. It is observed that this transition can be highlighted by phase velocity jumps inside the perturbation temporal evolution. This implies that the perturbation may experience accelerations or decelerations during its transient life. This behaviour depends on the initial condition adopted and on the wave-length of the perturbation (if it is shorter or longer in respect the the wavelength that separate the asymptotically dispersive waves from the asymptotically non-dispersive waves). These transient dynamics are therefore closely linked to the asymptotic dispersion relation.

The organization of the chapter is as follows. The physical problem treated is described in Section 2.1. The asymptotic dispersion relation is discussed in Section 2.2. The phase velocity behaviour in the transient is then described in Section 2.3.



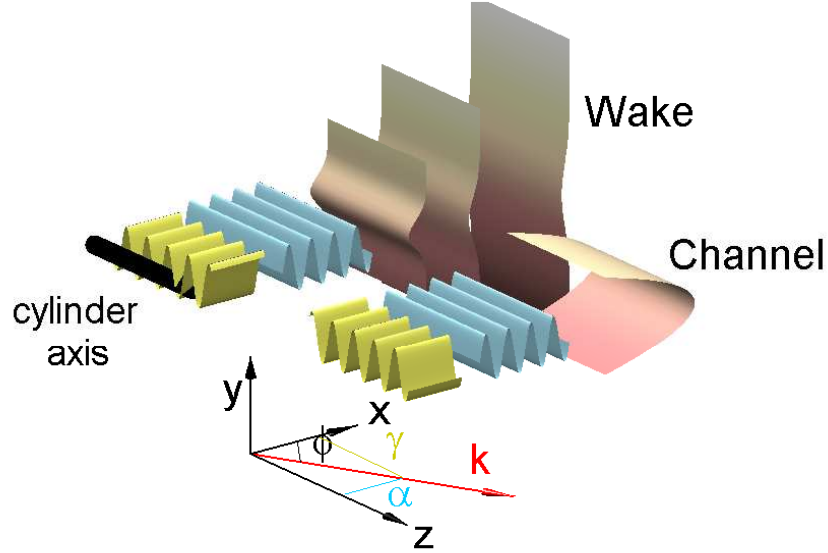


Figure 2.1: Basic flows and perturbation scheme. A cartesian reference frame is adopted, with unit vectors  $\mathbf{e}_1$ ,  $\mathbf{e}_2$ ,  $\mathbf{e}_3$  in the  $x$ ,  $y$ ,  $z$  directions, respectively. The base flow profiles are qualitatively represented in pink. The perturbation is represented by the blue and the yellow waves which propagate in the  $x$  and  $z$  directions, respectively.  $\mathbf{k} = \alpha\mathbf{e}_1 + \gamma\mathbf{e}_3$  is the wavenumber vector,  $\phi$  is its angle with respect to the basic flow  $\mathbf{U} = U(y)\mathbf{e}_1$ .

## 2.1 Physical problem

We consider two typical shear base flows, the plane channel flow, an archetype of bounded flows, and the plane bluff-body wake, one of the few free flow archetypes. A Cartesian reference systems is adopted, with origin at the channel mid plane in the first case and at the bluff-body location, for the wake case. The  $x, y, z$  axis are oriented in the streamwise, transversal and spanwise directions, respectively (see Figure 2.1). After introducing arbitrary small perturbations the linearised, viscous and incompressible governing equations Eq. 1.25 is obtained.

The channel base flow is represented by the plane Poiseuille solution

$$U(y) = 1 - y^2. \quad (2.1)$$

As a wake basic flow, we use the first two order terms of the Navier–Stokes asymptotic solution described in [136] and reported below:

$$U(y; x_0, Re) = C_0 - \frac{1}{\sqrt{x_0}} C_1 e^{-Re y^2 / (4x_0)} \quad (2.2)$$

where  $C_0 = 1$  and  $C_1 = 1.22 + 0.000067Re^2$ . In the present work the frozen-flow approximation is made, by considering different fixed streamwise locations  $x = x_0$  from the body, in the intermediate and far field of the wake. The domain is  $-\infty < x, z < \infty$ ,  $-1 < y < 1$  for the channel flow, and  $0 < x < \infty$ ,  $-\infty < z < \infty$ ,  $-\infty < y < \infty$  for the wake.

To define the Reynold number, as reference length scales the channel half-width  $h$ , and the body diameter  $D$ , are considered. The reference velocity for the channel flow is the centreline velocity  $U_0$ , while in the wake case the free-stream velocity  $U_f$ , is taken. The reference time is the convective one. Consequently, the Reynolds number, defined as  $Re = U_0h/\nu$ , for the channel flow and as  $Re = U_fD/\nu$  for the wake flow, where  $\nu$  is the kinematic viscosity.

In order to measure the perturbation evolution we have already defined variable we need in Section 1.4. In particular in this chapter we will focused on the phase velocity, that we recall is defined as

$$\mathbf{c} = (\omega/k)\hat{\mathbf{k}}, \quad (2.3)$$

and the group velocity that instead is defined as

$$v_g = \frac{d\omega}{dk}. \quad (2.4)$$

## 2.2 Dispersive to non dispersive transition

In this section we focus on the asymptotic behaviour of longitudinal waves and show the dispersion relations, in order to highlight some features which we found to be relevant to understand the temporal evolution of the initial perturbations. Our results have been compared with a large literature data collection, which includes different methods of investigation.

Figure 2.2 shows the dependence of the phase velocity  $c$  on the polar wavenumber  $k$ , in the range  $k \in [0.2, 5]$ . We see that although experimental results are affected by the nonlinear interaction, the agreement between laboratory data and our analysis is very good. In this regard, it has been shown by Delbende and Chomaz [33] that nonlinear terms limit the amplitude of perturbation wave packets and leave unaffected the frequency, see also the laboratory and normal mode data comparisons in [137, 6]. In particular, as regard to the channel flow we observe a good agreement with the works of Nishioka et al. [103], Asai and Floryan [2] and Ito [61] (see panels (a,b) of Figure 2.2).

As regard to the wake flow our references include the literature data of Paranthöen et al. [109], Barkley [5], Giannetti and Luchini [44], Nishioka and Sato [104], Norberg [105], Pier [110], Roshko [118], Williamson [148], and Zebib [150]. The agreement is much better for  $Re = 50$ , i.e. at the onset of instability ( $Re_{cr} \approx 47$ ), see Figure 2.2 panel (c). However, for  $Re = 100$  the current results are not far from literature data (the relative error with respect to the measurements by Williamson lies between 3.3% for  $Re = 50$  and 8.8% for  $Re = 100$ ). Moreover, it should be considered that most of the data used for the comparison only present

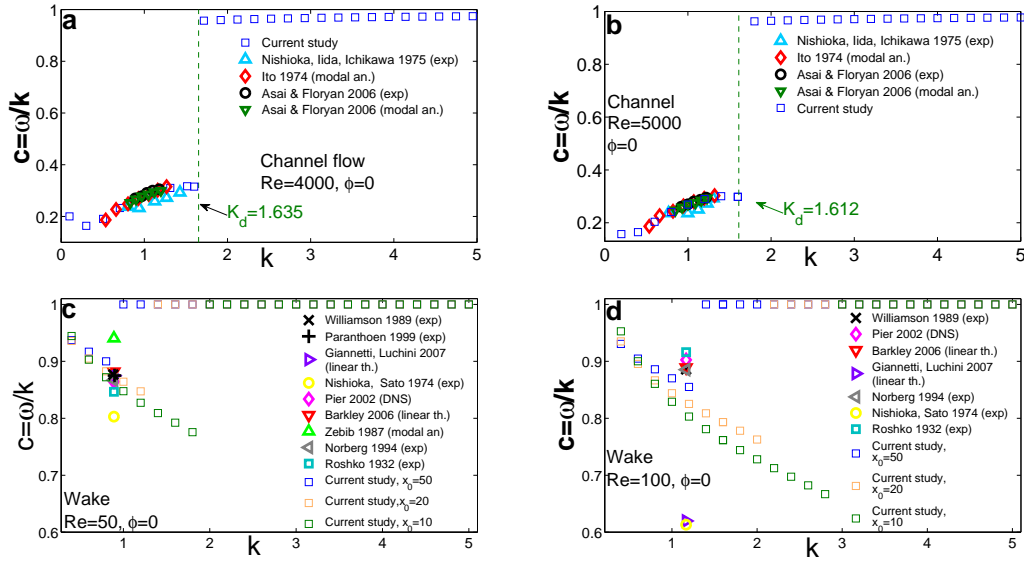


Figure 2.2: Phase velocity as a function of the wavenumber for longitudinal waves ( $\phi = 0$ ) and comparison with literature results. Channel flow, comparison with literature data by Refs. [103, 61, 2] for (a)  $Re = 4000$  and (b)  $Re = 5000$ . Wake flow, comparison with literature data by for [109, 5, 44, 104, 105, 110, 118, 148, 150] for (c)  $Re = 50$  and (d)  $Re = 100$ . Our results are computed at three different streamwise position:  $x_0 = 10, 20, 50$ . Note the jump in the dispersion relation at  $k_d$ .

the frequency at which vortex shedding takes place past the cylinder, the Strouhal number, and no information about the wavenumber of the shedding is provided. To compare the results, we then associate the frequency values reported in literature to the average of the wavenumber between the one observed by Williamson [148] and the one observed by Paranthöen [109], for  $Re = 50$ . For  $Re = 100$  instead, only  $k$  observed by Williamson [148] is known to us.

The comparison is especially rich of data in the range of long waves, which are the most unstable ones [123]. Indeed, these perturbations are those more easily observed in the laboratory, even if usually in their nonlinear regime. We have instead considered a range of wave numbers more extended without being limited to those that lead to instability.

In both cases we observe the existence of a threshold wavenumber,  $k_d$ , where a sudden variation of the phase velocity distribution in the relation dispersion occurs. For  $k > k_d$  the phase velocity is approximately constant and equal to 1 for both the base flows here considered, typical of a non-dispersive behavior. For  $k < k_d$  instead,  $c$  is a general function of  $k$  and the behavior becomes dispersive. In other word, this value clearly separates the dispersive region in the  $c - k$  map from the non-dispersive one. See also Figure 2.3 (a,b) where the phase velocity is compared with the group velocity that is the velocity with which the overall shape of the waves' amplitudes propagates through space ( $v_g = d\omega/dk$ ).

The transition between dispersive and non-dispersive behavior is related to the fact that for

long waves the least-stable Orr-Sommerfeld eigenvalue belongs to the left branch of the eigenvalues spectrum, while for short waves it belongs to the right branch. For three-dimensional perturbations it can be verified that, except in a neighborhood of  $k_d$ ,

$$c(k, \phi) = c(k, \phi = 0) \cos(\phi), \quad (2.5)$$

as a consequence orthogonal waves ( $\phi = \pi/2$ ) are standing waves. In the neighbourhood of  $k_d$  instead the dependence on the angle of obliquity is more complicated. The threshold  $k_d$  is a function of the Reynolds number, the wave angle and, for the wake flow, the streamwise station  $x_0$ . For the channel flow, values of  $k_d$  have been computed for  $Re \in [1000, 8000]$  and  $\phi \in [0, \pi/3]$  and are reported in the Table 2.1. We observe that  $k_d$  increases as  $Re$  and decreases as the wave angle. The  $k_d - Re$  trend is reversed in the wake case and the dependence on  $x_0$  is also shown, values of  $k_d$  are reported for  $Re \in [20, 100]$ ,  $\phi \in [0, \pi/3]$  and  $x_0 = [10, 20, 50]$ . Note that in the wake case the results for three-dimensional perturbations cannot be traced back to the 2D case by the Squire's theorem, since  $U = U(y; Re)$ .

### 2.2.1 The energy equation

In Figure 2.2 we have observed an abrupt transition in the dispersion relation for both base flows. As argued above this transition can be explained by the fact that for long waves the least-stable Orr-Sommerfeld eigenvalue belongs to the left branch of the eigenvalues spectrum, while for short waves it belongs to the right branch. It should be noted that the velocity field is concentrated inside the region where the base flow has a greater shear for the eigenfunctions associated to the left branch of the eigenvalues spectrum; while the velocity field is concentrated outside this region for the eigenfunctions associated to the right branch. In the case of the channel flow this means that the least stable mode takes significant values near the walls for long waves and it is localized in the center of the channel for short waves. On the contrary, in the case of the wake flow, the least stable mode is localized in the center of the domain for long waves while it is distributed outside the cylinder's wake region for short waves. A question naturally arises: why for  $k$  greater than a given value does the system prefer to settle on a different configuration? In the attempt to answer this question, we examine the evolution of the kinetic energy equation, that is:

$$\frac{dE}{dt} = - \underbrace{\frac{1}{k^2 Re} \int_{-y_f}^{y_f} (|\partial_{yy} v|^2 + 2k^2 |\partial_y v|^2 + k^4 |v|^2) dy}_{\text{Viscous terms}} + \underbrace{\frac{1}{k} \Im \int_{-y_f}^{y_f} U \bar{v} \partial_{yy} v dy}_{\text{Convective term}} \quad (2.6)$$

where  $\bar{v}$  indicate the  $v$  conjugate and  $\Im$  the imaginary part. In Figure 2.3(c,d,e,f) we compare convective and the viscous term for the least stable mode and the second last one, where if the least stable eigenvalue belongs to the left branch (i.e.  $k < k_d$ ) the second last one belongs to

Channel flow				
<b>Re</b> \ $\phi$	0	$\pi/6$	$\pi/4$	$\pi/3$
<b>1000</b>	2.071	2.111	2.168	2.256
<b>2000</b>	1.883	1.922	1.979	2.073
<b>3000</b>	1.764	1.803	1.866	1.960
<b>4000</b>	1.686	1.725	1.784	1.878
<b>5000</b>	1.623	1.662	1.721	1.815
<b>6000</b>	1.576	1.615	1.670	1.765
<b>7000</b>	1.536	1.568	1.627	1.720
<b>8000</b>	1.497	1.536	1.589	1.682

Wake flow, $x_0 = 20$				
<b>Re</b> \ $\phi$	0	$\pi/6$	$\pi/4$	$\pi/3$
<b>20</b>	0.756	0.732	0.691	0.616
<b>30</b>	0.968	0.943	0.896	0.815
<b>40</b>	1.153	1.118	1.086	0.987
<b>50</b>	1.325	1.294	1.250	1.159
<b>60</b>	1.471	1.441	1.400	1.318
<b>70</b>	1.616	1.587	1.550	1.463
<b>80</b>	1.748	1.719	1.686	1.596
<b>90</b>	1.881	1.851	1.809	1.728
<b>100</b>	1.992	1.983	1.945	1.860

Wake flow, $x_0 = 10$				
<b>Re</b> \ $\phi$	0	$\pi/6$	$\pi/4$	$\pi/3$
<b>20</b>	1.061	1.020	0.977	0.861
<b>30</b>	1.364	1.323	1.265	1.143
<b>40</b>	1.626	1.586	1.534	1.406
<b>50</b>	1.869	1.828	1.764	1.628
<b>60</b>	2.091	2.050	1.975	1.851
<b>70</b>	2.293	2.252	2.186	2.052
<b>80</b>	2.475	2.434	2.378	2.254
<b>90</b>	2.657	2.616	2.570	2.436
<b>100</b>	2.818	2.798	2.742	2.618

Wake flow, $x_0 = 50$				
<b>Re</b> \ $\phi$	0	$\pi/6$	$\pi/4$	$\pi/3$
<b>20</b>	0.483	0.461	0.441	0.401
<b>30</b>	0.596	0.593	0.573	0.522
<b>40</b>	0.709	0.714	0.684	0.633
<b>50</b>	0.822	0.815	0.795	0.734
<b>60</b>	0.935	0.916	0.886	0.835
<b>70</b>	1.020	1.007	0.977	0.926
<b>80</b>	1.105	1.088	1.068	1.007
<b>90</b>	1.189	1.169	1.148	1.098
<b>100</b>	1.246	1.249	1.229	1.179

Table 2.1: Values of the dispersive regime threshold wavenumber  $k_d$  for the channel and the wake flows, for different Reynolds number and obliquity angles. The uncertainty on  $k_d$  due to the discretization is  $\pm 0.005$ .

the right one and vice versa. In the right branch the symmetric and antisymmetric modes have almost identical eigenvalues. For simplicity we have considered only the symmetric ones but it can be shown that the results do not change by taking only the antisymmetric ones.  $C1$  and  $D1$  indicate respectively the convective and the viscous term for the least stable mode,  $C2$  and  $D2$  for the second last one. It can be observed that the system assume the configuration that maximize the contribution due to the convection, except that in a neighbourhood of  $k_d$ .

Though this results are related only to the asymptotic state of the perturbations, but as will be shown in the next section they are relevant to understand the perturbations transient dynamics.

### 2.3 Phase velocity transient dynamics

Recent studies on shear flows [21, 28] have shown the importance of the early time dynamics, that in principle can lead to non-linear growth long before the asymptotic exponential mode is dominant. Transient dynamics offers a variety of different behavior and phenomena which are not easy to predict *a priori*. It is interesting to note that these phenomena develop in the context of the linear dynamics, where interaction among different perturbations (and even self-interaction) is absent. In order to specify how given initial conditions the system evolves with time, proper initial conditions on  $\hat{v}$  and  $\hat{\omega}_y$  have to be associated to the system of equations 1.25.

In literature the transient dynamics is generally analyzed in terms of amplification factor, and little attention has been paid to the phase velocity and/or frequency transient. One of the aims of this paper is instead to analyze the transient perturbation in terms of phase velocity and to understand how many time scales the perturbation dynamics involves.

We have computed the phase velocity by the transverse velocity component  $\hat{v}$ , see Eqs. 1.41-1.42. We can of course consider any component of velocity and vorticity, but  $\hat{v}$  is always non-zero for any choice of the obliquity angle. Moreover the first equation of 1.25 is homogeneous and it can be demonstrated that the eventual introduction of an initial transversal vorticity does not actually affect the perturbation temporal evolution, see Ref. [122]. For this reason the initial vorticity  $\hat{\omega}_y(0, y)$  is set to zero for all the simulations showed in this paper.

Through an exploratory study that considers different types of initial conditions on the transversal velocity, we conclude that the characteristics influencing the transient are essentially two: symmetry/antisymmetry and centrality/non-centrality. Note that a ‘‘central’’ initial condition  $\hat{v}_0 = \hat{v}(t = 0, y)$  has its largest variations  $d\hat{v}/dy$  close to the base flow symmetry plane  $y = 0$ . By combining these two features, it is possible to classify the set of the possible initial conditions into four types that we can call:

- SC, symmetric and central,
- AC, antisymmetric and central,

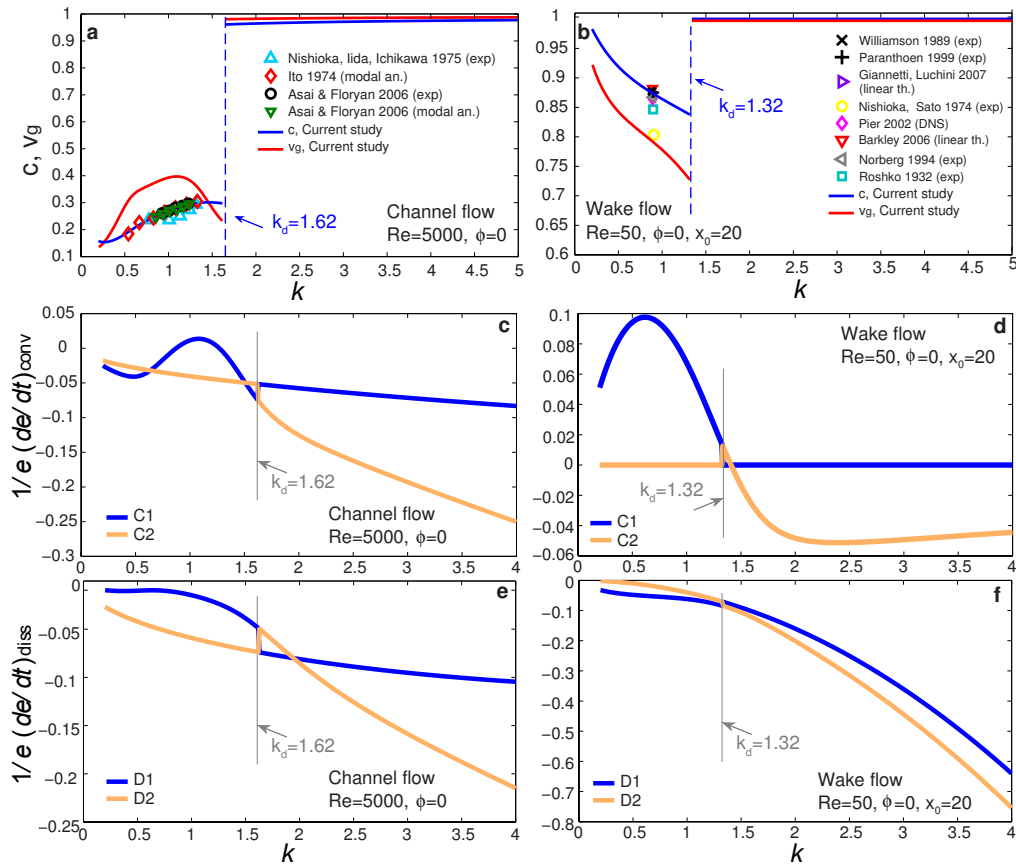


Figure 2.3: (a,b) Phase and group velocity as a function of the wavenumber for longitudinal waves ( $\phi = 0$ ) and comparison with literature results. The phase velocity is represented with the blue line (1024 computed points), while the group velocity with the red one and comparison with literature data as in Figure 2.2. Wave packets containing the wavenumber  $k_d$  can actually show a very high group velocity. (c,d,e,f) Energy time derivative convective and dissipative terms as defined in equation 2.6, for the two least-stable symmetric eigenmodes, as a function of the wavenumber. Blue lines are for the least stable eigensolution, yellow lines represents the symmetric second-last. (a) Channel flow with  $Re = 5000$ ,  $\phi = 0$ . (b) Wake flow,  $Re = 50$  and  $x_0 = 20$ . For  $k < k_d$  the least-stable solution belongs to the left branch of the eigenvalues spectrum, while for  $k > k_d$  it belongs to the right branch. Though the eigenmodes, considered separately, evolve continuously with  $k$ , we can observe that the least-stable is, among all, the solution that maximizes the convective energy term.

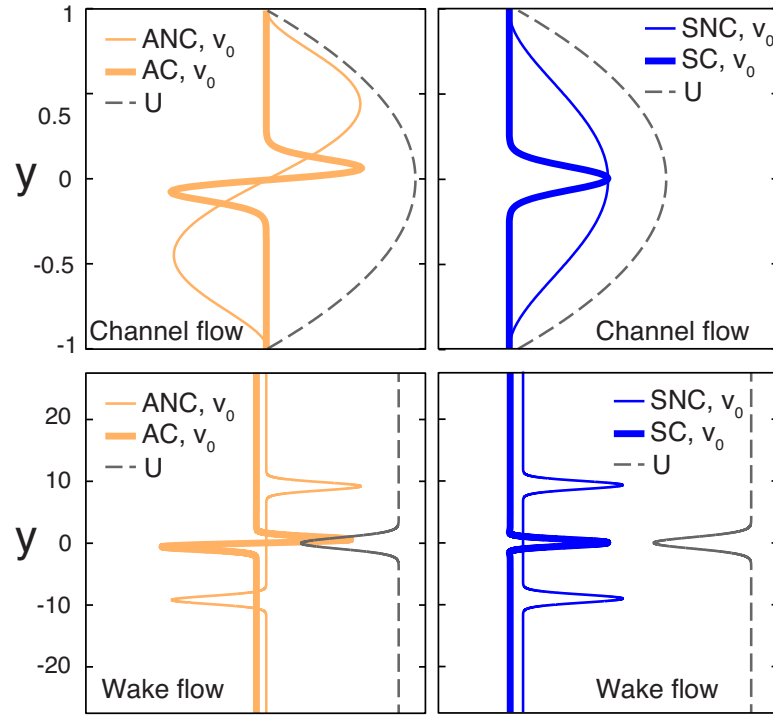


Figure 2.4: Initial velocity disturbances  $\hat{v}_0$  and base flows (amplitudes have been scaled for clarity). Top panels: channel flow. Bottom panels: wake flow. Dark lines represent symmetric disturbances (left panels), while light lines are for antisymmetric ones (right panels). Thick lines indicate central initial disturbances, thin curves represent the non-central ones.

- SNC, symmetric and non central,
- ANC, antisymmetric and non central.

In Figure 2.4 the prototypes of the different typology of initial condition are shown for both base flows, while the exact expressions adopted are given in Table 2.2.

We start the discussion by presenting an overview for transient dynamics, showing the evolution of three-dimensional perturbations in terms of amplification factor  $G$ , phase velocity  $c$ , and temporal growth rate  $r$ , and comparing the results obtained by the IVP with the eigenvalue spectra given by the modal analysis. In Figure 2.5 the transient dynamics of perturbations with initial conditions as in Table 2.2 are shown for both the base flows and for  $k < k_d$ . Trends for small wave numbers are shown here, as they are the most easily observable in the laboratory. However in Figure 2.7 we summarize in a general scheme the transient perturbations behavior also for disturbances with large wavenumbers.

The amplification factors and the temporal growth rates are reported in Figure 2.5 (b,c,f,g) for the two base flows. For the wake flow, we can observe that an initial condition of the kind



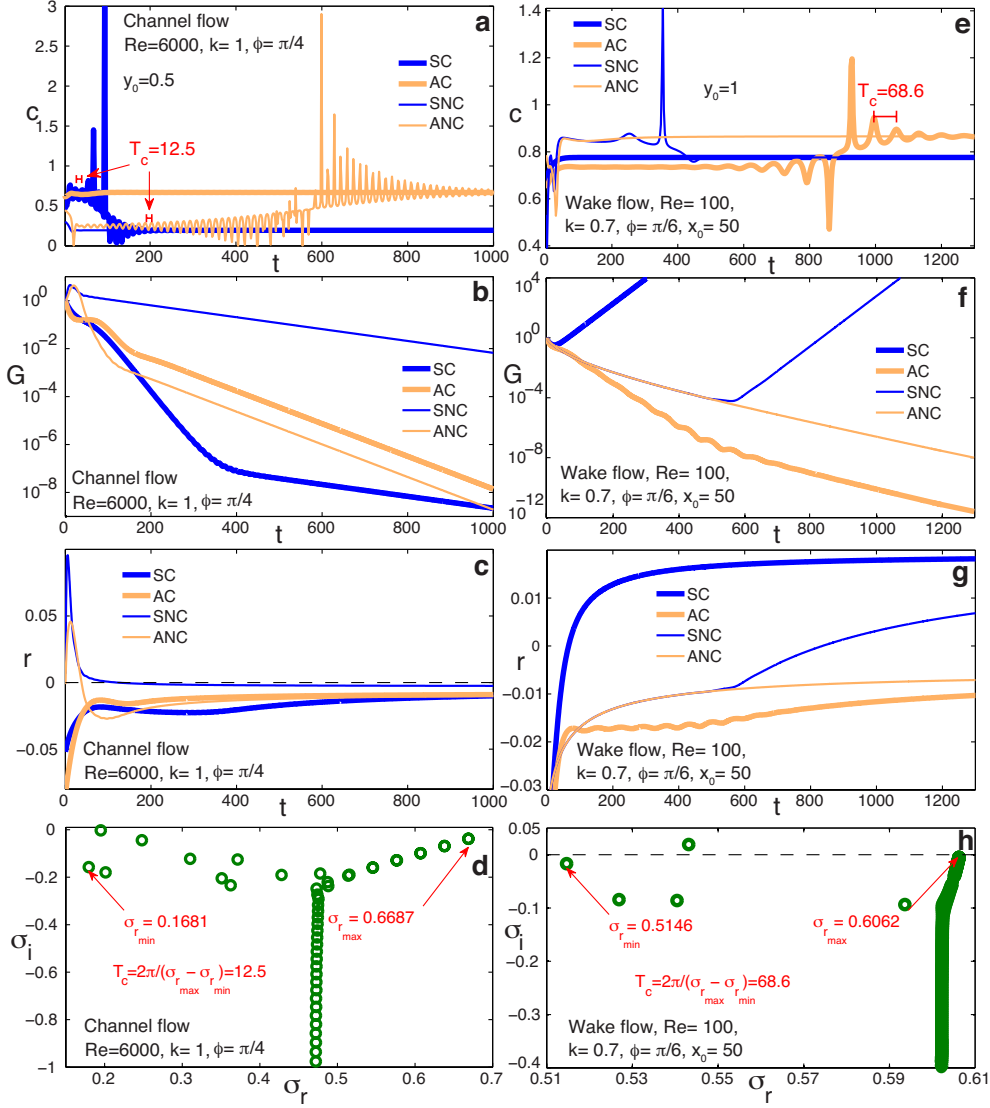


Figure 2.5: Transient lives of the perturbations observed through the the phase velocity  $c$  (a, e), the amplification factor  $G$  (b, f), and the temporal growth rate  $r$  (c, g), for four types of initial conditions. The eigenvalues spectra are shown in panels (d, h). Left column: channel flow with  $Re = 6000$ ,  $\phi = \pi/4$  and  $k = 1$ . Right column: wake flow with  $Re = 100$ ,  $\phi = \pi/6$  and  $k = 0.7$ . The phase velocity is computed at  $y_0 = 0.5$  for the channel and at  $y_0 = 1$  for the wake flow (remind that the reference lengths are the channel half-width and the cylinder diameter). The quantity  $T_c$ , see (a) and (e), indicates the temporal periodicity shown by the phase velocity fluctuations observed in the early and intermediate term and corresponds to the ratio  $T_c = 2\pi/[\sigma_{r_{max}} - \sigma_{r_{min}}]$ , as shown in panels (d) and (h).

IC	Wake flow	Channel flow
SC	$\hat{v}(0) = e^{-y^2} \cos(y)$	$\hat{v}(0) = e^{-\frac{y^2}{0.01}} \cos(3y)$
AC	$\hat{v}(0) = e^{-y^2} \sin(y)$	$\hat{v}(0) = e^{-\frac{y^2}{0.01}} \sin(3y)$
SNC	$\hat{v}(0) = e^{-(y-10)^2} + e^{-(y+10)^2}$	$\hat{v}(0) = (1 - y^2)^2$
ANC	$\hat{v}(0) = e^{-(y-10)^2} - e^{-(y+10)^2}$	$\hat{v}(0) = y(1 - y^2)^2$

Table 2.2: Initial conditions imposed on the velocity,  $\hat{v}_0 = \hat{v}(0, y)$ , for both the channel and the wake flows. SC: symmetric and central. SNC: symmetric and non central. AC: antisymmetric and central. ANC: antisymmetric and non central (see Figure 2.4).

SC - symmetric and localized inside the base flow shear region - and ANC- antisymmetric external to the base flow shear region - the asymptotic exponential behavior predicted by the modal analysis is reached after few temporal scales. On the contrary, with the other kind of initial conditions - SNC and AC - the transients can last up to hundreds of time units. In these cases quite far along within the transient the phase velocity abruptly changes its value, a phenomenon that we denominate phase velocity jumps (see panel *e*). For symmetric initial conditions external to the base flow shear region, SNC, the perturbation after the jump slows down, i.e the phase velocity jumps to a lower value. For antisymmetric initial conditions localized in the base flow shear region, AC, the perturbation the phase velocity jumps to a higher value, so it experiences an acceleration.

The same behavior is observed in the case of the channel flow, but here the role of the initial conditions is the opposite. In fact, SNC and AC reach the asymptotic exponential behavior after few time scales, while SC and ANC have a long transient characterized by the presence of phase velocity jumps (see Figure 2.5 *a*). Also in this case the phase velocity of the symmetric perturbation jumps to a smaller value while in the antisymmetric case it shifts to an higher value. The different behavior of the two base flows can be traced back to the structure of the eigenvalue spectra and the associated eigenmodes. Indeed, it is known that for the channel flow the eigensolutions of the left branch (A-branch) are wall-modes while those of the right branch (P-branch) are central modes. The opposite applies for the wake flow, whose spectra are made of a discrete set (left branch) of central modes, and a continuous branch of non-central modes. As for the channel case, both branches contain symmetric and antisymmetric functions.

Besides the two temporal scales associated to the value of the phase velocity before and after the jumps ( $T = 2\pi/(ck)$ ), we observe a further periodicity,  $T_c$ , related to the temporal modulation of the frequency during the early and intermediate terms, see Figure 2.5 panels (*a*) and (*e*). This period corresponds to the width of the spectral range of frequencies given by the modal theory  $T_c = 2\pi/[\sigma_{r_{max}} - \sigma_{r_{min}}]$ .

The system presents other two temporal scales: the external scale related to the base flow and the length of the transient (which can be determined by observing the time instant beyond

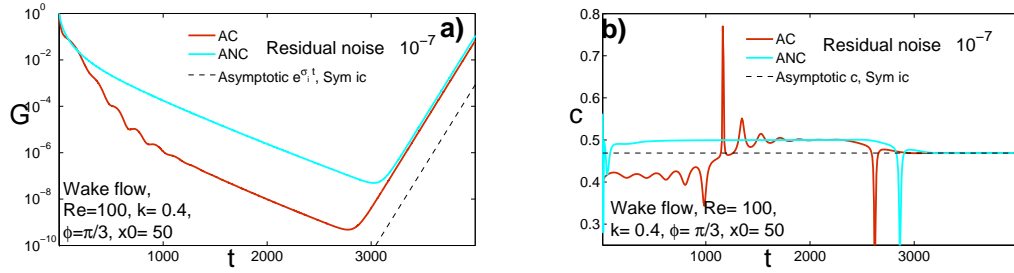


Figure 2.6: Temporal evolution of mixed symmetric-antisymmetric initial conditions for the wake flow with  $Re = 100$ ,  $k = 0.4$ ,  $\phi = \pi/3$  and  $x_0 = 50$ . A small uniform random noise of magnitude  $O(10^{-7})$  is added to the initial conditions AC and ANC in order to simulate the transient life of a general initial disturbance. (a) Growth rate. (b) Phase velocity. The dashed line represents the asymptotic trend given by the least stable OS eigenvalue.

which the growth rate,  $r$ , and the angular frequency,  $\omega$ , are both constant). Therefore, for each wavenumber it is possible to count up to five different time scales.

Figure 2.5 show that symmetric and antisymmetric perturbations do not have the same asymptotic behavior. More precisely symmetric perturbations are always less stable than antisymmetric one. This means that if we consider mixed initial conditions, the symmetric component will always prevail. Of course, in laboratory experiments, one cannot assume the precise symmetry because residual disturbance cannot be completely suppressed. As a consequence the phase velocity that can be eventually observed is the one given by the symmetric part of the initial condition. In an attempt to reproduce what might happen in laboratory, we can build up a mixed initial condition with prevailing antisymmetric component, by adding to the AC and the ANC conditions a small noise which models the presence of a small symmetric part. The evolution of such a disturbance is shown in Figure 2.6: after an early transient, the phase velocity experiences a jump (as it happens for AC and ANC) and then the solution keeps the antisymmetric (exponential self-similar decay,  $1000 < t < 2900$ ) shape until the symmetric part becomes dominant and the asymptote is eventually reached, announced by a second frequency jump. In this case the asymptotic solution is a symmetric growing mode.

## 2.4 Acceleration-deceleration general scheme

Figure 2.7 shows a full scheme of the perturbation transient type, and the possibility of frequency jumps to occur, for any different combinations wavenumber-type of initial condition, differentiating the cases where the perturbation is accelerated or decelerated after the jump. Moreover when a perturbation accelerate it goes from a dispersive to a non dispersive behaviour and vice-versa. Therefore the dispersivity of a waves can change also during its transient which make the wave packets dynamics more complex.



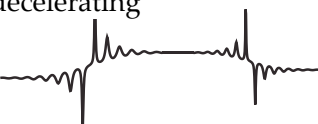
Transient behavior	Wake flow	Channel flow
No jumps Short transient	Initial condition SC, and $k < k_d$	<ul style="list-style-type: none"> <li>• Initial conditions SNC or AC, and <math>k &lt; k_d</math></li> <li>• Initial conditions SC or AC, and <math>k &gt; k_d</math></li> </ul>
One jump, accelerating 	<ul style="list-style-type: none"> <li>• Initial conditions ANC or AC, and <math>k &lt; k_d</math></li> <li>• Every initial condition, and <math>k &gt; k_d</math></li> </ul>	<ul style="list-style-type: none"> <li>• Initial conditions ANC, and <math>k &lt; k_d</math></li> <li>• Initial conditions SNC or ANC, and <math>k &gt; k_d</math></li> </ul>
One jump, decelerating 	Initial conditions SNC, and $k < k_d$	Initial conditions SC, and $k < k_d$
Two jumps, accelerating-decelerating 	Mixed initial conditions with dominant antisym. component, and $k < k_d$	Mixed initial conditions with dominant antisym. component, and $k < k_d$

Figure 2.7: Scheme of the possible perturbation transient behavior. *Left column*: type of transient, the black line represents the phase velocity jump, while the red draw indicates the self-similar velocity profiles for the wake case. *Mid column*: wake flow; in each cell the conditions under which the corresponding transient type can realize are indicated, in terms of initial condition type (SC=symmetric central, AC=antisymmetric central, SNC=symmetric non-central, ANC=antisymmetric non-central) and the wavenumber value, namely  $k < k_d$  or  $k > k_d$ . *Right column*: channel flow.

It is also important to notice that the frequency/phase velocity jumps are observed for long enough time. For instance in the case of the wake flow,  $Re = 100$  and AC type initial condition (see red curve in Figure 3.4), if we consider a cylinder with  $D = 2 \text{ cm}$  the jump arrive after nearly 3 minutes if the fluid is air, and after nearly 40 minutes if the fluid considered is water.

The observations of phase velocity jumps yield an interesting result: the perturbation temporal evolution have a three-part structure, with an early stage, an intermediate stage and an asymptotic stage. The early transient is the stage where the perturbation is most affected by the fine details of the initial condition and represents a period of adjustment. During the intermediate stage the perturbation evolves almost exponentially: the phase velocity takes the final constant value, the transverse velocity profiles maintain a near self-similar nature in time and the growth factor changes very slowly. This stage appears as a kind of intermediate asymptotics and that can be in general considered extinguished only when both the frequency and the temporal growth rate become constant so that the asymptotic regime is reached. This transient structure is common to all perturbations. Moreover, in the case in which the frequency transient presents one or more jumps, the beginning of the intermediate asymptotics is clearly announced by the last jump.

In the next chapter the properties of self similarity that characterize the intermediate transient will be investigated.

## Chapter 3

# Intermediate transient: self similar solution and energy spectra

In previous chapter we have seen that phase velocity jumps may occur inside the transients. We have observed up to two jumps. We can interpret the appearance of the jumps, which can be preceded and followed by modulating fluctuations, as the boundaries between an early transient and the beginning of an intermediate term. During the intermediate stage the perturbation evolves almost exponentially: the phase velocity takes the final constant value, the transverse velocity profiles maintain a near self-similar nature in time and the growth factor changes very slowly. This stage appears as a kind of intermediate asymptotics and that can be in general considered extinguished only when both the frequency and the temporal growth rate become constant so that the asymptotic regime is reached. In this chapter, we analyse the similarity properties of the time history inside the intermediate term.

Moreover we have considered that, at any instant, the laminar system can host a multiplicity of scales. Small perturbations which randomly enter the system and, in the linear framework, evolve independently from each other. Although linearity on one hand allows each evolution to be determined singularly, on the other, it should be recalled that a large number of perturbations (not even bounded, in principle) are present at the same time. In this chapter, we try to consider and observe the collective behaviour of small perturbations. The aim is the understanding and the discovering of possible similarities with turbulence behaviour.

As an example, in order to understand whether, and to what extent, spectral representation can effectively highlight the non-linear interaction that occurs among different scales, it could be useful to consider the state that precedes the onset of both instability and turbulence in flows. In this condition, even if stable, the system is however subject to a swarming of small arbitrary three-dimensional perturbations that constitutes a system of multiple spatial and temporal scales subject to all the processes included in the Navier-Stokes equations: linearised convective transport, linearised vortical stretching and tilting, and molecular diffusion. If we

leave aside nonlinear interaction of the different scales, the other features are tantamount to the features of the turbulent state.

If it were possible to observe such a system, by computing and comparing a large set of three dimensional waves, and build spectra, it would be possible, among others, to determine if a power scaling in the intermediate range exists and, in case, to compare it with the exponent of the corresponding developed turbulent state (notoriously equal to  $-5/3$ ). In the case a power scaling exists, two possible situations can therefore appear. A - The exponent difference is large, and as such, is a quantitative measure of the nonlinear interaction in spectral terms. B - The difference is small. This would indicate a higher level of universality on the value of the exponent of the intermediate range (the inertial range in turbulence), not necessarily associated to the nonlinear interaction. For this purpose, by solving a large number of initial-value problems, we have determined a large set of transient solutions for the two typical shear flows considered before.

This chapter is organized as follow. Consideration about the duration of the intermediate transient are made in Section 3.1. Section 3.2 present the features of the velocity field inside the intermediate transient. How the energy is distributed among the different scales inside the intermediate transient is treated in Section 3.3.

### 3.1 Intermediate transient

The observations of the perturbation transient dynamics made in the previous chapter yield an interesting result: the perturbation temporal evolution has a three-part structure, with an early stage, an intermediate stage and an asymptotic stage. This is clearly seen by the fact that events like phase velocity jumps and associated fluctuations split the transient into two parts, where the second part is much longer than the first one. The asymptotic evolution will eventually follow.

The intermediate transient can be considered extinguished only when the temporal growth rate,  $r$ , also becomes constant. A measure of the temporal scales related to the end of the early transient and the reaching of the asymptotic state ( $t_e$  and  $t_a$ , respectively) is reported in figure 3.1, by considering different perturbation wavelengths for both the wake with and channel flows. The initial condition considered are respectively AC and SNC. The length of the intermediate transient can be obtained by calculating the difference between  $t_a$  and  $t_e$ , and is in general one order of magnitude larger than the early term.

We have also determined the scaling with the Reynolds number of the time where the early part of the transient ends ( $t_e$ ) and the time where the transient ends and the evolution reaches the final exponential state ( $t_a$ ), see Figures 3.2). One may notice that for the total transient duration,  $t_a$ , the scaling presents positive exponents less than 1. The exponents for these oblique waves ( $\phi = \pi/4$ ) are close in the two cases (0.34 in the channel flow, 0.4 in the wake). The situation is different for the early transient time scale. The channel flow does not feel the Reynolds

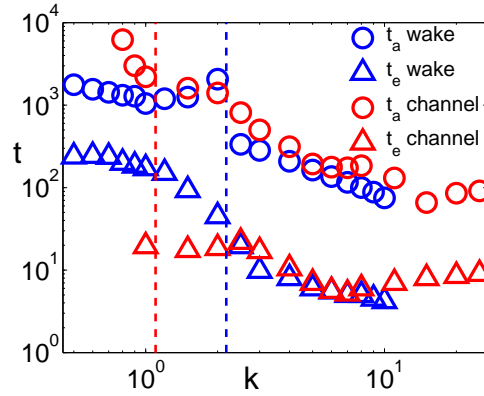


Figure 3.1: Typical transient time scales.  $t_a$  (circles): time where the asymptotic limit is reached ( $r$  and  $\omega$  settle to the final constant values).  $t_e$  (triangles): time where the early transient ends and the phase velocity jumps occur. The intermediate term is given by the difference  $t_a - t_e$ , and generally is one order of magnitude longer than the early term. Blue symbols: wake flow,  $Re = 100$ , AC initial conditions,  $\phi = \pi/4$ , the wake profile is observed at a distance from the body equal to 10 body scales,  $x_0 = 10$ , and  $y_0 = 1$ . Red symbols: channel flow  $Re = 10000$ , SNC initial conditions,  $\phi = \pi/4$ , the channel is longitudinally homogeneous, thus to specify the observation point it is sufficient to choose the transversal location, in this case the point is the midpoint between the wall and the channel axis,  $y_0 = 0.5$ . The dashed red and blue lines represent the transition from asymptotically unstable to stable wavenumbers.

number variation, the wake instead presents a decay with exponent  $-0.52$ . In any case, both cases evidence a definite trend of growth for the intermediate term (equal to the difference  $t_a - t_e$ ) with the Reynolds number. In general the intermediate term is more than one order of magnitude larger than the early transient.

### 3.2 Scaling propriety inside the intermediate transient

After defining the intermediate transient and discussed its existence and duration, a question arises: whether in this range the solution has some feature properties.

As mentioned before, during the intermediate stage the perturbation evolution is almost exponentially and the growth factor changes very slowly. This stage appears as a kind of intermediate asymptotics and its presence is common to all perturbations transient. Moreover, in the case in which the frequency transient presents one or more jumps, the beginning of the intermediate asymptotics is clearly announced by the last jump. In this stage the transverse velocity profiles maintain a near self-similar nature in time as shown in Figures 3.3 and 3.4. We present the cases of  $Re = 100$ ,  $x_0 = 50$ ,  $k = 0.7$ ,  $\phi = \pi/6$  with SNC and AC initial condition for the wake flow and of  $Re = 6000$ ,  $k = 1$ ,  $\phi = \pi/4$  with SC and ANC initial condition for the channel flow.



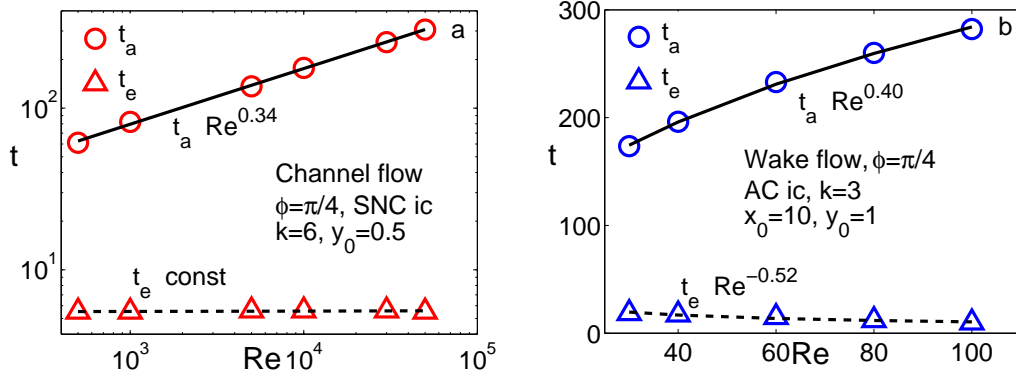


Figure 3.2: Scaling of the transient time scales with respect to the Reynolds number:  $t_e$  (triangles) is the time where the early transient ends and the frequency discontinuities occur, while  $t_a$  (circles) is the time where the asymptotic limit is reached. Panel (a): channel flow,  $\phi = \pi/4$ , SNC initial conditions,  $k = 6$ , the transversal observation point is  $y_0 = 0.5$ .  $Re = [500, 50000]$ . For the end of the mid-term we found a scaling  $t_a \sim Re^{0.34}$  (solid curve), while the early transient remains constant, thus it is not sensitive to the Reynolds number variation. A log-log scale is adopted. Panel (b): wake flow,  $\phi = \pi/4$ , AC initial conditions,  $k = 3$ , the longitudinal and transversal observation points are  $x_0 = 10$  and  $y_0 = 1$ , respectively.  $Re = [30, 100]$ . The end of the early transient scales as  $t_e \sim Re^{-0.52}$  (dashed curve), while the time where the asymptotic state is reached scales as  $t_a \sim Re^{0.40}$  (solid curve). For both flows the intermediate region ( $t_a - t_e$ ) increases with the Reynolds number. As an indication, the maximum relative error of the fitting is, in the worst case, about 8%.

In the channel case, since the lateral diffusion is blocked by the walls, to highlight the similarity, it is sufficient to normalize the solution by the profile peak value (the  $\infty$ -norm).

In the wake case the similarity is showed by normalizing the solution by the peak value of the profiles and by normalizing the lateral coordinate by the instantaneous width of the perturbation profile (the distance from the axis where  $|\hat{v}|/\|\hat{v}\|_\infty = 0.01$ ). In the reported cases, the wake perturbation width scales in time as  $t^p$ , with  $p \approx 0.42$ . The general trend for  $p$  is shown in Figure 3.5. One can observe that the exponent decreases as the Reynolds number and increases as the wave obliquity and the polar wavenumber. For very low values of the Reynolds number, when the inertial effects become very little, the exponent is expected to take the value 0.5. Note that  $Re \approx 20$  is the smallest reliable value for which the wake flow can be represented in terms of a matched asymptotic expansion solution valid in both the spatial intermediate and far field, see Ref. [136] for major details on the wake base flow computation. The dependence on the obliquity angle is weak at low angles, while the diffusive scaling  $t^{0.5}$  occurs for perturbations orthogonal to the base flow ( $\phi = \pi/2$ ) since in this case the convective transport does not matter, see Eqs.1.25. Moreover, as expected, we observe that short waves present a more diffusive behaviour than long ones as shown in Figure 3.5, panel (b).

About the cases of expanding perturbation along the  $y$  direction, as shown in Figure 3.4, the rapid change in the perturbation shape (and the  $y$ -location of its peak) seem to happen when

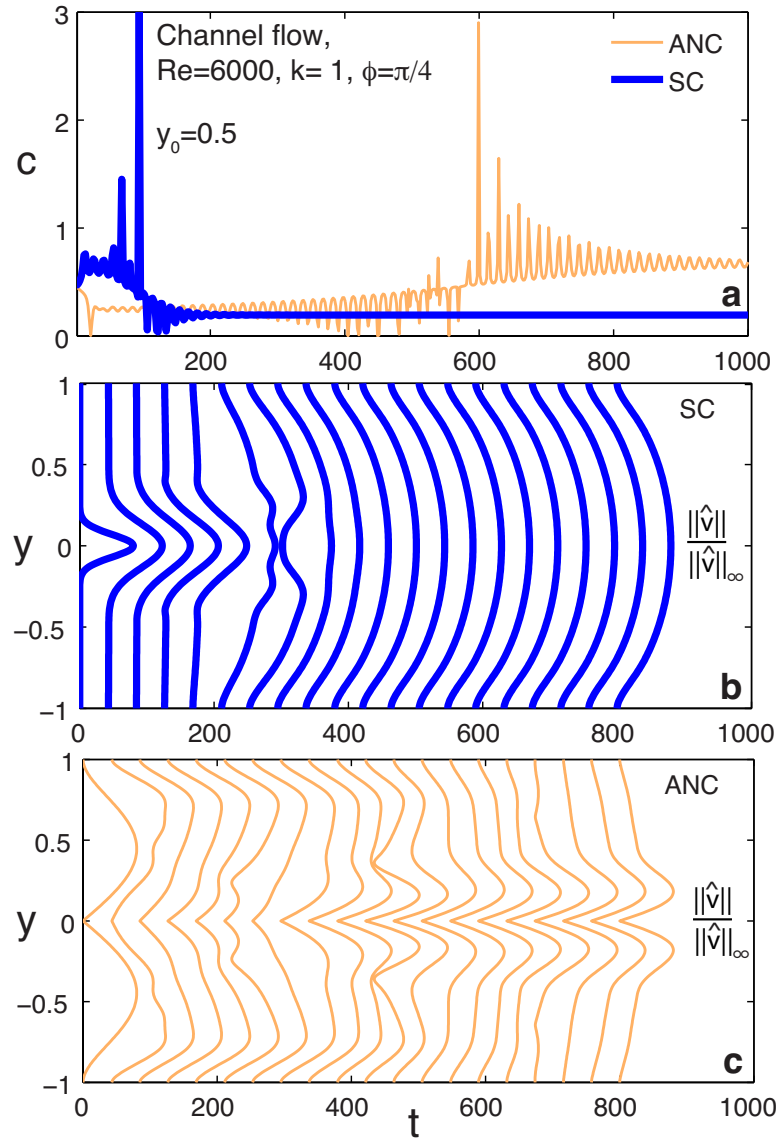


Figure 3.3: Channel flow,  $Re = 6000$ ,  $k = 1$ ,  $\phi = \pi/4$ , initial conditions ANC (blue lines) and SC (red lines). (a) Temporal evolution of the phase velocity, computed at  $y_0 = 0.5$ . A jump is observed at  $t \approx 100$  for SC and at  $t \approx 600$  for ANC. (b) Evolution of velocity profile modulus for the SC initial condition. The profiles are normalized with respect to their peak value. (c) Evolution of the normalized velocity profiles for the case of ANC initial condition. The phase velocity shifts indicate a substantial change in the velocity profiles. This transition can be more or less abrupt depending on the simulation parameters, and the regions before and after the jump can show a nearly self-similar behavior.

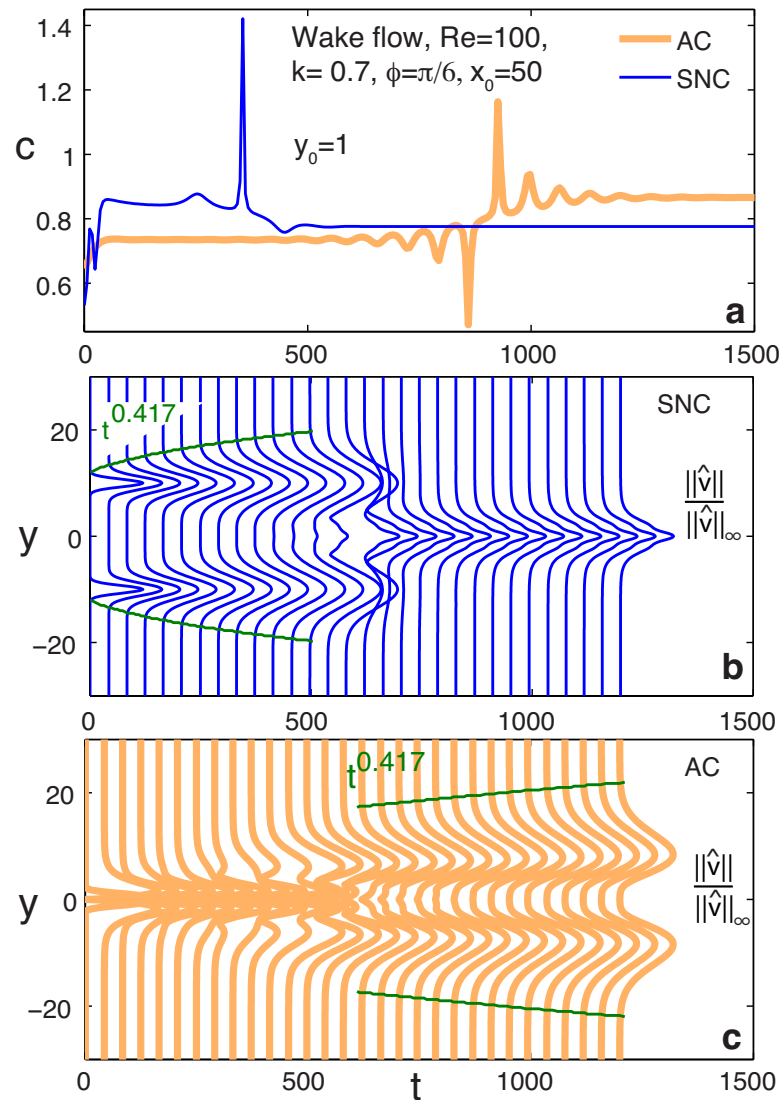


Figure 3.4: Wake flow,  $Re = 100$ ,  $k = 0.7$ ,  $\phi = \pi/6$ ,  $x_0 = 50$ , initial conditions AC (red lines) and SNC (blue lines). (a) Temporal evolution of the phase velocity, computed at  $y_0 = 1$ . A jump is observed at  $t \approx 400$  for SNC and at  $t \approx 800$  for AC. (b) Evolution of the velocity profile modulus for the SNC case. The profiles are normalized with respect to their peak value. (c) Evolution of the normalized velocity profiles for the case of AC case. It can be noticed that the solution for the wake flow admits a three-part structure with the presence of self-similar terms (see Figure 2.7) of expanding profiles. It is also interesting to note that the rapid transition happens when the perturbation reaches the shear wake region from the outer one (as the SNC case, panel b), or viceversa as the AC case (panel c). The perturbation width follows a power law  $t^p$ ,  $p \approx 0.42$  in the above cases.

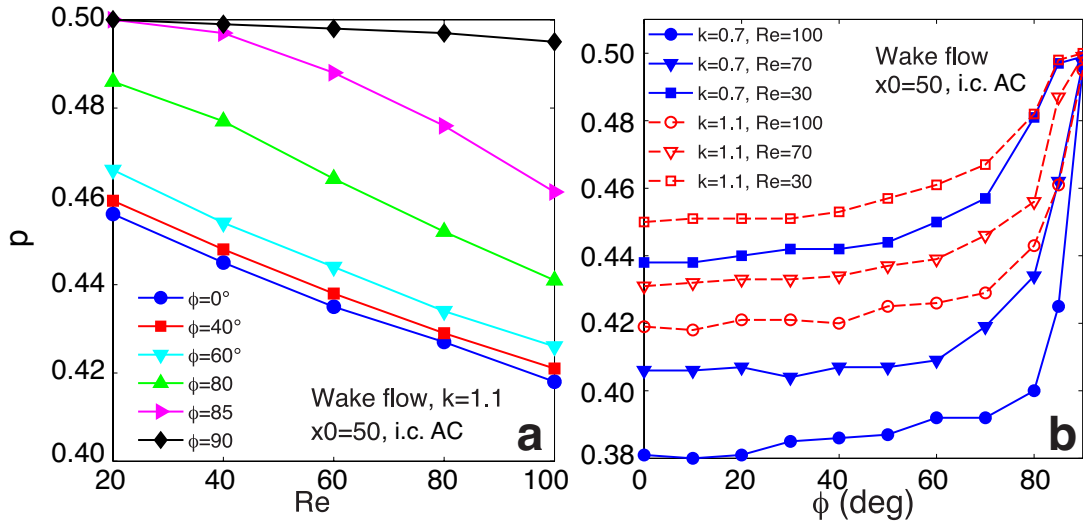


Figure 3.5: Scaling exponent  $p$  for the temporal evolution of the wake perturbation width in the intermediate term at  $x_0 = 50$  and with AC initial condition. (a) The exponent is represented as a function of the Reynolds number and it is parametrized with the obliquity angle in the range  $[0, \pi/2]$ . (b) The dependence on the obliquity angle is shown for  $Re = \{30, 70, 100\}$  and  $k = \{0.7, 1.1\}$ .

the perturbation itself reaches the wake high shear region. For this reason one of the relevant features of the initial condition is its centrality.

### 3.3 Power law scaling of the energy spectrum

The existence of an intermediate transient in which the perturbation presents characteristics of self similarity and the fact that set of small three-dimensional perturbations constitutes a system of multiple spatial and temporal scales lead as to wonder if there could be other similarities with turbulent flows. Indeed the three-dimensional disturbances are subject to all the processes included in the perturbative Navier-Stokes equations: linearised convective transport, molecular diffusion, linearised vortical stretching. Leaving aside the non-linear interaction among the different scales, these features are the same as those found in the turbulent state. In particular we query if a power-law scaling for the energy spectrum exist for an intermediate range of wavenumbers or frequency even in the linear dynamics of the perturbative Navier-Stokes equations and, if so, how does it compare, in terms of decay exponent and width of range where it applies, to the well-known  $-5/3$  Kolmogorov law for homogeneous fully developed turbulence?

In order to answer such questions, we study how the energy spectrum resulting from the analysis of a large set of solutions of the linearised perturbative Navier-Stokes equations be-

haves and we compare it with the energy spectrum of homogeneous fully developed turbulence. We perform this spectral analysis inside common phase of the perturbations life, i.e inside the intermediate transient. In this interval we have to decide in which instant compare the kinetic energy of the waves. We have to adopt a criterion that is valid for any wave numbers considered and which does not introduce an intrinsically scaling law.

To this aim, we have selected the instants, that we call **observation time**, at which the amplification factor reaches a given rate of variation, either in growth or in decay, that is the instant (inside the intermediate transient) at which

$$dG/dt = \pm \varepsilon$$

where  $\varepsilon$  is a given small constant value. Since unstable waves evolve much more rapidly than stable ones, it is convenient to use slightly different  $\varepsilon$  values in the two cases. In order to take the energy in instants equivalent to each other, the variation in absolute value of  $\varepsilon$  for stable waves goes from big to smaller values; while for the unstable waves it goes from smaller to bigger. In Figure 3.6 the results obtained for  $\varepsilon \in [10^{-4} - 10^{-2}]$  are presented.

Figure 3.6 top panels show where exactly this observation times defined with different  $\varepsilon$  are inside the intermediate transient. The beginning and the end of the intermediate transient are delimited by the black triangles. Panels (c,d) instead exhibit where the same observation time are collocated in respect to the temporal evolution of the amplification factor for two of the cases represented in top panels.

The main results is represented in panel (e-f) where the kinetic energy that the disturbances have at the observation time is represented as a function of the polar wavenumber in a log-log scale. The spectral values of  $G$ , for both the channel flow case (panel e) and the wake flow case (panel f) show a scaling in the intermediate range of the polar wavenumber ( $k \in [20, 200]$  for the channel,  $k \in [2, 150]$  for the wake) that is amazingly close to the turbulent canonical value of  $-5/3$ .

For shorter wavelengths, characterized by very short transients, the scaling is a little higher in magnitude, approximatively equal to  $-2$ . This result does not appear to be influenced to any great extent by the wave obliquity, the symmetry, or the  $Re$ , see Figure 3.7. However, it is possible to observe that purely orthogonal waves show a closer scaling to  $-2$  than to  $-5/3$ , even at intermediate wavenumbers.

In general, a full decade of intermediate wavenumbers can be observed for both the wall flow and the free flow. It is possible to show that the present results – in particular, the existence of an intermediate spectral range where the spectral decay exponent is very close to that of the Kolmogorov theory – do not depend on the choice of  $\varepsilon$  provided that the instant belongs to the intermediate transient.

These data gather all the stable waves occurring in the intermediate range (which is usually named inertial in turbulence jargon) and in the dissipative range. We would like to point out

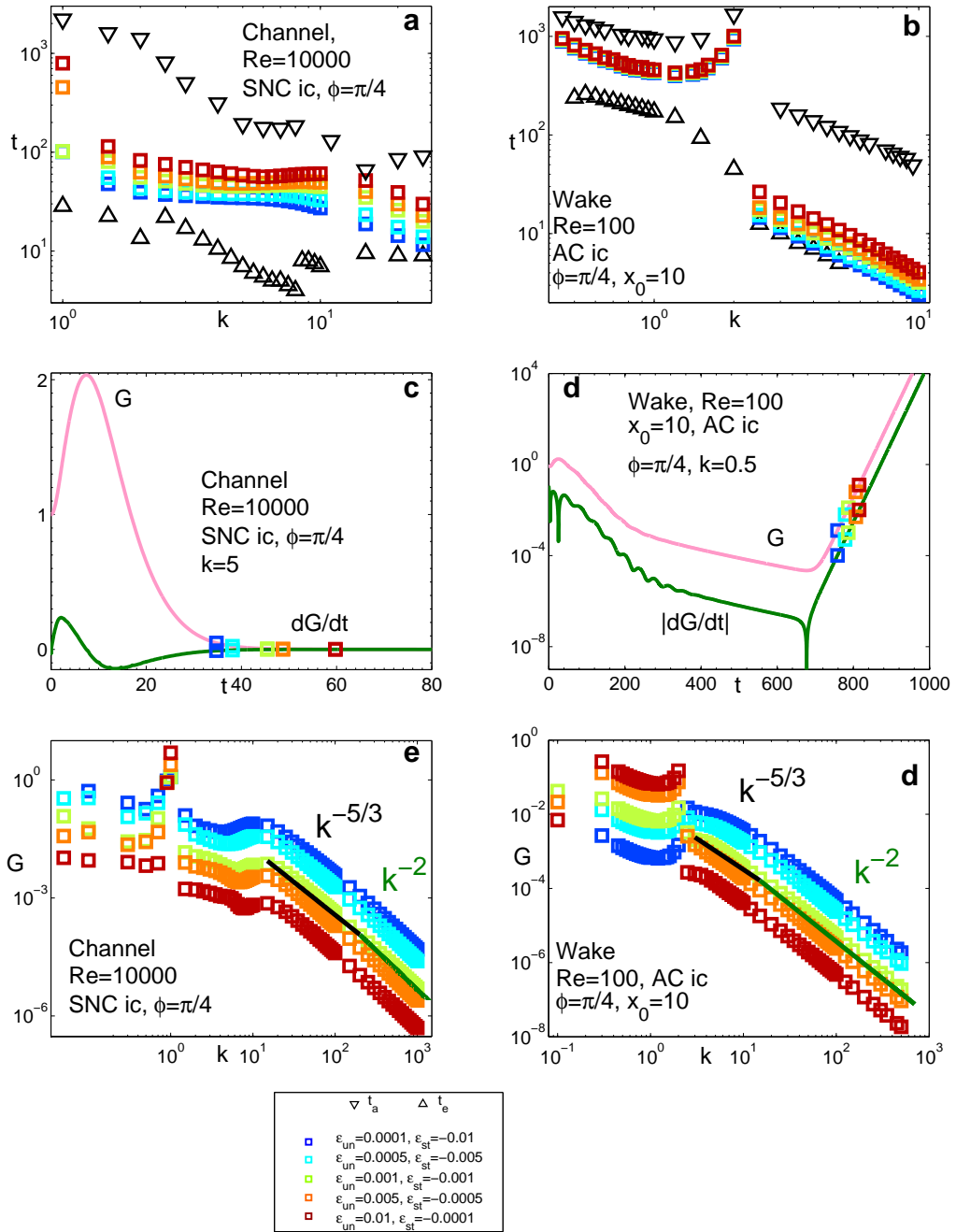


Figure 3.6: (a-b) Spectrum of the observation times where the wave energy is measured and compared referred to the limit of the intermediate transient (black triangles). (c-d) Position of the observation times inside the amplification factor transient. (d-e) Energy spectra computed at the times shown in top panels. The legend in the bottom panel specifies the symbols associated with either the results of the present study or those of the laboratory and numerical experiments carried out on fully turbulent flow fields by other authors.

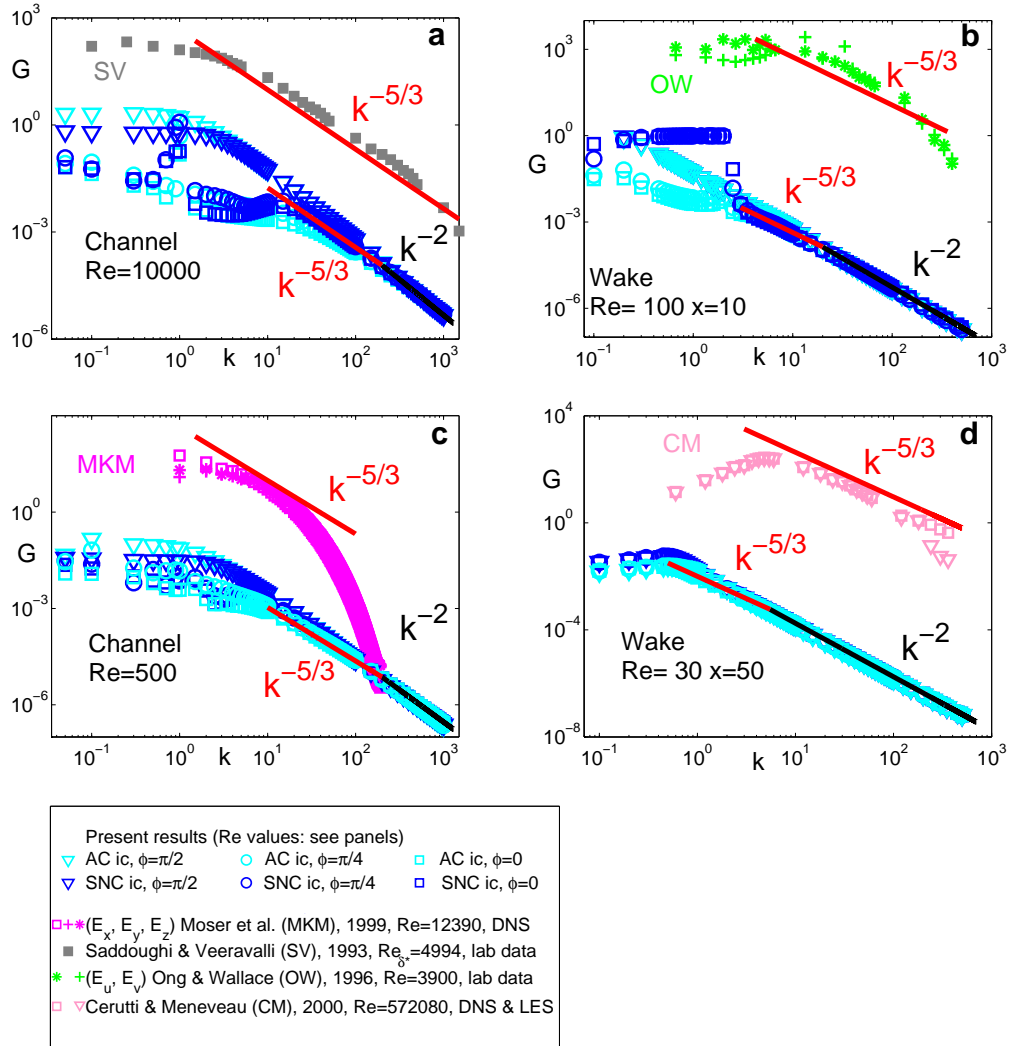


Figure 3.7: Spectra of the amplification factor  $G$  for the collections of linear travelling waves observed at the time,  $|T_e : dG/dt(T_e)| = 0.001$ , where the perturbations are out of their transient. Our results concern both stable flow configurations (*a, b*) and unstable ones (*c, d*). The spectra obtained in this study have been compared qualitatively with the turbulent field spectra available in the literature and obtained from laboratory or numerical experiments. The legend in the bottom panel specifies the symbols associated with either the results of the present study or those of the laboratory, and numerical experiments carried out on fully turbulent flow fields by other authors.

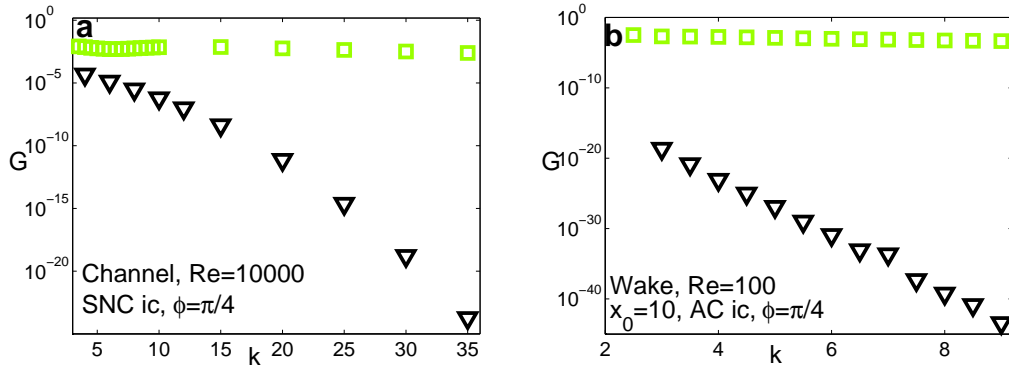


Figure 3.8: Comparison between the energy spectrum observed in the intermediate transient (green squares) and the energy spectrum observed at the asymptote (black triangles).

that the data do not highlight a dependence on  $Re$ , the flow control parameter. For longer waves ( $k < 10$  and  $k < 1 - 2$  for the plane Poiseuille flow and the bluff-body wake, respectively), the results depend on the perturbation inclination, the symmetry of the initial condition, and on the boundary conditions (geometry of the system). As expected, they do not reveal any universal behavior. In Fig. 3.7, panels a-b-c-d, experimental (laboratory and numerical) measurements [99, 119, 22, 106] in the turbulent states have been included for the sake of comparison of stable linear perturbations and turbulent scales.

However it is really important to stress that these results are obtained inside the intermediate transient. If instead we compare the residual energy that the waves have at the instant in which they reach the asymptotic regime, i.e. when the growth rate and frequency have reached their asymptotic values, we get completely different energy spectrum, as shown in figure 3.8.

Taking into account the present results, it is possible to say that the non-linear interaction distributes the relative energy over different wavenumbers in a way that corresponds to the that energy each wave has when during the intermediate transient it reaches a common decay threshold.

This sheds some light on the existence of some common linear and non-linear Navier-Stokes solutions properties, and helps one to consider them as a whole. In particular, we consider it is important to explore the collective behaviour of the linear solutions by thinking of them as a set of multiple elements that fill the wavenumber range which pertains to the geometry of the system. By means of a comparison of the various elements, or, possibly, by means of an observation of their collective behaviour, this multiplicity may either reveal trends that are common to the non-linear dynamics or highlight their differences.



## Chapter 4

# Cross Flow Boundary Layer

Until now we have considered the two-dimensional base flows, but we think it is also interesting to see how the stability properties change if a three-dimensional base flow is perturbed. For this reason we consider the boundary layer in cross flow. The study of three-dimensional boundary layers is motivated by the need to understand the fundamental instability mechanisms that cause transition in swept-wing flows.

The cross flow boundary layer is one of the most important boundary layers in engineering applications (aerospace, mechanical, wind...). Examples of cross flow boundary layer include flow over a swept back air plane wing, rotating discs, cones and spheres and cones at an angle of attack. It is important to understand the dynamics of this flow and to learn how to prevent the possibility of breakdown to turbulence. Furthermore, unlike the well-known Blasius boundary layer, breakdown is far more likely in this flow. For example, it can be unstable inviscidly as well as that caused by the influence of viscosity due to the existence of an inflexion point in the mean profile [47]. This chapter presents a study in an extended portion of the parameter space of the stability of the cross flow boundary layer in supercritical conditions with three-dimensional perturbations based not only on the modal approach but also examining the temporal evolution of the perturbation.

Flow due to an infinite rotating disk often has been used in literature as an archetypal example of three-dimensional boundary layers [121]. Lingwood in 1995 [77] found that in this flow a transition from local linear convective to radial absolute instability can occur. This inspired many authors and led to the investigation of the fully non linear regime (see, among others the paper of Pier [111] and Healey [53]).

The swept-wing boundary layer is genuinely three-dimensional, which makes its exploration very complex. Despite this complexity, Lingwood's approach motivated studies on the possibility of absolute instability operating in the swept-wing boundary layer. In particular, it was found that close to the attachment line there is chordwise absolute instability above a critical spanwise Reynolds number of about 545 [78]. Taylor and Peake [133] extended the

study by Lingwood and searched for pinch points in the cross flow direction for a larger range of flow angles and pressure gradients. Although these crossflow-induced pinch points do not constitute an absolute instability, as there is no concomitant pinch occurring in the streamwise wavenumber plane, they can be used to find the maximum local growth rate contained in a wavepacket travelling in any given direction. Recently, these findings were confirmed by Koch [71] in a work dedicated to the study of the secondary instability of stationary cross-flow vortices. In general, a rigorous proof that the absolute instability cannot occur in a swept-wing boundary layer does not yet exist.

The three-dimensional boundary layer has been also investigated in the context of receptivity and transient optimal perturbations. Most studies of optimal disturbances in wall-bounded flows [81, 82] deal with temporal growth of perturbations. For example, Corbet and Bottaro [27] performed a local stability analysis using a variational technique in the temporal framework. They found that the three-dimensional boundary layer shows significantly greater capacity for algebraic growth than the two-dimensional boundary layer with the same base flow parameters. Moreover, they proved that the cross flow angle that maximizes the transient growth is nearly equal to  $49^\circ$ . Schrader et al. [126] and Tempelmann et al. [134] studied the receptivity problem for spatial growing perturbation considering vortical free stream modes, free stream turbulence and surface roughness. They found that steady cross-flow instabilities to dominate for low-level free stream disturbance.

Malik et al. [86, 87] investigate the secondary instability characteristics of swept-wing boundary and found that three types of secondary disturbances can be distinguished. The first two were high-frequency disturbances with high growth rates and maxima located away from the wall. Their origin was related to regions of high spanwise shear (type I) and vertical shear (type II). The third type is a low-frequency disturbance with smaller growth rates and maxima closer to the wall representing a primary traveling crossflow disturbances being modulated by the stationary crossflow vortex.

With this study we treat the linear perturbation problem and demonstrates the importance of the results during the transient period as well the long time behaviour [32]. Near-optimal perturbations which are localized within the boundary layer thickness are used as initial conditions [73, 27]. We also have good agreement with results obtained by using impulsive forcing [133] or least-damped Orr-Sommerfeld eigenfunctions as initial conditions [20]. The extreme simplicity of this method allows for an extended study of the parameter space. In particular, special attention was given to the role played by the direction of the perturbation both in the transient and in the asymptotic regime. In sub-critical conditions, a similar analysis was performed by Breuer and Kuraishi [20]. They observed that, when the external flow is accelerated, the disturbances which have greater transient growth are those that propagate in the crossflow direction. Vice versa, if the external flow is decelerated, the maximum transient growth is obtained with disturbances propagating in the opposite cross-flow direction.

With this study we wish to extend the study of Breuer and Kuraishi by considering su-

percritical conditions. The pressure perturbation during the transient is also investigated. We observe that the maximum amplification factor for the pressure measured at the wall is not synchronous with the maximum amplification of the energy.

This chapter is organized as follow. The physical problem is described in Section 4.1. Subsection 4.1.1 is dedicated to the mean three-dimensional flow, subsection 4.1.2 to the definition of the initial value problem and modal analysis. Sections 4.2 and 4.3 present transient dynamics and the role of the perturbation inclination and the long term behaviour, respectively. Section 4.5 gives information on the wall pressure transient.

## 4.1 Physical Problem

### 4.1.1 Mean flow configurations

For the present study we assume that locally we can represent the boundary layer as a parallel shear flow. Mathematically, good approximation of the velocity profiles in a three dimensional boundary layer is given by the family of similarity solutions known as Falkner-Skan-Cooke (FSC) boundary layers, [26], where the magnitude of the cross-flow can be varied in a systematic manner.

Let us define a local coordinate system as shown in Figure 4.1(a). On an infinite swept wing, taken any point  $x^*$  lying on the wing, we can always distinguish the chordwise direction,  $x_c$ , from the streamline direction,  $x$ .

In the coordinate system based on the chordwise direction, we can assume that the base flow is steady, incompressible, irrotational. We assume also that the free stream velocity depend only on the streamwise direction,  $U_\infty = U_\infty(x_c)$  and  $W_\infty = W_\infty(x_c)$ . In particular, the FSC profiles are characterized by a power law dependence of the streamwise free-stream velocity on the streamwise coordinate direction and zero spanwise free stream velocity

$$U_\infty(x_c) = Cx_c^m, \quad W_\infty = 0 \quad (4.1)$$

Since the flow is irrotational we can apply the Bernoulli principle and write the pressure term as follow

$$-\frac{1}{\rho} \frac{\partial p_e}{\partial x_c} = U_\infty \frac{dU_\infty}{dx_c}$$

The Navier-Stokes equations that describe the infinite swept flat plane boundary layer accord-

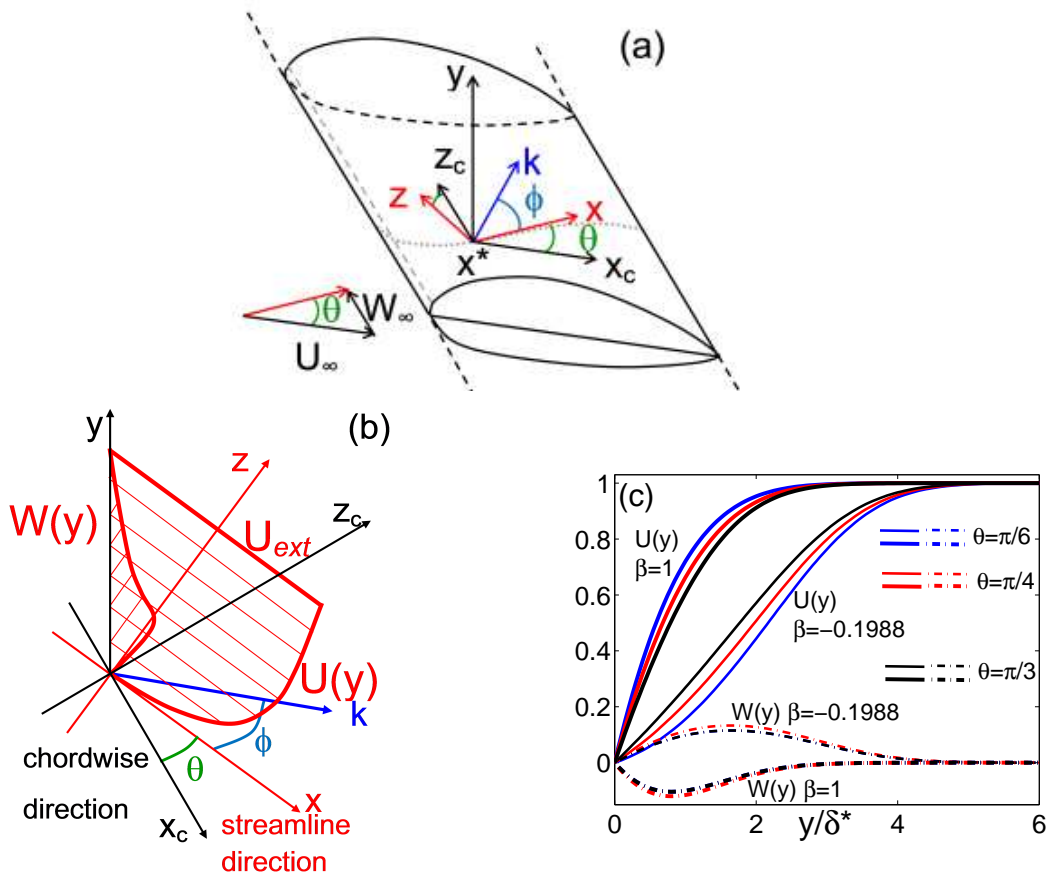


Figure 4.1: Flow scheme. (a) Chordwise  $(x_c, y, z_c)$  and streamline  $(x, y, z)$  reference frame. The cross flow angle,  $\theta$  is represented in green while the direction in which the perturbation propagate,  $k$  is in blue.  $\phi$  is the angle of obliquity between the streamline and the perturbation direction. The attachment line is shown as a dashed line, the external streamline is indicated by the dotted line. (b) Three dimensional representation of the boundary layer velocity profiles,  $U(y)$  and  $W(y)$ , in the plane aligned with the external streamline. (c) Solutions of the Falkner Skan Cooke flow. Effect of changing the parameters:  $\beta = -0.1988, 1$  and  $\theta = \pi/6, \pi/4, \pi/3$ .

ing to [124] become

$$u \frac{\partial u}{\partial x_c} + v \frac{\partial u}{\partial y} = U_\infty \frac{dU_\infty}{dx_c} + v \frac{\partial^2 u}{\partial y^2} \quad (4.2)$$

$$u \frac{\partial w}{\partial x_c} + v \frac{\partial w}{\partial y} = v \frac{\partial^2 w}{\partial y^2} \quad (4.3)$$

$$\frac{\partial u}{\partial x_c} + \frac{\partial v}{\partial y} = 0 \quad (4.4)$$

with the boundary conditions

$$u = v = w = 0 \text{ at } y = 0 \quad (4.5)$$

$$u \rightarrow U_\infty, w \rightarrow W_\infty \text{ as } y \rightarrow \infty \quad (4.6)$$

where  $u, v, w$  are the chordwise ( $x_c$ ), normal ( $y$ ) and spanwise ( $z_c$ ) velocity components, respectively (see black curves in Figure 4.1a).

A self-similar solution may be found if we select

$$\eta = y \sqrt{\frac{U_\infty}{2\nu x_c}} \quad (4.7)$$

Introducing the stream function

$$\Psi = \sqrt{U_\infty \nu x_c} f(\eta) \quad (4.8)$$

(with  $u = \partial\Psi/\partial y$  and  $v = -\partial\Psi/\partial x$ ) and

$$w = W_\infty g(\eta) \quad (4.9)$$

reduces the boundary layer equations to a function of the single variable  $\eta$ , and we have

$$f''' + ff'' + \beta(1 - f'^2) = 0 \quad (4.10)$$

$$g'' + fg' = 0 \quad (4.11)$$

where  $\beta$  is called Hartree parameter or dimensionless pressure gradient. It is defined as

$$\beta = \frac{2m}{(m+1)} \quad (4.12)$$

Here the boundary conditions are

$$f = f' = g' = 0 \text{ if } \eta = 0 \quad f \rightarrow 1, g \rightarrow 1 \text{ as } \eta \rightarrow \infty \quad (4.13)$$

Conventionally stability is studied in the the external streamline frame of references, see red lines in Figure 4.1(a-b). If we introduce the cross flow angle,  $\theta$ , which is the angle between the external streamline direction and the chordwise direction

$$\theta = \arctan\left(\frac{W_\infty}{U_\infty}\right) \quad (4.14)$$

the velocity components parallel and normal to the external flow are given by

$$U(y) = f'(\eta) \cos^2 \theta + g(\eta) \sin^2 \theta, \quad (4.15)$$

$$W(y) = [g(\eta) - f'(\eta)] \cos \theta \sin \theta \quad (4.16)$$

Figure 4.1(b-c) shows the velocity profiles in this referenceframe. The variables are nondimensionalized by the streamwise displacement thickness,  $\delta^*$  and streamwise velocity component of the undisturbed flow.

Summarizing, there are two parameters in the FSC formulation that allow the magnitude of the cross flow to be varied:  $\theta$  the crossflow angle and  $\beta$ , the dimensionless pressure gradient. Note that with this approximation

$$\frac{\partial p_e}{\partial x_c} = -m\rho C^2 x_c^{2m-1}$$

therefore the external flow is accelerating as the pressure decrease ( $\beta, m > 0$ ) and one can talk of boundary layer in a **favourable pressure gradient**. On the contrary the external flow is decelerating as the pressure rises ( $\beta, m < 0$ ) and one talks of an **adverse pressure gradient**.

The profiles 4.11 will be used here as base flow in the stability investigation of three dimensional disturbances.

### 4.1.2 Initial-value problem and modal analysis

The transient as well as the long term behaviours of arbitrary three-dimensional disturbances acting on the FSC cross-flow boundary layer are investigated. We have considered the velocity vorticity formulation and have Fourier transformed the governing disturbance equations in the streamwise and spanwise directions only, using respectively the wave numbers  $\alpha$  and  $\gamma$  (see also Chapter 1 for major details). This leads to generalized forms of the Orr-Sommerfield and Squire equations:

$$\begin{aligned} \left( \frac{\partial}{\partial t} + i(\alpha U + \gamma W) \right) \left( \frac{\partial^2}{\partial y^2} - k^2 \right) \hat{v} - i(\alpha U'' + \gamma W'') \hat{v} - \frac{1}{Re} \left( \frac{\partial^2}{\partial y^2} - k^2 \right)^2 \hat{v} = 0 \\ \left[ \frac{\partial}{\partial t} + i(\alpha U + \gamma W) - \frac{1}{Re} \left( \frac{\partial^2}{\partial y^2} - k^2 \right) \right] \hat{\omega}_y = i(\alpha W' - \gamma U') \hat{v} \end{aligned} \quad (4.17)$$

where  $k^2 = \alpha^2 + \gamma^2$  is the polar wavenumber,  $\hat{v}$  and  $\hat{\omega}_y$  are respectively the transformed perturbation vertical velocity and vorticity,  $U$ ,  $U'$ ,  $U''$ ,  $W$ ,  $W'$  and  $W''$  indicate the base flow streamwise and spanwise profiles and its derivatives in the  $y$  direction. The boundary conditions require that  $\hat{v} = \hat{v}' = \hat{\omega}_y = 0$  at the wall and at infinity.

On these equation we have performed both a modal analysis and an initial value problem, which thereafter will be indicated with the abbreviation IVP, as described in Section 1.4. We have considered supercritical flows ( $Re=1000-5000$ ) subject to positive and negative pressure gradient ( $\beta = -0.1988, 1$ ). The cross-flow angle,  $\theta$ , is taken in the range  $[\pi/12, 5\pi/12]$ . Concerning the perturbations, we vary both the polar wavenumber,  $k$ , and the angle of obliquity  $\phi$ , defined as the angle between the streamwise and the perturbation directions,  $\phi = \arctan(\gamma/\alpha)$ , see Figure 4.1(a-b). For the IVP as initial condition we have chosen a Gaussian distribution for the velocity field, while the vorticity is initially zero, namely

$$v(0) = y^2 \exp(-y^2), \quad \omega_y(0) = 0 \quad (4.18)$$

However, in order to make some comparison with literature data, in section 4.2 we have performed simulations with different initial condition at  $Re = 500$  and  $\beta = 0.2$ .

### Codes Validation and confirmation of previous results

To validate the numerical procedure, both numerical solutions are compared with each other and with the data in the literature, see Figure 4.2. Panel (a) shows a really good agreement with the results of Taylor and Peak [133] for both the modal approach and the IVP. Since we have not found many spectra for the cross flow boundary layer, in panel (b) we have considered as base flow the Blasius boundary layer and contrasted our results with Mack [85].

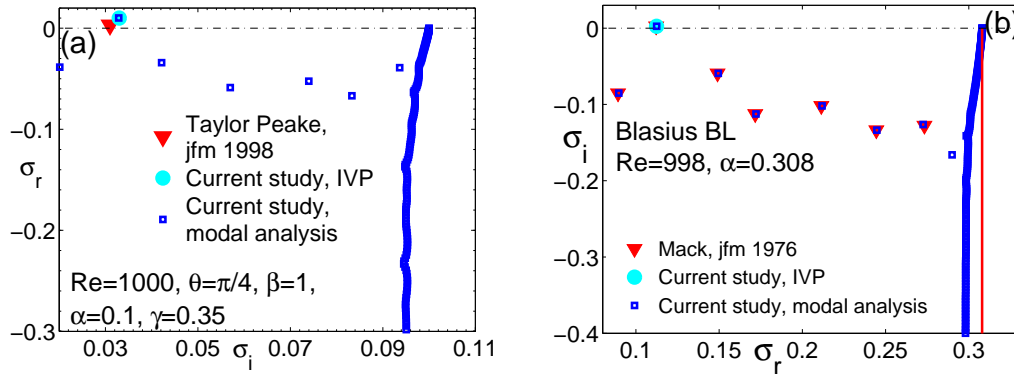


Figure 4.2: Spectra of eigenvalues ( $\sigma = \sigma_r + i\sigma_i$ ) of the Orr-Sommerfeld equation. Comparison of different numerical methods: 4<sup>th</sup> order finite differences scheme on uniform grid (blue square); initial value problem (cyan circle); literature data (red triangle). (a) Cross flow boundary layer  $Re_{\delta^*} = 1000$ ,  $\beta = 1$ ,  $\theta = \pi/4$ ,  $\alpha = 0.01$ ,  $\gamma = 0.35 + i0.125$ . Comparison with Taylor and Peake data [133]. (b) Blasius boundary layer flow,  $Re_{\delta^*} = 998$ ,  $k_{\delta^*} = 0.308$ ,  $\phi = 0$  contrasted with Mack 1976 [85]. Please note that with our approach the continuous part of the spectrum is discretely approximated. The red line represents the analytical solution, obtainable relaxing the boundary condition to infinity.

## 4.2 Transient dynamics and role of the obliquity angle

As mentioned in the introduction we want to extend the results of Breuer and Kuraishi [20] to the case of supercritical flow. As initial condition they use the least-damped Orr-Sommerfeld eigenfunction for the velocity field and set the vertical vorticity equal to zero. See in Figure 4.3(a) the comparison between their initial condition extending outside the boundary layer and the initial condition defined in Eq. 4.18. Breuer and Kuraishi consider stable waves and found that transient growth can be observed in a narrow range of wavenumbers ( $k \in [0.2, 1.1]$ ). Within this region, they observe that for positive  $\beta$  positive values of  $\phi$  show a greater transient growth than those with negative values, see panel (c), and the peak value is achieved for an obliquity angle of about  $80^\circ$  ( $9/20\pi$ ). For negative value of  $\beta$ , the opposite is true and the peak value is reached for an obliquity angle of about  $-80^\circ$ .

To further validate our simulations we have done some simulation using their initial condition, as done also by Corbett and Bottaro [27] (see figure 3 therein), getting a very good agreement, see blue squares in Figure 4.3 panels (b) and (c). In panel (c), the transient growth obtained with the initial condition 4.18 is again contrasted with Breuer and Kuraishi results. We also have a point of comparison with an optimal perturbation at a similar sweep angle ( $48.8^\circ$ ) obtained by Corbett and Bottaro. It should be noted that according to literature [73, 27], our kind of initial condition fully confined within the boundary layer promotes the initial energy gain. However, in this study we are not focusing on the use of optimal initial conditions, but we simply wish to describe how in supercritical condition the obliquity of arbitrary perturbation



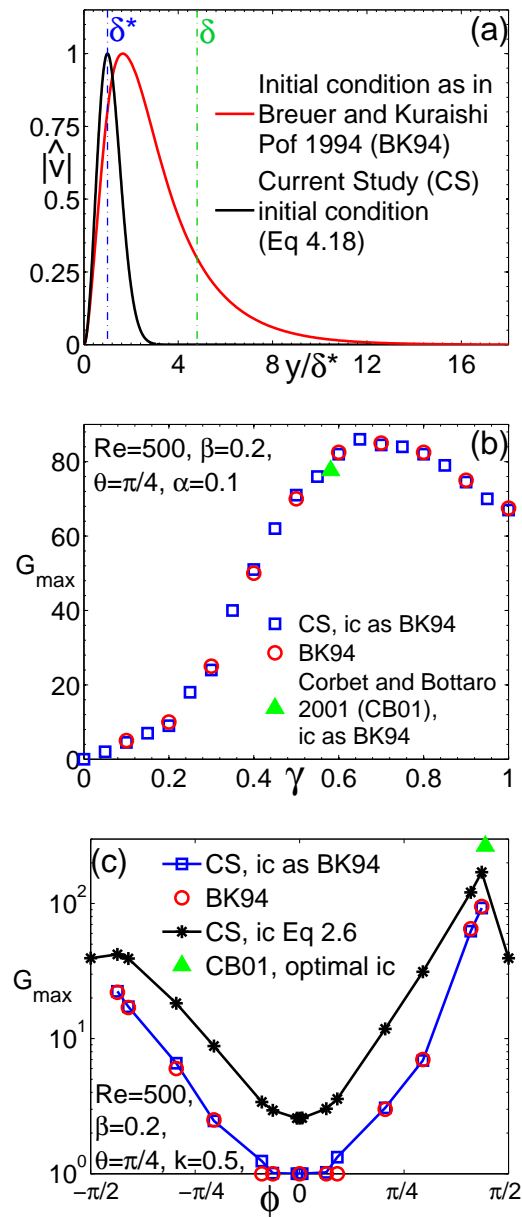


Figure 4.3: Comparison between the current study and Breuer and Kuraishi (BK94). (a) Their (red) and our (black) initial condition profile. Vertical dash-dotted lines indicate the displacement thickness and the boundary layer width. (b-c) Numerical results at  $Re = 500$ ,  $\beta = 0.2$  and  $\theta = \pi/4$ . Red circles indicate results from BK94, green triangles show results by Corbet and Bottaro (CB01) [27], blue squares are the reproduction of results in BK94 made with our numerical procedure using their initial condition, black asterisks are the transient growths obtained by the initial condition Eq.4.18.(b) Maximum of the amplification factor as a function of the spanwise wavenumber with  $\alpha = 0.1$  and initial condition as in BK94. (c) Maximum of the amplification factor as a function of the the obliquity angle at  $k = 0.5$ . Results in CB01 are obtained at  $\theta = 48.8$  using an optimal initial condition.

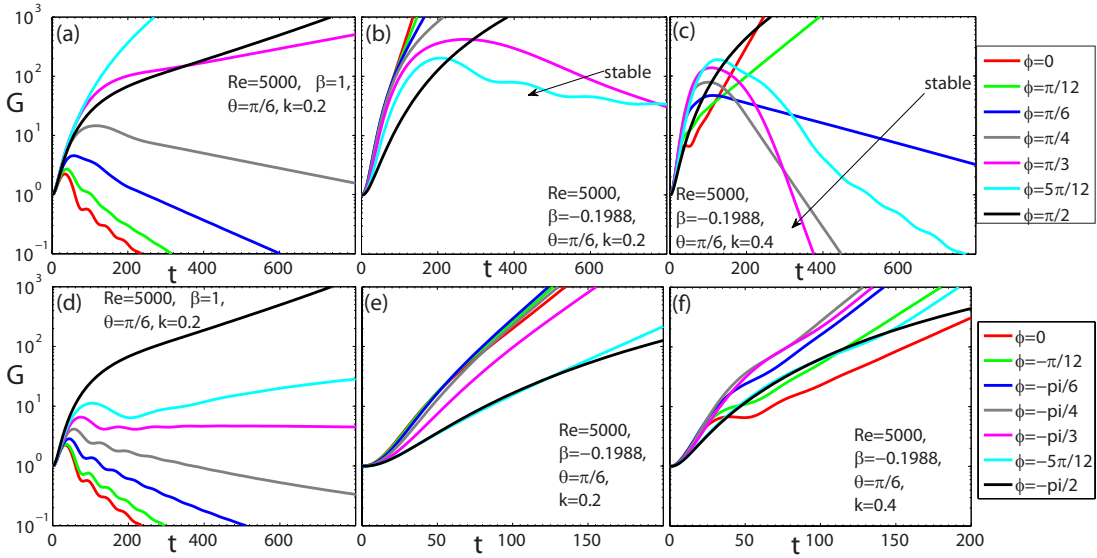


Figure 4.4: Temporal evolution of the amplification factor,  $G(t)$  for perturbations with different obliquity angles,  $\phi = 0, \pi/12, \pi/6, \pi/4, \pi/3, 5\pi/12, \pi/2$  at  $Re = 5000$  and  $\theta = \pi/6$ . Left panel  $\beta = 1$ , middle and right panels  $\beta = -0.1988$ . Panels (a,b,d,e)  $k = 0.2$ , panels (c,f)  $k = 0.4$

can influence its evolution.

Figure 4.4 shows the temporal evolution of the amplification factor for perturbation with different obliquity angles at the supercritical Reynolds number of 5000. Fixing the wavenumber, when the external flow is accelerated, the growth rate increases with the positive angle of obliquity up to  $\phi = 5/12\pi$  and then slightly decreases, see panel (a), while for negative angles the increase is monotonic, see panel (d). One can also note that in case of transient growth the maximum of  $G$  is monotonically increasing with the modulus of  $\phi$ . When the external flow is decelerated a rather general rule can be found. When considering positive angles of obliquity, Figure 4.4 (panels (b),  $k = 0.2$  and (c),  $k = 0.4$ ) highlights a rich and, for certain aspects, counter-intuitive scenario on the role of the perturbation direction. We see in fact that the waves with small obliquity together with the orthogonal waves are unstable but a range of oblique waves in between are not. Usually, in 2D shear flows, if one sees instability in the longitudinal direction, one then sees a progressive tendency to stability moving toward the orthogonal direction. Instead, here, intermediate angles have an intense initial growth and then become stable. When considering negative angles of obliquity (panels (e),  $k = 0.2$  and (f),  $k = 0.4$ ), we see that the waves do not present significant transient growth and are all unstable.

It should be noted that for the cases in panels (a,b,c) in Figure 4, perturbations beyond  $\phi = \pi/3$  (i.e.  $\theta + \phi > \pi/2$ ) propagate toward the attachment line of the wing. These travelling waves are unstable for  $\beta = 1$  and are transiently growing for  $\beta = -0.1988$ . This is a

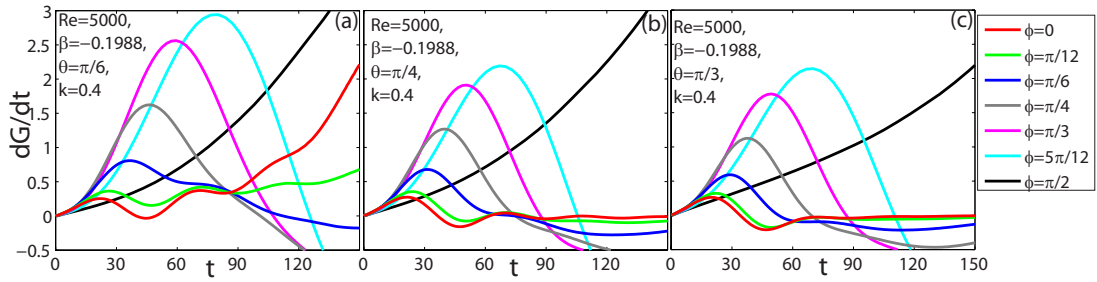


Figure 4.5: Temporal evolution of the amplification factor growth,  $dG(t)/dt$  for perturbations with different obliquity angles,  $\phi = 0, \pi/12, \pi/6, \pi/4, \pi/3, 5\pi/12, \pi/2$  at  $Re = 5000$ ,  $\beta = -0.1988$  and  $k = 0.4$ . Panel (a),  $\theta = \pi/6$ . Panel (b),  $\theta = \pi/4$ . Panel (c),  $\theta = \pi/3$ .

very dangerous possibility since the growth of these disturbances can contaminate the attachment line region. Note that in this case transient growths are more intense than the growths of asymptotically unstable waves, as can be seen in Figure 4.5, where for the same time instant in the transient, the asymptotically stable waves show a transient increase up to six times faster than that of the unstable waves. According to Lingwood [78], modes propagating along the span may be able to reach non linear amplitudes and trigger transition before being convected beyond the wing tip.

### 4.3 Long-term behaviour

Regarding the influence of the angle of obliquity on the long-term behaviour, the best way to study it is by means of the modal analysis. In fact, considering the large number of parameters involved, with the IVP the knowledge of the final growth rate of a perturbation would require a large computational effort and a large memory space to store the temporal results (there are simulations that can last up to  $10^5$  time scales). In Figure 4.6, for different combinations of obliquity angle, pressure gradient and cross-flow angle and two different wavenumbers taken in the range of the most unstable one, one can see the growth rate computed as the imaginary part of the least damped eigenvalue in the discrete spectrum. Taylor and Peake [133] have also investigated the combined effect of  $\beta$  and  $\theta$ . Considering wavenumbers supporting pinch points, they found that asymptotically the perturbations with an adverse pressure gradient flow are more unstable at lower cross flow angles, while for negative pressure gradient the opposite is true. Our results are completely in agreement with their observations. Summarizing the situation, by changing the sign of Hartree's parameter, the sign of the growth rate changes. A concentration of the growth factor values that become nearly constant in the range  $[-60, 60]$  is observed for the accelerated boundary layer at  $k = 0.4$ , see panel (c) of Figure 4.6. A less intense similar trend is observed in panel (d) for the same configuration with a positive pressure

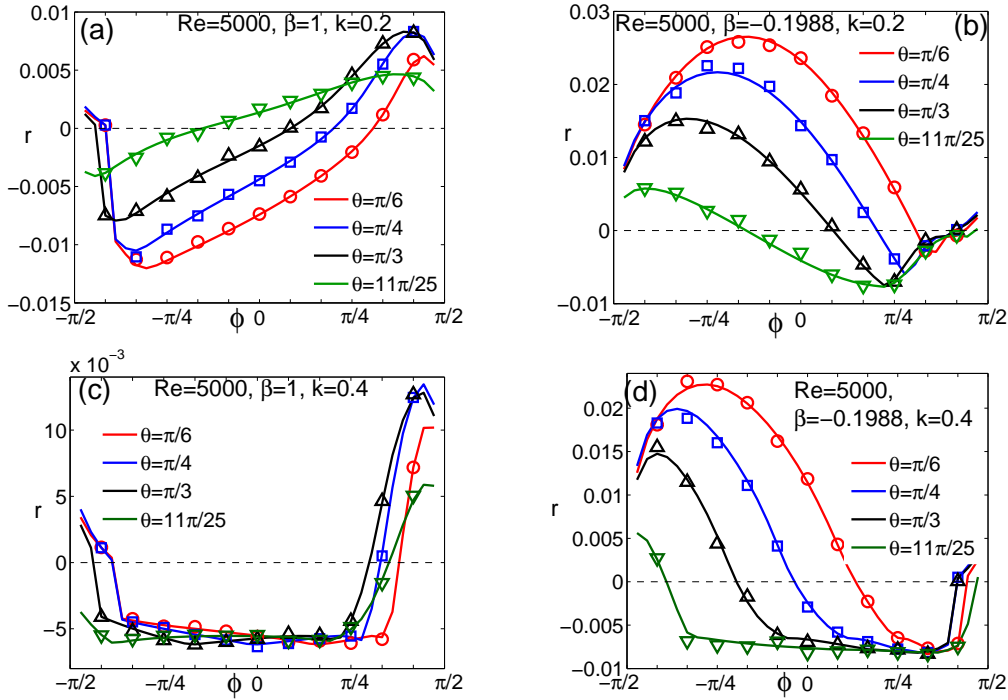


Figure 4.6: Growth rate as a function of the obliquity angle for different cross flow angles:  $\theta = \pi/6$  (red line),  $\theta = \pi/4$  (blue line) and  $\theta = \pi/3$  (black line). Circle, triangles and squares are values computed by the IVP and reported here to further validate the numerical results. Left panels positive pressure gradient. Right panels negative pressure gradient. Top panels  $k = 0.2$ . Bottom panels  $k = 0.4$

gradient.

We can define two thresholds of the obliquity angle for which the growth rate reaches its minimum negative value,  $\phi_{min}$ , and its maximum positive value,  $\phi_{max}$ . These thresholds are slightly decreasing with the cross flow angle and almost constant with the Reynolds number. The behaviour with the wavenumber, in the range  $[0.02 - 1]$ , is a bit more structured as shown in Figure 4.7 panel (b). When the external pressure gradient is positive (dashed lines)  $\phi_{max}$  and  $\phi_{min}$  are general decreasing function of the wavenumber. For  $\beta = 1$  (solid lines), both  $\phi_{min}$  and  $\phi_{max}$  present a local mild minimum at the long wave where  $k = 0.1$ . Furthermore  $\phi_{min}$  has a local maximum at  $k = 0.4$ .

Summarizing, for a given  $\theta$  and  $\beta$  the Reynolds number dependence of the obliquity angle of the most unstable waves is very weak. This suggests that this instability is essentially an inviscid mechanism.

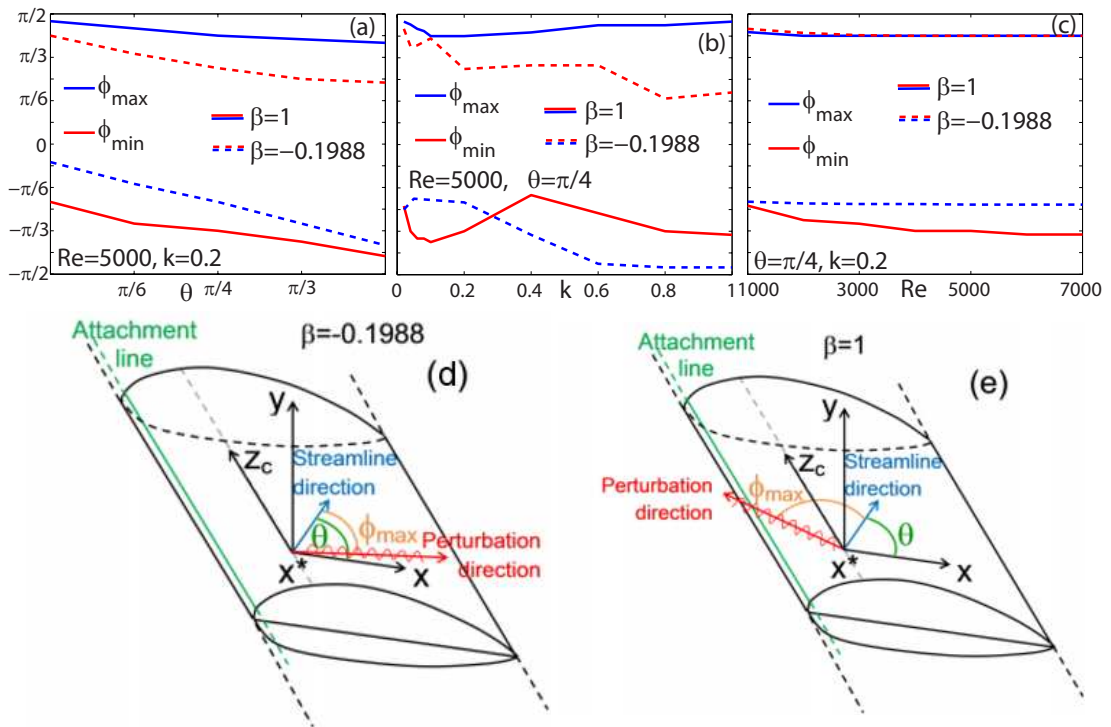


Figure 4.7:  $\phi_{\min}$  and  $\phi_{\max}$ , obliquity angle for which the growth rate reaches respectively its minimum negative value and its maximum positive value, as a function of the base flow and the perturbation parameters. Solid lines  $\beta = 1$ , dashed lines  $\beta = -0.1988$ . Panel (a) shows their dependency on the cross flow angle for perturbations at  $Re = 5000, k = 0.2$ . Panel (b) represents  $\phi_{\min}$  and  $\phi_{\max}$  as a function of  $k$  for waves at  $Re = 5000, \theta = \pi/4$ . Panel (c) shows the trends with the Reynolds number in the case  $k = 0.2, \theta = \pi/4$ . (d,e) Scheme of the direction of the perturbation with maximum growth for  $\beta = -0.1988$  and  $\beta = 1$  respectively.

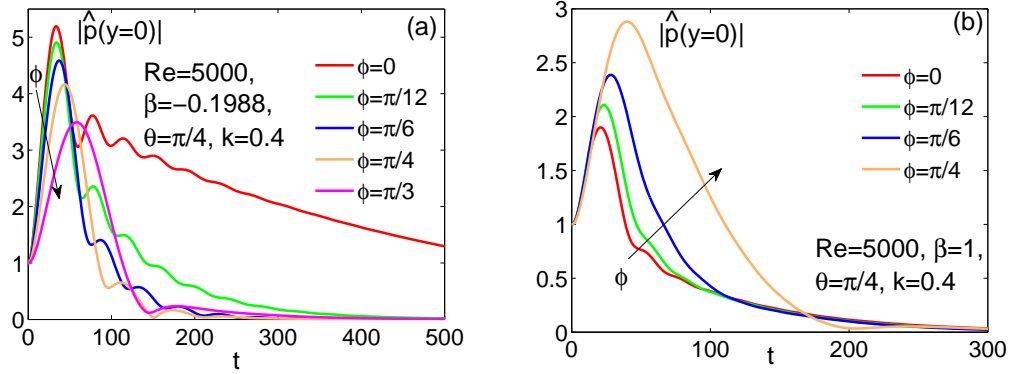


Figure 4.8: Role of the obliquity angle in the pressure transient,  $\phi = 0, \pi/12, \pi/6, \pi/4, \pi/3, 5\pi/12, \pi/2$ . Pressure amplification,  $P$ , temporal evolution.  $Re = 5000$ ,  $\theta = \pi/4, k = 0.4$ . Panel a  $\beta = -0.1988$ , panel b  $\beta = 1$ .

#### 4.4 Perturbed pressure transient

Probably due to the fact that the flow considered is incompressible, the perturbed pressure dynamics have been poorly investigated. However knowing how the pressure behaves on the wing is of obvious interest to the aerodynamics. For this reason we analyse the evolution of the perturbed pressure at the wings and we found a behaviour that is not easily predictable by the amplification factor evolution. The pressure field is computed by the Poisson equation,

$$\Delta \hat{p} = -ik(\cos(\phi)U' + \sin(\phi)W')\hat{v} \quad (4.19)$$

and boundary conditions

$$\hat{p}(y \rightarrow \infty) = 0, \quad \hat{p}'(y = 0) = \hat{v}''(y = 0)/Re \quad (4.20)$$

As in the previous section, we are interested in the role of the obliquity angle. For this purpose we define the equivalent of the amplification factor for the pressure:

$$P = |\hat{p}(y = 0, t)|/|\hat{p}(y = 0, t = 0)| \quad (4.21)$$

that we can call pressure amplification. Now we consider only the stable waves that, as mentioned above, with the initial condition applied, have always a transient energy growth. Top panel in Figure 4.8 shows the time evolution of the pressure amplification for  $\theta = \pi/4, k = 0.4$ , positive (panel a) and negative (panel b) pressure gradient. As expected the pressure field is also initially amplified. For adverse pressure gradient, once is reached its maximum value the pressure has a modulated damping. Moreover in this case the maximum value of the pressure

amplification,  $P_{max}$ , is always higher than in the case of  $\beta = 1$ . Finally we can observe that  $P_{max}$  decreases with the obliquity angle for  $\beta = -0.1988$  while it increases with  $\phi$  in the other case.

This behaviour is better represented in the bottom panels of Figure 4.9 where is reported  $P_{max}$  (circles) together with the maximum of the amplification factor  $G_{max}$  (triangles) and the time difference in which the two maxima are reached  $\Delta T = t(G(t) = G_{max}) - t(P(t) = P_{max})$  (squares), for the same configurations of figure 4.9. In panels c and d is reported  $P_{max}$  (circles) together with the maximum of the amplification factor  $G_{max}$  (triangles) and the time difference in which the two maxima are reached  $\Delta T = t(G(t) = G_{max}) - t(P(t) = P_{max})$  (squares) as a function of the obliquity angle. We can observe that  $P_{max}$  decreases with the obliquity angle for  $\beta = -0.1988$  while it increases with  $\phi$  in the other case. In the case of favourable pressure gradient (panel c) we observe that all the quantities increase with the obliquity angle. In the other case instead  $P_{max}$  decreases with  $\phi$  while  $G_{max}$  grows.  $\Delta T$  doesn't have a monotone behaviour: increases initially than reach a maximum at  $\phi = \pi/6$  and decrease. Please note that  $\phi = \pi/6$  also correspond to the obliquity angle at which the growth rate is minimum for this configuration. We also investigate the role of the wavenumber in this transient dynamics. Panels e and f show the transient growths as a function of the polar wavenumber for waves with obliquity angle and cross flow angle  $\phi = \pi/4$ . For  $\beta = 1$  all the quantities,  $P_{max}$ ,  $G_{max}$ , and  $\Delta T$ , growth with the wavenumber if  $k > k_{unstable}$  and decrease in otherwise, see panel (e). All the waves shown in (a-e) panels have positive  $\Delta T$ , i.e. the pressure at the wall is in advance with respect to the kinetic energy density. This is not true in general. For example panel f shows that the maximum of  $P$  is not always reached earlier than the maximum of  $G$ . For positive pressure gradient and waves longer than the unstable range the pressure at the wall is in delay with respect to the global energy of the flow. For all the other case ( $\beta < 0$  and  $k > k_{unstable}$  or  $\beta = 1$ ) the maximum of the pressure occurs in advance with respect to the maximum of the energy. Even if is not represented here, we have observed that in general  $P_{max}$  and  $G_{max}$  have the same relation with the cross-flow angle: increase with  $\theta$  for negative  $\beta$  and decrease with  $\theta$  for positive  $\beta$ .

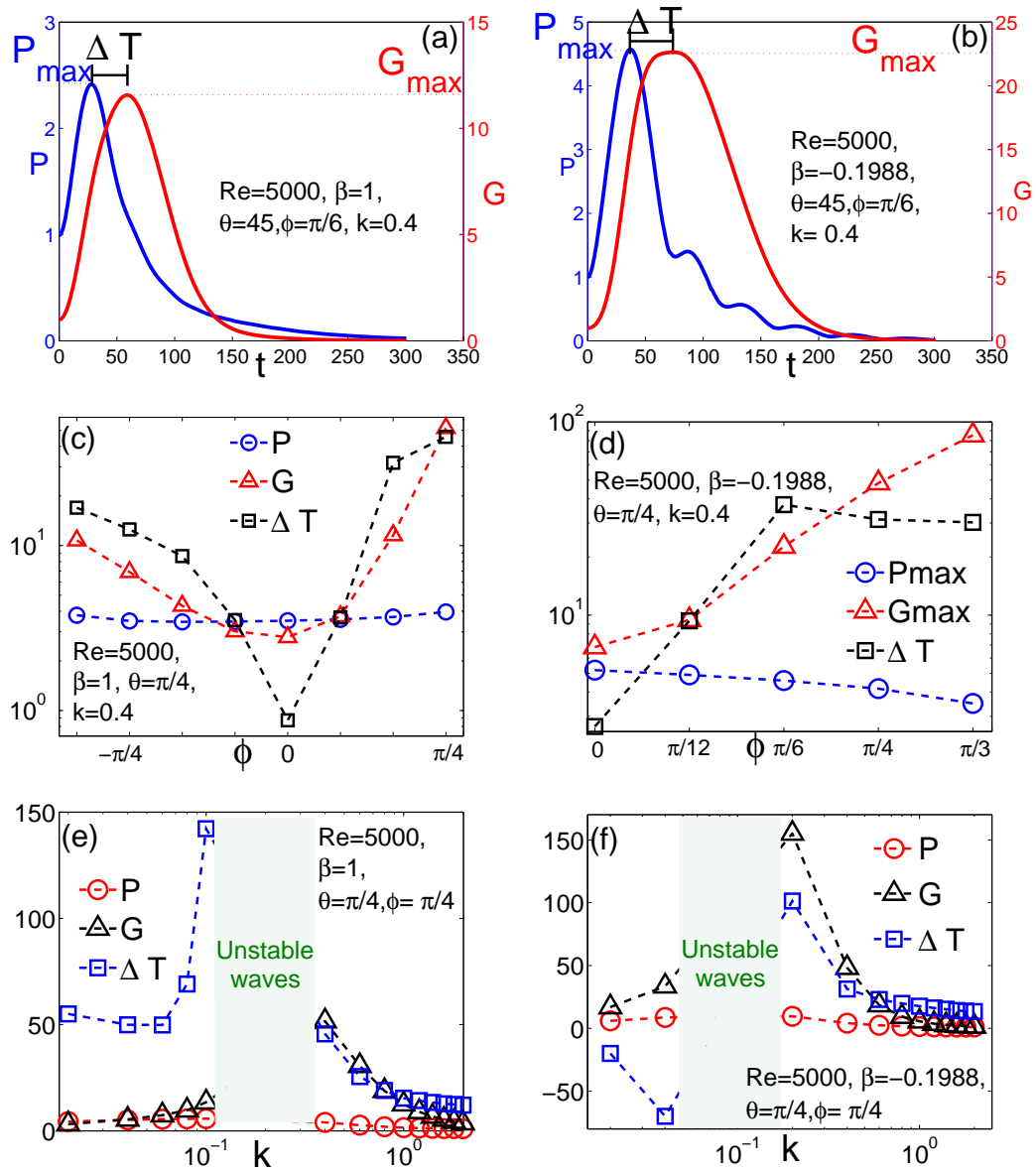


Figure 4.9: Comparison between the amplification factor and the pressure transient,  $Re = 5000$ ,  $\theta = \pi/4$ , Top panels  $\beta = 1$ , bottom panel  $\beta = -0.1988$ . Left panels: examples of transient for  $P$  and  $G$ ,  $k = 0.4$ ,  $\phi = \pi/6$ . Panels c-f: blue circles indicate the maximum value of the pressure amplification, red triangles represent the maximum of the amplification factor, the black squares are the difference between the time in which the perturbation reaches  $P_{max}$  and the time in which it reaches  $G_{max}$ . Panels c-d role of the obliquity angle at fixed obliquity angle  $k = 0.4$ ,  $\phi = 0, \pi/12, \pi/6, \pi/4, \pi/3, 5\pi/12, \pi/2$ . Panel e-f role of the wavenumber at fixed obliquity angle  $\phi = \pi/4$ .



# Conclusions - Part I

In the first part of this thesis we have presented interesting phenomenology relevant to shear flows perturbation waves. The initial value problem associated to arbitrary shear flow perturbations in the form of three-dimensional travelling waves uniform in space is considered. The waves lie in the plane normal to the direction of main variation of the basic flow. We have considered small amplitude perturbation and linearised the perturbed equations that were treated with both the modal theory and as both the initial value problem.

We have first considered the case of two-dimensional base flows. We have mainly considered two archetypical cases: the plane channel (Poiseuille) and the plane wake past a bluff body flows.

Following the traditional approach we began our analysis looking at the dispersion relation of the phase velocity in the far transient of longitudinal waves for two decades of wavenumber, extending the literature results that generally are just for long waves. The agreement with this literature data is really good in particular when these data are obtained in fully non-linear context (laboratory experiments or direct numerical simulations). This validates the use of linear stability analysis to predict the frequency transient and asymptotic behaviour. Moreover we observe that long waves present a dispersive behaviour, while short waves are non-dispersive. Therefore we found the existence of a threshold wavenumber  $k_d$  that separates the waves that asymptotically show a dispersive behaviour, that are the longest ones ( $k < k_d$ ), from the waves with a non-dispersive behavior, the shortest ones ( $k > k_d$ ). The asymptotic velocity profile taken by perturbation with  $k < k_d$  has high derivatives in correspondence to the base flow high shear region. On the other hand, for  $k > k_d$  the asymptotic velocity field have high derivatives in correspondence to the base flow low shear region.

We have then solved the initial value problem and analysed the transient dynamics of this perturbation. Attention is mostly addressed to the phase velocity transient for whom we have tried to extract a general rule that at each given type of initial conditions associates a kind of transient behaviour.

The dispersion relation help us to explain also the transient dynamics. Indeed, given an initial condition, having a wave number higher or lower than  $k_d$  does significantly change the type of transient proved. The possible phase velocity transient can be classified into four categories:

1. really short transient, the phase velocity reaches smoothly its asymptotic values
2. during the transient, the phase velocity jumps to an higher value and the waves are accelerated
3. during the transient, the phase velocity jumps to a lower value and the waves are decelerated
4. more than one jump occurs during the phase velocity transient.

When they occur the jumps are in general accompanied with a modulation of the phase velocity value observed before and after the jump. This modulation show a temporal periodicity that is correlated with the global range of spectral frequencies given by the modal theory.

Of course the type of transient resulting depends on the initial condition imposed. Also the initial conditions can be classified into four types according to their symmetry and in which region of the domain is concentrated its largest variation.

The observation of phase velocity transients leads to identify a three distinct stages in the time evolution of the perturbations. There always is a first part, the early transient, which is heavily dependent on the initial condition, a second much longer part, the intermediate transient, which appears as a kind of intermediate asymptotics and a third part, the asymptotic state that is reached when both the phase velocity and the growth rate take their final constant values. Inside the intermediate transient the perturbation evolves almost exponentially: the phase velocity takes the final constant value, the transverse velocity profiles maintain a near self-similar nature in time and the growth factor changes very slowly. In the wake flow, which is a system slowly evolving in space, our simulations allowed to obtain the temporal scaling for the thickness of perturbation profiles with exponents changing not only in function of the Reynolds number, but also with the wavelength and orientation of the perturbation.

The beginning of the intermediate transient is well marked by the last phase velocity jumps, if there are any. When a jump occurs it separates the intermediate transient from an other time interval in which the perturbation show an almost exponential behavior with a different coefficient.

For each instant belonging to this range, the velocity components profiles of our simulations show the same shape, and this confirmed our hypothesis. In the channel flow case, it is sufficient to normalize the profiles on their peak values in order to make them collapse on a single curve. In the wake flow, which is a system slowly evolving in space and unbounded, the thickness of perturbation profiles increases in time. Therefore to obtain the self-similar curve, the transversal coordinate must be rescaled  $Y = y/t^p$ . The  $p$  exponent depends on the Reynolds number and on the obliquity of the perturbation and tends to 0.5 as  $Re$  goes to 0 or  $\phi$  approaches  $\pi/2$ .

As might be expected, The scaling property of the velocity profile affects the kinetic energy. The energy that the perturbation has during the intermediate term shows a power law scaling

which is very close to the  $-5/3$  turbulent one, if taken at a constant change of rate. We empirically prove that this scaling appears just inside the intermediate transient and is no more observed in asymptotic regime.

These observations are not specific of a peculiar kind of flow (wall bounded or free). This can mean that these scaling properties are not only one of the major signatures of the turbulence interaction, but it also exists hidden inside the dynamics of linear stable waves, where the self-interaction is absent as well. Once known, these properties could induce an important outcome: the modelling and forecast of turbulence fields could be done on the basis of linear solutions. Those solutions are quickly numerically obtained and generally more physically inclusive than other contemporary turbulence models. Therefore, the use of super-computers could become less strategic in the future. Linear solutions in fact do not need parallel computations, and can often be preliminary analytically treated in a way where at least one or two spatial variables can be removed from the differential system of governing equations. Since our observations do not depend on the system control parameter (Reynolds number), on the kind of initial condition and on geometrical parameters, such as the wave inclination, they could also reveal a new set of structural properties of the Navier-Stokes equation solutions. In particular, we think that they can be used to build a bridge between the linear and the non-linear interaction in multi-scale systems.

The perturbation dynamics in three-dimensional shear flow is also considered. We have presented a comprehensive study of the space of the parameters relevant to the life of small perturbations of the three-dimensional boundary layer in cross flow. We considered a group of five parameters: the Reynolds number, the external pressure gradient, the wave number, the angle of cross flow and the tilt of the perturbation with respect to the streamline of the flow outside the boundary layer. We adopted almost optimal initial conditions and classical perturbation methods to obtain information on initial transient and temporal long-term behaviour.

We compared our results with results produced by other numerical simulations concerning the evolution of three-dimensional perturbations. In particular for the long term behaviour we compare our results with Taylor and Peake [133] and Mack [85], while for the initial transient we compare our results with Breuer and Kuraishi [20] and Corbett and Bottaro [27]. In both cases good agreement was found.

Perturbations that have transitional growth but are asymptotically stable could still have a substantial role in triggering non-linear processes that may lead to transition to turbulence. Some of our results are related to this role, in particular with respect to the influence of the wave-angle. We show that in the decelerated three-dimensional boundary layer at a high Reynolds number there are some asymptotically stable perturbations in the range of wave-angles  $[\pi/125\pi/12]$  which are initially able to grow up to six times faster than those which are asymptotically unstable (waves almost aligned with the external flow or orthogonal to it). Among these, some have negative phase speeds, that is they propagate in the negative chord-wise direction, although the associated group velocities are always positive and the energy

propagates in the positive direction. This was observed for Reynolds numbers based on the displacement thickness higher than  $10^3$ , which means Reynolds numbers of the order of  $10^4$  or  $10^7$ , respectively, when calculated on the thickness of the layer or on a chord of the wing profile of about one meter.

There are two other noticeable aspects. The first is that in the decelerated three-dimensional boundary layer the most unstable perturbations are either those nearly aligned with the external current or those almost orthogonal to it, that is almost aligned with the cross flow. Oblique perturbations in between always have strong growths which, however, are still transient, while the perturbations with tilt and direction of propagation opposite to the cross flow are all unstable.

The second aspect is that the perturbed field of pressure at the wall and inside the layer is not synchronous with the amplification factor of the kinetic energy of the disturbances. In general, in the case of boundary layers both accelerated and decelerated, the perturbed pressure field is made in advance up to about 100 times scale. However, in the decelerated case, it is also observed that the very long wave perturbations can induce a significant delay in the oscillation of the pressure which again may be approximately up to 100 time scales of the system.

## **Part II**

# **Stratified turbulent flows**

## Chapter 5

# Stratified flows

When a flow is in turbulent regime it can potentially act on a huge range of scales, from the very small, through the medium scales that influence the human environment to the vast length scales of planets, solar system and galaxies.

Unlike the laminar flows treated in previous part, where viscous forces are dominant and the fluid motion is smooth and constant, turbulent flows are dominated by inertial forces, which tend to produce chaotic eddies, vortices and other flow instabilities.

These turbulent flows exist also in the simplest of everyday occurrences, such as water passing down a plug hole, the movement of air behind a travelling air-plane and in that which perhaps is one of the most important aspects of daily human life, the weather. Turbulence indeed is one of the characteristic properties of atmospheric flows: the majority of processes in the atmosphere, such as transfer of water vapour and atmospheric dust, heat exchange, and the formation of clouds and precipitation, are extremely closely tied to the turbulent nature of motion in the atmosphere. Atmospheric turbulence renders an essential influence on the propagation of sound, light, and radio waves. Finally, atmospheric turbulence influences flight conditions for aircraft. As a consequence the knowledge of the characteristics of turbulence is of great significance for many practical purposes.

Geophysical fluid dynamics has recently become an important branch of fluid dynamics due to our increasing interest in the environment. The importance of the study of atmospheric dynamics can hardly be overemphasized. We live within the atmosphere and are almost helplessly affected by the weather and its rather chaotic behaviour. The motion of the atmosphere is intimately connected with that of the ocean, with which it exchanges fluxes of momentum, heat and moisture, and this makes the dynamics of the ocean as important as that of the atmosphere. The study of ocean currents is also important in its own right because of its relevance to navigation, fisheries, and pollution disposal.

The two features that distinguish geophysical fluid dynamics from other areas of fluid dynamics are the rotation of the earth and the vertical variation of the fluid density/temperature

of the medium.

Rotation is exerted through Coriolis forces which mainly act in horizontal planes whereas stratification largely affects the motion along the vertical direction through the Archimedes force. Depending on the mean density profile, stratification can either enhance or suppress vertical motions. Stratification in the atmosphere is usually stable above the boundary layer [143, 45], i.e. a fluid particle which is displaced in the vertical direction tends to return to its initial position.

At large scales in the atmosphere rotation becomes of secondary importance and the stratification effects dominate. In the last decade there has been important advances in understanding of turbulence in the presence of strong stratification. In the context of homogeneous stratified turbulence, it is known [75, 70] that initially isotropic turbulence in a stratified fluid rapidly becomes anisotropic, with the formation of pancake-like structures in its interior. The formation of the pancakes is sometimes known as layering and its causes are as yet unclear, with a number of mechanisms having been put forward over the years, for example the decorrelation instability of Lilly [74] and the zig-zag instability (see next chapter for major details).

A typical layer formation in turbulent stable stratified flow where a light fluid is on top of a heavier fluid is represented in Figure 5.1. Here it is reported a DNS simulations performed by Chunga and Matheou [25]. The images detail the structure of density fluctuations (lighter colors correspond to denser fluid) in two limiting cases. In the top figure, the stratification is neutral and density behaves like a passive substance exhibiting ramp-and-cliff structures. At the same time, the structures are being sheared, giving rise to forward-leaning structures. As stratification increases, vertical motions are progressively inhibited and eventually turbulence collapses, forming thin layers as shown in the bottom image.

The chapter is organized as follows. In section 5.1 we derive the motion equation under the Boussinesq approximation; while in section 5.2 typical parameters of stratified flows are discussed.

## 5.1 The Boussinesq approximation

The density may, in general, either increase or decrease with height. The processes that can lead to changes in air density in the atmosphere are in principle three: the variation of atmospheric pressure with height, the pressure changes that occur dynamically because of atmospheric motions, the phenomena of thermal expansion. Consider separately the three effects. The first effect and phenomena associated with stratification and correspond to the budget in the Navier-Stokes equations between the vertical components external forces and pressure

$$\nabla P = f^{ext}$$

leading to the equation of hydrostatic balance. The second and third effect corresponds to density fluctuations generated in a dynamics due to motions of fluid and temperature variations. Imagine an area of medium size  $L$  whose speed and its variation are both  $U$ . This means that the corresponding time scale is  $L/U$ . In the absence of external forces and viscous terms in Navier-Stokes will therefore be of the order of magnitude, in sequence:

$$\frac{U}{\tau} \approx \frac{U^2}{L} \approx \frac{\Delta P}{\rho L}$$

where  $\Delta P$  is the change in pressure corresponding. From the equation of state we have

$$P = \rho \frac{T}{m} \approx \rho v_{th}^2 \quad \Rightarrow \quad \frac{\Delta P}{\rho} \approx v_{th}^2 \frac{\Delta \rho}{\rho} + \frac{\Delta T}{m}$$

therefore the relative density variation should satisfy

$$\frac{\Delta \rho}{\rho} < \max \left( \frac{u^2}{v_{th}^2}, \frac{\Delta T}{T} \right)$$

Recall that in less than a factor  $O(1)$ ,  $v_{th}$  is the speed of sound  $c$  for an ideal gas. We thus see that if the Mach number  $M = u/c$  and the relative variation of the temperature scale  $\Delta T/T$  are both small, the density variations produced are themselves small, i.e., the fluid motion is in a first approximation incompressible. In the troposphere, the first condition is always verified and it is the only effect that produces changes in density stratification. Therefore, tropospheric motions, with a vertical scale length much smaller than the troposphere height, is almost incompressible.

In the stratosphere, things are more complicated, since changes in temperature are associated with density variations, and even if the motions occur at scales much smaller than the stratosphere height, and are in good approximation incompressible, small density variations produced are still responsible for the same motion through convection. These effects can be taken into account as perturbations, through the so-called **Boussinesq approximation**. The Boussinesq idea consist in take into account the density fluctuation just in the term in which it is absolutely necessary, while consider it as a constant for all the others. To understand what this means we have to do an accurate magnitude analysis. Let hypnotizes that the relative density variation are small  $\Delta \rho'/\rho_0 \ll 1$ . We can first consider the continuity equation:

$$\frac{1}{\rho} \frac{D\rho}{Dt} + \nabla \cdot \vec{u} = 0 \quad (5.1)$$

It is always possible see the density as a constant plus a time dependent correction term  $\rho(x, y, z, t) = \rho_0 + \rho'(x, y, z, t)$  where the fluctuation  $\rho'$  is related to the temperature effect. Now,



since  $\rho_0$  is a constant, we have  $D\rho/Dt = D\rho'/Dt$ . Furthermore, in the absence of other information, we assume that the typical values given by the derivatives of  $u$  are approximately equal. It is also reasonable to assume that the velocity of the fluid remains limited: a particle of fluid that moves with a speed arbitrarily large has unlimited kinetic energy, and this seems physically unreasonable. If we indicate with  $U$  the typical amplitude of the velocity fluctuations and we call  $L$  the typical distance between its maximum and its minimum value, it is reasonable that the typical value of the derivative space of  $(\bar{u})$  should be close to the ratio between these two quantities, then

$$\left| \frac{\partial u}{\partial x} \right| \approx \left| \frac{\partial v}{\partial y} \right| \approx \left| \frac{\partial w}{\partial z} \right| \approx \frac{U}{L} \quad (5.2)$$

Recall that our aim is to estimate the magnitude of  $D\rho'/Dt$  in a way that is comparable to the magnitude of spatial derivatives of  $\bar{u}$ . The convective derivative of the density represents the variation in time of a particle of fluid followed along its path. The density fluctuations oscillate between its maximum and its minimum at a characteristic time which we call  $\Delta t$  and has to be of the order of

$$\Delta t \approx \frac{L}{U}.$$

As a consequence the density variation is

$$\left| \frac{D\rho'}{Dt} \right| \approx \frac{\Delta\rho'}{\Delta t} \approx \frac{\Delta\rho'U}{L}$$

that implies

$$\frac{\left| \frac{1}{\rho_0} \frac{D\rho'}{Dt} \right|}{\left| \frac{\partial u}{\partial x} \right|} \approx \frac{\Delta\rho'}{\rho_0} \ll 1.$$

This means that the term containing the density in the continuity equation is small compared to the terms containing the velocity as much as it is  $\rho'$  with respect to the reference density  $\rho_0$ . In other words, in the continuity equation the density is dominated by the velocity divergence and thus we can use the continuity equation for incompressible fluids:

$$\nabla \cdot \bar{u} = 0.$$

Let us now consider the momentum equation. Let us suppose that there is no motion and that the density is constant. In this case the pressure gradient is given by the hydrostatic equation

$$\frac{\partial p_0}{\partial z} = -\rho_0 g$$

In the general case the pressure field can be expressed as the sum of hydrostatic pressure  $p_0$  and a dynamic pressure  $p'$

$$p(x, y, z, t) = p_0(z) + p'(x, y, z, t)$$

By replacing the pressure in the Navier Stokes equation we obtain:

$$(\rho_0 + \rho') \left( \frac{\partial \bar{u}}{\partial t} + \bar{u} \cdot \nabla \bar{u} \right) = -\nabla p' - \left( \frac{\partial p_0}{\partial z} + \rho g \right) - \rho' g \hat{k} + \nu \Delta \bar{u} \quad (5.3)$$

The hydrostatic terms cancel each other, then the density remains only in two terms. We have adopted the assumption  $\rho' \ll \rho_0$ , therefore on the left side  $\rho'$  can be neglected. On the right side the density fluctuation multiplies the gravitational acceleration and can not be neglected. Therefore the Navier - Stokes equations under the Boussinesq approximation are expressed as follow

$$\nabla \cdot \bar{u} = 0 \quad (5.4)$$

$$\rho_0 \left( \frac{\partial \bar{u}}{\partial t} + \bar{u} \cdot \nabla \bar{u} \right) = -\nabla p' - \rho' g \hat{k} + \nu \Delta \bar{u} \quad (5.5)$$

at this point we need another equation in order to close the system obtained. We can consider the internal energy equation expressed in term of temperature:

$$\frac{DT}{dt} = \kappa \Delta T \quad (5.6)$$

where  $\kappa$  is the thermal diffusivity. Since we have assumed small density variation, we can linearise the state equation that relate density and temperature:

$$\rho = \rho_0 [1 - \alpha(T - T_0)] \quad (5.7)$$

and we can express the energy equation in terms of fluctuation density.

Eventually we can further decompose  $\rho'$  as the sum of a linear function of  $z$  and a proper fluctuating component and indicate with  $G$  the linear density gradient:

$$\rho' = \tilde{\rho}(x, y, z, t) + G(z)$$

In conclusion the equation of motion under the Boussinesq approximation are

$$\left\{ \begin{array}{l} \nabla \cdot \bar{u} = 0 \\ \frac{D\bar{u}}{Dt} = -\nabla p' + \frac{1}{Re} \nabla^2 \bar{u} + \frac{g}{\rho_0} \tilde{\rho} \\ \frac{D\tilde{\rho}}{Dt} = \kappa \nabla^2 \tilde{\rho} - Gu_3 \end{array} \right. \quad \begin{array}{l} (5.8) \\ (5.9) \\ (5.10) \end{array}$$

## 5.2 Density vertical variation and fluid motion

We want now to understand under which conditions the buoyancy forces produce motion of a fluid. For this purpose we assume that the flow is in absence of motion ( $\bar{u} = 0$ ) and that we can apply the Boussinesq approximation. In this way, the equations are reduced only to the hydrostatic relation:

$$\frac{\partial p}{\partial z} = -\rho g \quad (5.11)$$

Moreover suppose that  $\rho$  depends only on  $z$ . To determine if the vertical profile of density specified by  $\rho(z)$  is stable or unstable, let's suppose to move a fluid particle from its initial height  $z$  at  $z+h$ . The equation which give us the vertical velocity of the particle is

$$\frac{Dw}{Dt} = -\frac{1}{\rho_0} \nabla p - \frac{\rho(z)}{\rho_0} g \quad (5.12)$$

For the moment we neglect the viscosity term, but just for simplifying the calculation. If we suppose to know  $\rho(z)$ , this equation contains two unknowns:  $w$  and  $p$ . In general, therefore, is not resolvable, but in our situation we can find an approximate solution. In fact, if the vertical velocity is initially zero the pressure is specified by the hydrostatic equation. Also until  $w$  is small, we can use Eq. 5.11 to remove the pressure from Eq. 5.12 without entailing an appreciable error. In this way we yield:

$$\frac{Dw}{Dt} = \frac{g}{\rho_0} [\rho(z+h)\rho(z)] \quad (5.13)$$

It is important to note that the pressure term tends to  $\rho(h+z)$ , because that is the hydrostatic pressure at the height at which the particle was increased, while the gravity term keeps  $\rho(z)$  because we assume that during its motion the particles maintains its density. Now,  $Dw/Dt$  is the Lagrangian acceleration of the particle, so we have

$$\frac{Dw}{Dt} = \frac{d^2 h}{dt^2} \quad (5.14)$$

Also note that  $|\rho(z+h)\rho(z)| \approx d\rho/dzh$ . Then we can rewrite our equation as follows

$$\frac{d^2h}{dt^2} - \frac{gd\rho}{\rho_0 dz}h = 0 \quad (5.15)$$

It is usual to define the quantity

$$N^2 = -\frac{g}{\rho_0} \frac{d\rho}{dz} \quad (5.16)$$

it is positive if the density decreases upward and negative otherwise. Until the displacement  $h$  of the particle is small it is easy to solve this equation, because in this case it is reasonable to consider  $d\rho/dz$  as a constant. Some particular solution are almost obvious. It is easy to verify that if  $N^2$  is positive, then both  $h(t) = \cos(Nt)$  and  $h(t) = \sin(Nt)$  satisfy the equation 5.15. These are periodic solutions, then the fluid particle, deviated from its initial position, not goes away from it, but it fluctuates around it. If, instead,  $N^2$  is negative, we define  $\mathbb{N} = -\sqrt{N^2}$ ; a pair of particular solutions is given by  $h(t) = \exp(\mathbb{N}t)$  and  $h(t) = \exp(-\mathbb{N}t)$ . The first tells us that the displacement of the fluid particle increases indefinitely in time, and it no return to its initial position. In this way we have obtained a stability criterion for stratified flows:

- Statistically stable fluid,  $N^2 > 0$  density decrease upward. A fluid particle oscillates if it deviated from its equilibrium position.
- Statistically unstable fluid,  $N^2 < 0$  density increase upward. A fluid particle moves away indefinitely from its initial position as soon as any perturbation deviate from it.

If the fluid is statically stable, the quantity  $N$  is the frequency of oscillations performed by the fluid particle around its position. It is known as frequency of Brunt- Väisälä .

### 5.2.1 The Froude number

We consider the case of a three-dimensional flow outside boundary layers at high Reynolds and Peclet numbers, so that both viscous and diffusive processes are negligible. Thus we write the momentum and density equations (for steady flow)

$$\rho \bar{u} \cdot \nabla \bar{u} = -\nabla p + \rho g \nabla \cdot \bar{u} = 0 \quad (5.17)$$

We take  $z$  vertically upwards and suppose that the basic stratification consists of a uniform density gradient ( $-d\rho/dz$ ). Because  $\rho_0$ , does not vary horizontally, the balance between  $\rho_0 g$  and the hydrostatic pressure can be subtracted out from equation 5.17 just as it can subtracted out for an entirely uniform density case. We now consider, superimposed on this basic configuration, a flow with length and velocity scales  $L$  and  $U$ , produced, for example, by moving an obstacle of size  $L$  horizontally through the fluid at speed  $U$ . This will produce a modification

of the density field which we denote by  $\rho_0$ , related to the stratification in the form

$$\bar{u} \cdot \nabla \rho' + w \frac{d\rho_0}{dz} = 0 \quad (5.18)$$

that in order of magnitude give us

$$\rho' \approx \frac{WL}{U} \left| \frac{d\rho_0}{dz} \right| \quad (5.19)$$

where  $W$  is now restricted by the fact that the flow cannot produce buoyancy forces associated with  $\rho'$  that are larger than the other forces involved. Since the buoyancy force does not contribute directly to the horizontal components of Eq. 5.17 it is convenient to work in terms of the vorticity form of this equation

$$\rho(\bar{u} \cdot \nabla \omega - \omega \cdot \nabla \bar{u}) = -g \left( \hat{i} \frac{\partial \rho'}{\partial y} - \hat{j} \frac{\partial \rho'}{\partial x} \right) \quad (5.20)$$

Since the order of magnitude of  $\omega$  is  $U/L$  this indicates that the order of magnitude of  $\rho'$  must remain not greater than

$$\rho' \approx \frac{\rho_0 U^2}{gL} \quad (5.21)$$

By comparing i with Eq 5.19 we get

$$\frac{W}{U} \approx \frac{\rho_0 U^2}{gL^2} \left| \frac{d\rho_0}{dz} \right| = Fr^2 \quad (5.22)$$

When  $Fr^2$  is small the horizontal motion has only much weaker vertical motion associated with it.  $Fr$  is called **Froude number**,  $1/Fr^2$  is sometimes known as the Richardson number. Similar analysis can be given for flows in which viscous and/or diffusive effects are strong. This is a matter of some complexity, since different detailed treatments are appropriate for low, intermediate and high Prandtl number. Thus we omit consideration on it; when we talk here after of low Froude number flows, it is assumed that any other criterion for the flow to be strongly constrained by stratification is also fulfilled. In general we can have three situations:

- $Fr \rightarrow \infty$  non stratified flow,
- $Fr \rightarrow 0$ , strong stratification,
- $Fr \approx 1$ , intermediate case

In conclusion the dimensionless Navier Stokes equation with the Boussinesq approximation are:

$$\begin{cases} \nabla \cdot \bar{u} = 0 \\ \frac{D\bar{u}}{Dt} = -\nabla p' + \frac{1}{Re}\nabla^2\bar{u} + \frac{1}{Fr^2}\tilde{\rho} \\ \frac{D\tilde{\rho}}{Dt} = \kappa\nabla^2\tilde{\rho} - Gu_3 \end{cases} \quad (5.23)$$

The next chapters treat two cases of stratified flows. In the first case the stratification is homogeneous and we focus on the aspects related to the energy spectrum. In the second case the typical lapse rate of the atmospheric stratification is perturbed and we examine how this changes the dynamics of a turbulent mixing.

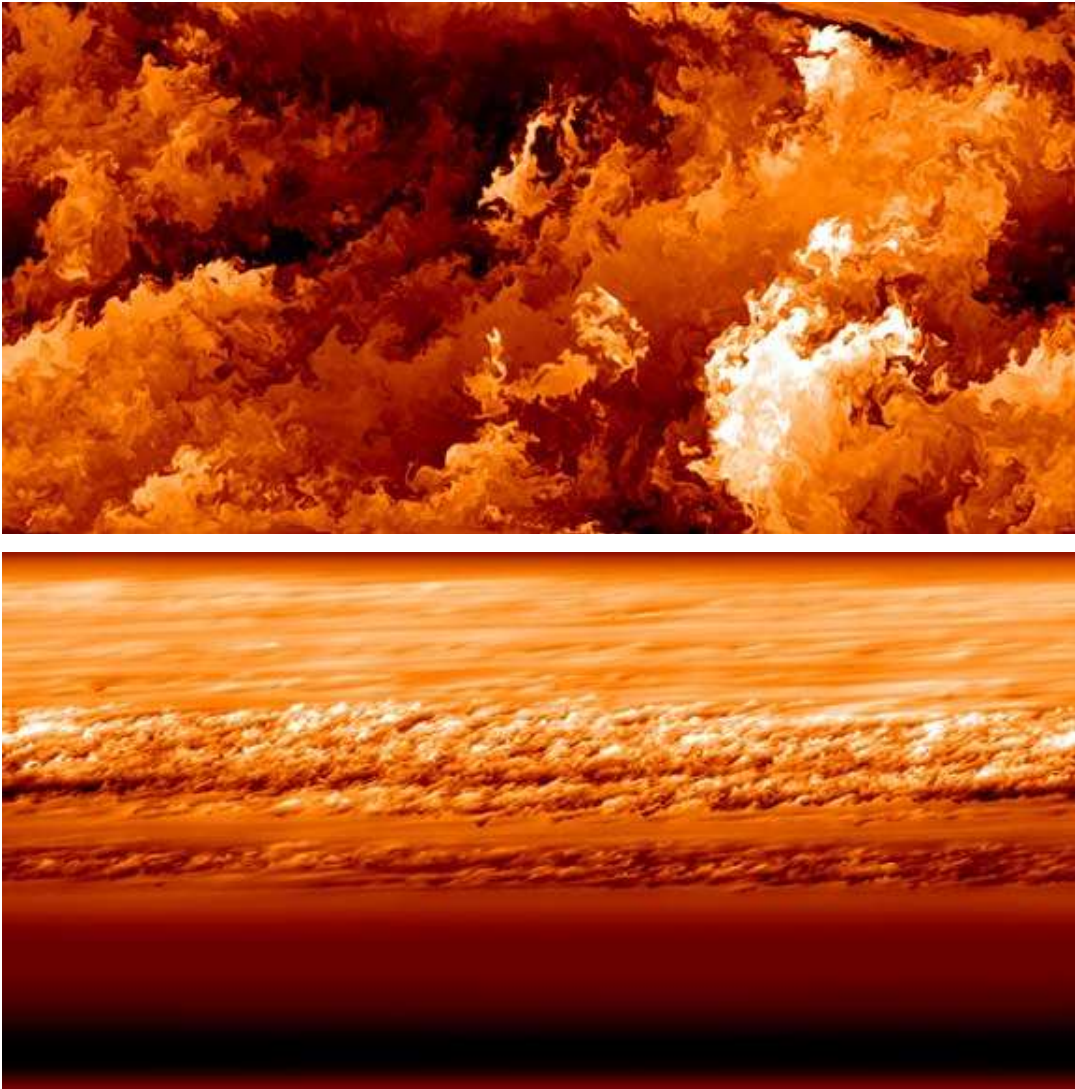


Figure 5.1: Direct numerical simulation of stratified turbulence. Lighter colors correspond to denser fluid. Results by [25]

## Chapter 6

# Transition to turbulence from counter-rotating vortex pair in a stratified fluid

Vortices are ubiquitous in the atmosphere and oceans. The question of their stability has important practical and theoretical consequences, since instability provides a mechanism for energy transfer from large to small scales where dissipation occurs.

As regard to the energy transfer, the wavenumber spectra of kinetic and potential energy measured in the upper troposphere and lower stratosphere have been debated for several decades. These spectra, as the spectrum of three-dimensional isotropic turbulence, exhibit at the horizontal mesoscale (wavelengths  $\approx 1500 \text{ km}$ ) a  $k_h^{-5/3}$  dependence, where  $k_h$  indicates the wavenumber in the horizontal plane (see Figure 6.1). This scaling law leads to the hypothesis of a direct energy cascade.

The question then was how to argue this horizontal cascade. Erik Lindborg [76] develops a similarity hypothesis for such a cascade based on the ratio between the horizontal and the vertical length scale. He concludes that the forward cascade process is generated by the formation of layers which is universal in strongly stratified fluids as discussed in Chapter 5 and illustrated in Figure 5.1. However the detailed physics of why the layers formation would lead to a  $-5/3$  cascade has been unclear.

The layer formation leads to Kelvin Helmholtz instability and one could argue, that the local KH breakdowns would occur intermittently in the horizontal, leading to the horizontal cascade. However it seems that the Kelvin Helmholtz instability affect the spectra only in the range of the wavenumbers larger than the buoyancy wavenumber ( $k_b = 2\pi N/U$ ), where the motion is near-isotropic [117]. We are interested in whether it can be tied to other physics like, as the Lundgren model [83]. He argues that the development of  $-5/3$  spectrum appears to be linked to the generation of stretched spiral vortices, which in turn grow out of locally orthogonal vortices



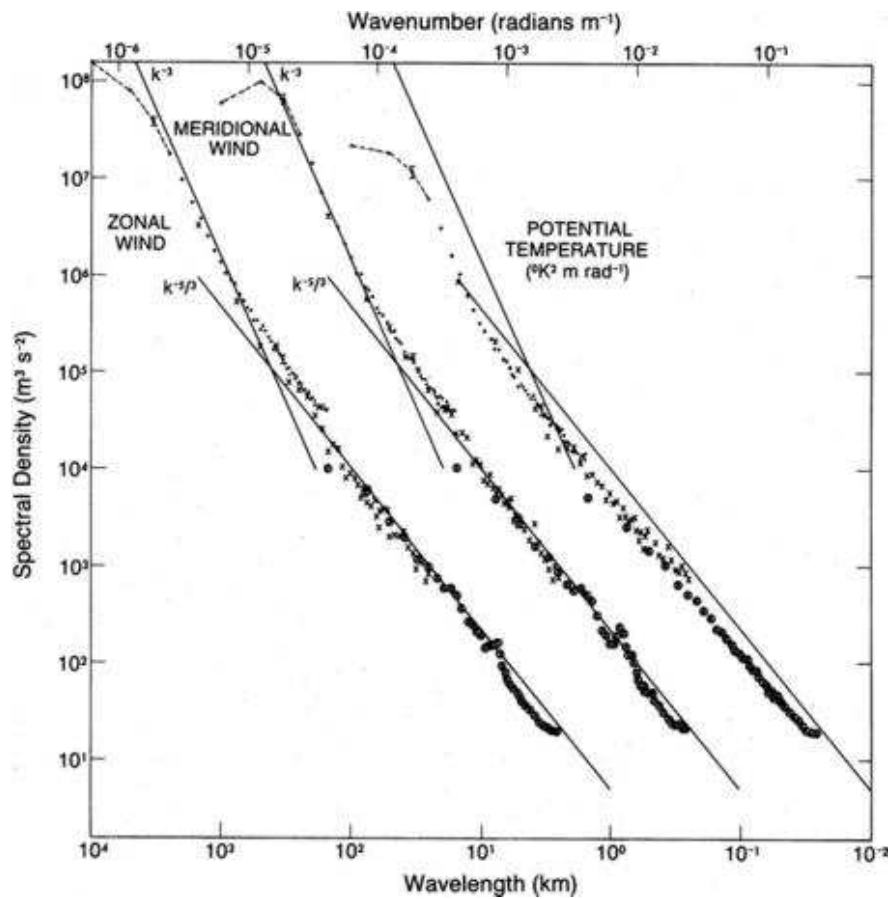


Figure 6.1: Atmospheric spectra of kinetic energy of the zonal and meridional wind components and potential energy measured by means of the potential temperature. The spectra of meridional wind and potential temperature are shifted one and two decades to the right, respectively. Reproduced from Nastrom & Gage [102].

created by a series of vortex reconnection events, a configuration that has been seen in some isotropic calculations just before they become fully turbulent [66].

For this purpose we are analysing the vortex dynamics in stratified flow considering a simple configuration that shows a transition to turbulence. This configuration consist in two column vortex parallel to the gravitational direction and it has been recently fully investigated since it can lead to the zig-zag instability. This instability entail a transfer of energy from large scales to small vertical dissipative scales. Moreover at high Reynolds number, the zig-zag instability creates a so intense vertical shear that small-scale Kelvin-Helmholtz instability develop and leads to a turbulent regime.

The state of the art and the rational for this kind of analysis is discussed in the following section. Section 6.2 describe the mathematical formulation; while major details about the zig-zag instability are treated in section 6.3. In section 6.4 we show and discuss our results. Cocluding remark are in section 6.5.

## 6.1 Rationale and state of the art

Fluid motions in the atmosphere and oceans are often strongly affected by stable density stratification. In these flows, large vertical motions are inhibited by the buoyancy force, leaving only two possible modes of motion: internal gravity waves and vortices with vertical axis [116]. Laboratory experiments [75, 24], numerical simulations [116, 70] and oceanic measurements [46] have revealed that these vortices never have a large vertical extent, but are rather thin like **pancakes**. It is now well known that this layered flow structure enhances energy dissipation through the associated strong vertical velocity shear [56]. This feature has been invoked as the reason why stratified turbulence departs profoundly from twodimensional turbulence although the motion is mostly horizontal. However, despite its importance in understanding turbulence in geophysical flows, the reason why the vortices acquire such a flat ‘pancake’ shape was unclear: *is such layering due to the initial collapse of three-dimensional motions under the gravitational restoring force or is it an intrinsic behaviour of vertical vortices in the presence of stable stratification?*

Some results of the numerical simulations of two-dimensionally forced stratified turbulence by Herring & Métais [56, 92] suggest that **the layering may arise as a result of an instability**. The initial conditions of these numerical experiments consisted of a forced turbulent flow vertically uniform, i.e. purely two-dimensional, upon which a three-dimensional perturbation was added. This disturbance grow exponentially and resulted in the formation of decoupled layers. However, the physical mechanism of this instability remains unexplained. Subsequently, Fincham et al. [39], did an experiment on a vertical cylinder wakes and showed that layers can emerge from a vertically coherent flow.

In an attempt to further elucidate the mechanism by which decoupled layers arise, Billant & Chomaz [13] investigate the dynamics of a simple prototype flow initially uniform along the

vertical: a pair of long counter-rotating vertical columnar vortices in a strongly stratified fluid. Such a vortex pair has been studied in detail in non-stratified fluids because of its aeronautical interest. Early work on vortex instability was thus concerned with neutrally stratified fluids. Lord Kelvin [63] studied disturbances to columnar Rankine vortices (Kelvin waves), and found them to be neutrally stable. Interest in the instability of such disturbances was revived by Crow [31], who found that a pair of counter-rotating vortices is unstable to axially varying displacements of the vortex cores (bending waves). Unstable bending waves grow via resonance with the oscillating strain field induced by each vortex on the other. The corresponding growth rate is maximum at axial scales much larger than the vortex radii. Instabilities also exist at smaller axial scales, driven by resonances with Kelvin waves of more complicated radial structure than the bending waves. These instabilities have been studied extensively in the context of a vortex filament in an externally imposed strain field. A separate approach has focused on the instability of two-dimensional flows with elliptical streamlines to three-dimensional perturbations [146]. Both sets of short-wave instabilities are referred to as elliptic instabilities [69]. Laboratory experiments by Thomas & Auerbach [135] demonstrated that a counter-rotating vortex pair undergoes an antisymmetric short-wave instability. They suggested that the instability is driven by the resonance mechanism of the elliptic instability, and called it a cooperative elliptic instability. Linear simulations and analysis [12] and direct numerical simulations [72] support this view.

Density stratification modifies the elliptic instability by changing the dispersion relation of the Kelvin waves. Miyazaki & Fukumoto [41] showed that the elliptic instability of a strained uniform vortex aligned with a stable density gradient is inhibited by stratification and disappears when the buoyancy frequency exceeds the vorticity. However, they found that other instabilities connected with higher-order resonances emerge and persist at strong stratifications. For the case of a vortex pair, Billant & Chomaz [13] showed that the cooperative elliptic instability is suppressed for strong enough stratification. At these strong stratifications they found a distinct antisymmetric instability, which they call the **zig-zag instability**. Similar to the Crow instability, the zig-zag instability bends and twists the vortex cores horizontally with little change to their internal structure. It has been studied with laboratory experiments, multiple-scale analysis, and linear and non linear numerical simulations [13, 14, 15, 34]. The zig-zag instability directly transfers the energy from large scales to the small dissipative vertical scales. Moreover, for high Reynolds number, the vertical shear created by the zig-zag instability is so intense that small-scale Kelvin-Helmholtz instabilities develop leading to a turbulent regime.

## 6.2 Methods

We consider the evolution of two counter rotating vortex columns in a highly stratified fluid (see a scheme of the initial condition in Figure 6.2).

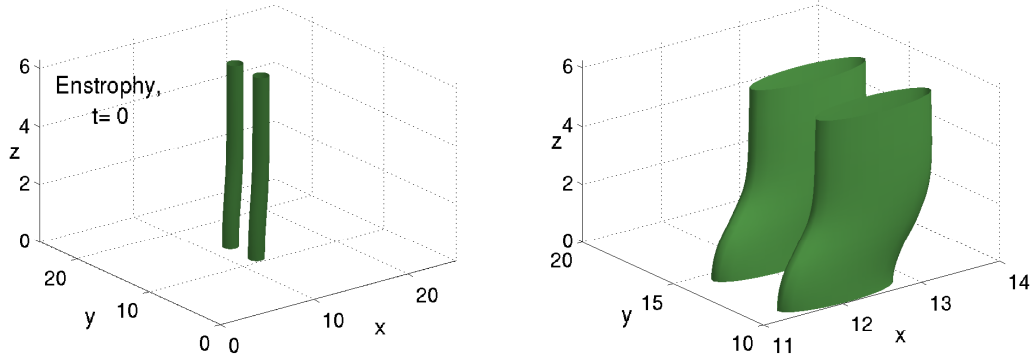


Figure 6.2: Scheme of the initial condition. Left panel: isosurface of the vorticity in the entire domain. Right panel: zoom on columns vortex the perturbation.

The governing equations are the incompressible Navier-Stokes equations under the Boussinesq approximation discussed in the previous chapter Eq. 5.23. We have already defined three non-dimensional parameters: the Reynolds number, the Froude number and the Richardson number, that are respectively

$$Re = \frac{Ur}{\nu}, \quad Fr = \frac{U}{Nr}, \quad Ri = \frac{N^2}{\left(\frac{\partial u}{\partial z}\right)^2 + \left(\frac{\partial v}{\partial z}\right)^2} \quad (6.1)$$

where  $U$  is the initial propagating speed of the vortex columns,  $r$  is the initial radius of the columns,  $G$  is the vertical gradient of the density linear component,  $\nu$  the viscosity. In the test run case that we treat in section 6.4 we have imposed

$$U = 6.54, \quad \nu = 0.008, \quad r = 1, \quad \frac{g}{\rho_0} = 2.41, \quad -\frac{d\bar{\rho}}{dz} = 2.41$$

and thus

$$Re = 817, \quad Fr = 2.712.$$

The equations are solved by a pseudo-spectral DNS code implemented by Prof R. Kerr (University of Warwick) [66], with whom we have collaborated for this study. As computation domain box has  $256 \times 256 \times 128$  grid points.

In respect to the results in the literature we add the an analysis based on the enstrophy production. The enstrophy,  $Z$ , is defined as half the integral of the vorticity square and its rate

of change is given by

$$\frac{1}{2} \frac{\partial Z}{\partial t} + \frac{1}{2} (\mathbf{u} \cdot \nabla) Z = \underbrace{\frac{\omega S \omega}{Z^{3/2}}}_{\text{vortex stretching}} + \underbrace{\frac{g}{\rho_0} \hat{\mathbf{z}} \cdot (\boldsymbol{\omega} \times \nabla \rho')}_{\text{baroclinic production}} + \underbrace{\nu (\boldsymbol{\omega} \cdot \Delta \boldsymbol{\omega})}_{\text{viscous effect}}$$

where  $\boldsymbol{\omega}$  is the vorticity ( $\boldsymbol{\omega} = \nabla \times \mathbf{u}$ ), and  $S_{ij}$  is the rate of strain tensor given by

$$[S]_{ij} = \frac{1}{2} \left( \frac{\partial u_i}{\partial x_j} + \frac{\partial u_j}{\partial x_i} \right)$$

We normalize the vortex stretching and the baroclinic production terms over  $Z^{3/2}$ , in order to quantify the significance of where the spirals occur:

$$S = \frac{\omega S \omega}{Z^{3/2}}, \quad B = \frac{\frac{g}{\rho_0} \hat{\mathbf{z}} \cdot (\boldsymbol{\omega} \times \nabla \rho')}{Z^{3/2}} \quad (6.2)$$

It is known from experiments and simulations that in fully developed isotropic turbulence is  $S \approx 0.5$  [142]. In this context find  $S \approx 0.1$  would mean that the stretching is significant.

### 6.3 The Zig-Zag instability

As mentioned in Section 6.1 the presence of stratification radically modifies the evolution of vertical column vortices. When buoyancy effects are dominant, the Crow and elliptic instabilities are inhibited and we show in the present section that a third type of instability spontaneously slices the columnar vortex pair into thin horizontal layers of pancake-like dipoles. This instability, which has been named **zig-zag instability** by Billant & Chomaz [13], occurs only when the fluid is strongly stratified and clearly differs from the Crow and elliptic three-dimensional instabilities. This section is devoted to a characterization of this instability and its further transition to a turbulent regime.

The linear analysis [14] employs an asymptotic expansion in small  $Fr$  and  $Fr_z = Uk_z/N$ , where  $k_z$  is the vertical wavenumber of the perturbation to the vortex pair. It is therefore restricted to vertical scales much larger than  $2\pi U/N$ . In this strongly stratified regime, the dimensionless equations for vortex motion describe decoupled layers of two-dimensional solenoidal flow at lowest order in  $Fr$  and  $Fr_z$ . Buoyancy and vertical velocity are slaved to the horizontal velocity via hydrostatic balance, and gravity waves are filtered out. Billant & Chomaz moreover showed that the slaved vertical velocity induced by a bending and twisting perturbation of the dipole stretches the vorticity in a way that amplifies the perturbation. This is the basic mechanism of the zig-zag instability.

In the laboratory a 60 cm long columnar vertical vortex pair generated with a flap apparatus has been investigated by Billan & Chomaz [13]. The basic vortex pair closely resembles the

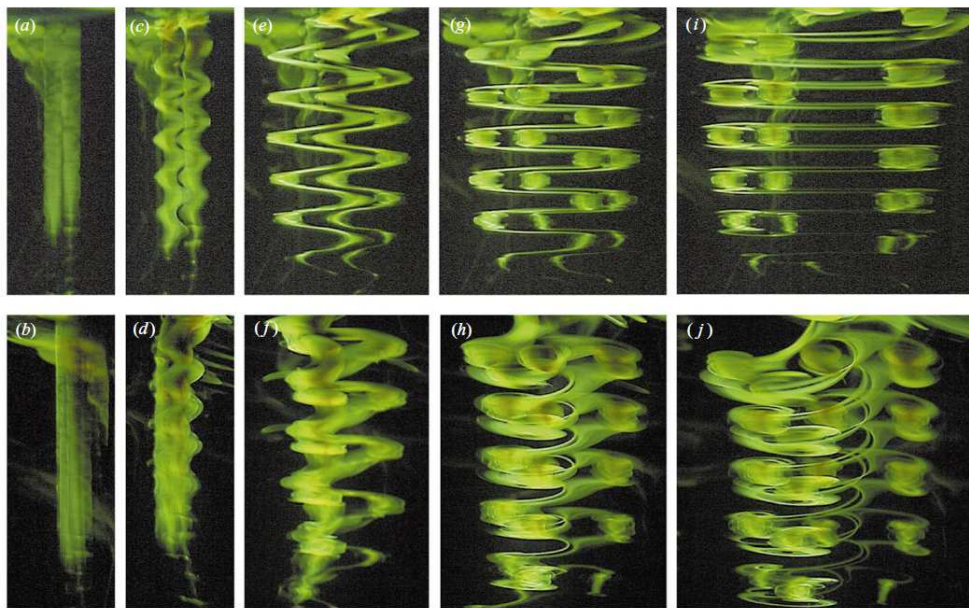


Figure 6.3: A sequence of frontal (*a*), (*c*), (*e*), (*g*), (*i*) and side (*b*), (*d*), (*d*), (*h*), (*j*) views showing the growth of the zig-zag instability for  $Fr = 0.19$  and  $Re = 365$ . The pictures have been taken at 7 s (*a*), (*b*); 36 s (*c*), (*d*); 75 s (*e*); 109 s (*d*); 121 s (*g*), (*h*); 176 s (*i*), (*j*) after stopping the flap motion. In the side views, the vortex pair is initially propagating leftward. In this particular experiment, a slight forcing at the natural wavelength has been applied to make the zig-zag pattern perfectly periodic. Picture by [13]

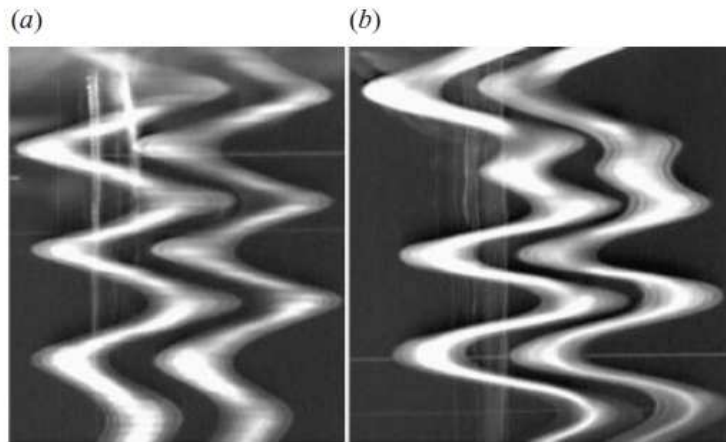


Figure 6.4: Visualizations of the zig-zag instability in two different experiments in the absence of forcing for the same parameters  $Fr_0 = 0.19$ ,  $Re = 365$  at  $t = 121s$  after stopping the flap motion. In (a) a regular zig-zag pattern is observed while a defect can be seen in (b). Picture by [13]

Lamb-Chaplygin dipole that they adopt for the numerical analysis. In Figure 6.3 and Figure 6.4 we report some of their experimental results.

Shortly after the end of the flap motion, at  $t = 7s$  the columnar vortex pair is initially straight and uniform along the vertical, see Figure 6.3 (a,b). At  $t = 36s$ , it exhibits sinusoidal antisymmetric deformations which are best seen in the frontal view (Figure 6.3(c)). Obviously, this antisymmetric instability differs from the Crow instability which is symmetric and ultimately produces vortex rings. Although it has the same symmetry as the elliptic instability, some differences are readily noticeable. The whole vortex pair is bent without noticeable internal deformations. This contrasts with the elliptic instability for which the mean axes of the two vortices remain globally straight, but the two vortex cores and envelopes are bent out of phase. At  $t = 75s$ , in the frontal view, panel (e), the amplitude of the deformations has increased dramatically. Nonetheless, the instability grows gently without any gravitational collapse and without subsequent large three-dimensional motions as it would for the elliptic instability. This distinct behaviour, i.e. the occurrence or not of the collapse phenomenon, has allowed the Billan & Chomaz to unambiguously define a critical Froude number demarcating the elliptic and zig-zag instabilities. In Figure 6.4 the "zig-zag pattern" reached by the perturbed column vortex is shown for two different simulation with the same parameters.

This experiment was then followed by a series of linear stability papers and a few direct numerical simulations using the three-dimensional, incompressible Boussinesq-Navier-Stokes equations. For the initial perturbations chosen, the primary instability did not yield the zig-zags. Recently, it is shown that the primary stratification terms completely oppose the stretching terms [16]. Only with the inclusion of higher-order terms could zig-zags form, and numeri-

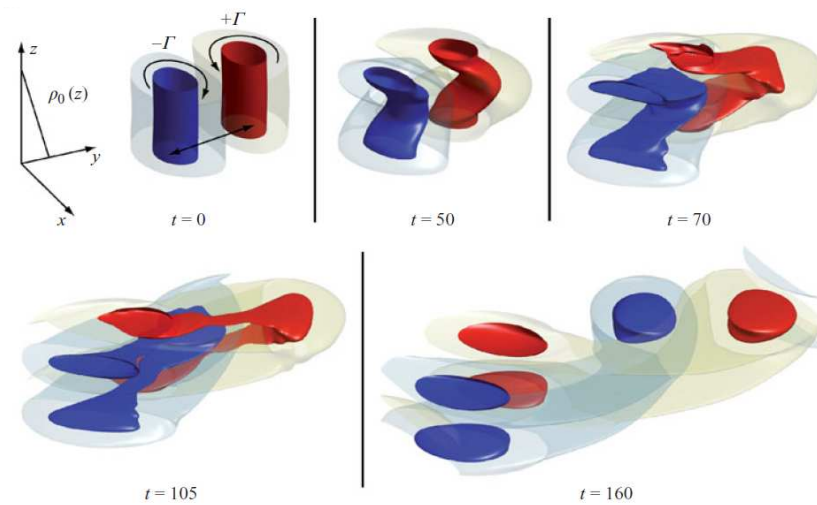


Figure 6.5: Vertical vorticity isosurfaces of simulation with  $Fr = 0.66$  and  $Re = 1060$ . Red and blue contours represent respectively plus and minus 60% of the vertical average of the maximum vertical vorticity in each horizontal plane. Transparent isosurfaces are the same for a 10% level. Picture from [34]

cally, zig-zags are retarded. The most successful numerical experiment [34] did yield zig-zags, but only after the order of 50-70 characteristic timescales. What we found perplexing is how difficult it was for the instabilities to form zig-zags, but not difficult for the experiments. In the next section a different initial condition that speed up the zig-zag instability is proposed.



## 6.4 Vertically shifted perturbation and second instability

By vertically shifting the perturbations on two counter-rotating vortices, it is shown that the zig-zag patterns seen experimentally develops on a much faster timescale than if the perturbations are on the same horizontal plane [67]. In Figure 6.6 indeed it is shown that the zig-zag pattern can show up after only 7 time scale, while in [34] we have to wait until 50 time scale. Please notice also that we are using a smaller Reynolds number,  $Re = 817$  and in a more weakly stratified fluid,  $Fr = 2.712$ . It is also interesting to observe the differences with the non-stratified case, see Figure 6.7. We can observe that up to  $T = 6$  the kinetic energy transient is not too different between the two cases, while the enstrophy components show from the beginning a different behaviour. In both cases a  $T = 100$  spirals are well observed in the enstrophy isosurfaces, but in the stratified case they are more concentrated on the bottom of the domain, as a consequence of the buoyancy effect. After  $T = 10$  stratified and non-stratified flow differentiate completely their behaviour. Indeed in the stratified case a mild horizontal layering is observed.

In the stratified case, with the vertical shift, the density overturning by the two vortices generates horizontal density gradients that can force the horizontal baroclinic vorticity production terms in the incompressible Boussinesq, Navier-Stokes equations, see Figure 6.8 an example of potential energy isosurface, i.e  $|\rho|^2$ .

We have thus observed spirals formation and hypnotized a contribution due to the the horizontal baroclinic vorticity production terms. It is then natural to ask how these phenomena interact in the production of enstrophy. In Figure 6.9 we can observe the temporal evolution of these terms defined as in Eq. 6.2.

It can be observed that both have a peak value after 10 timescales, but the baroclinic term is three order of magnitude smaller than the vortex stretching one. It is also interesting to analyse how this terms are distributed in respect to the enstrophy isosurfaces. See for example left panel in Figure 6.10. Both terms are obviously concentrated where spirals are formed.

Figure 6.6 moreover shows the development of small-scale structures in the highly sheared region of the vortices. To address their origin, several authors [117] have proposed considering the local Richardson number  $Ri$ , defined in Eq. 6.1. It is proved that where the Richardson number is lower than  $1/4$ , [95, 58] the KelvinHelmholtz instability occurs. In right panel of Figure 6.10 this region is highlighted.

It is shown in literature that the secondary instability can lead to a turbulent regime. By computing the energy spectra, however, we observe a behaviour far from the  $-5/3$  Kolmogorov power law. Anyway we can clearly observed that the small scales gain energy up to  $T = 12$  when the viscous effect are dominant. We know from the literature that the secondary instability develops and lead to a  $-5/3$  spectrum for  $(Re - 400)Fr^2 > 4$  and  $ReFr^2 \geq 57$  [4]. Even if our test case satisfy both the inequalities, the transition to turbulence is not observed. Likely we are considering a too small Reynolds number and a weak stratification. Unfortu-

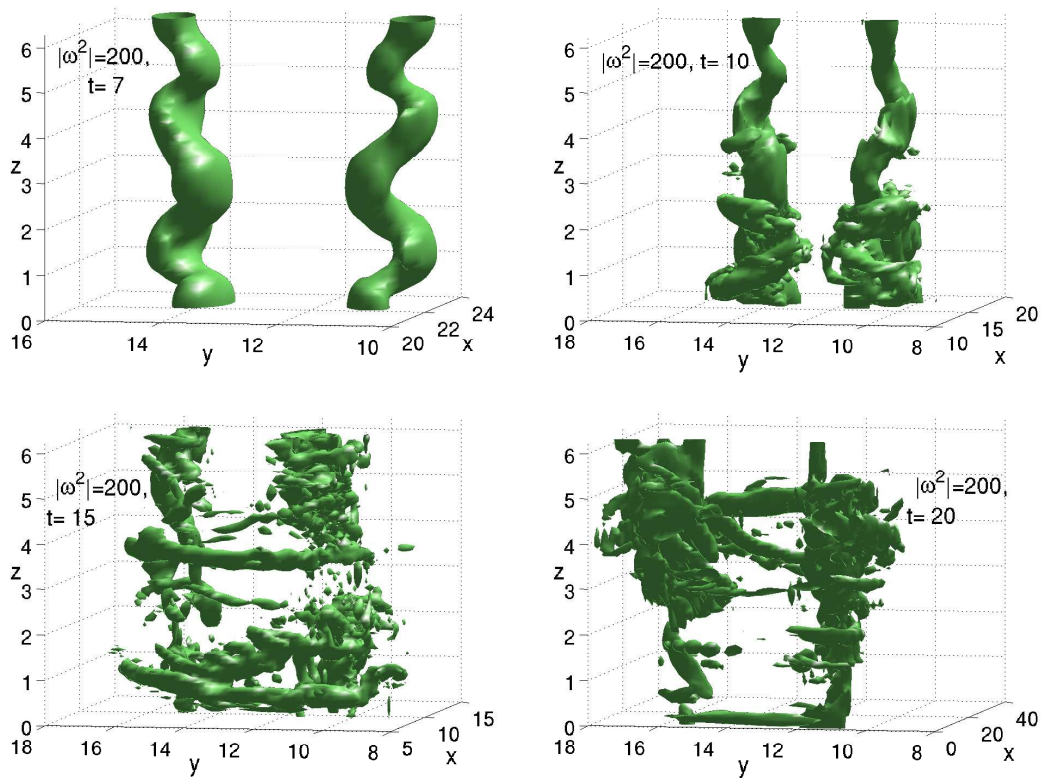


Figure 6.6: Entropy isosurface,  $|\omega^2| = 200$ . Stratified case,  $Fr=2.712$ . From time  $T = 10$  isosurfaces show spirals and the formation of small scales.

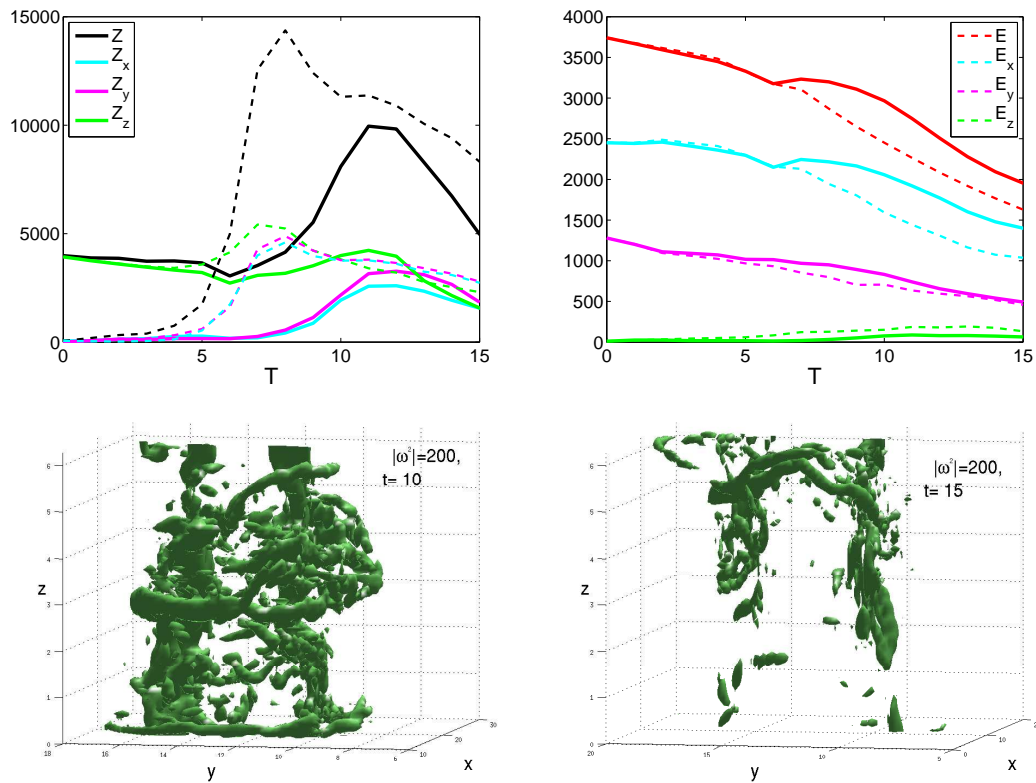


Figure 6.7: Comparison with the non stratified case. Top panels: time evolution of the enstrophy  $Z$  and kinetic energy  $E$ . The suffices  $x, y, z$  indicates enstrophy and energy computed taking into account only the  $x, y$  or  $z$  component of the vorticity and velocity respectively. Dotted line: non stratified case, solid line: stratified with  $Fr=2.712$ . Bottom panels: non stratified case enstrophy isosurface,  $|\omega^2| = 200$  at time  $T = 10, T = 15$ .

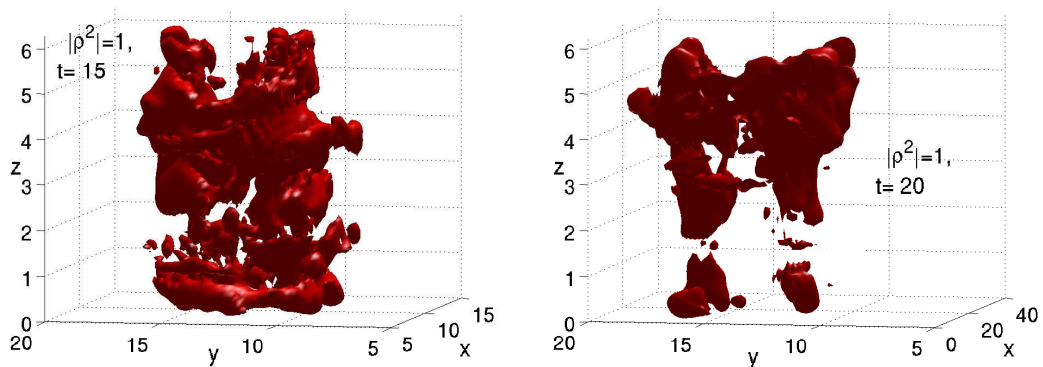


Figure 6.8: Potential energy isosurface,  $|\rho^2| = 1$

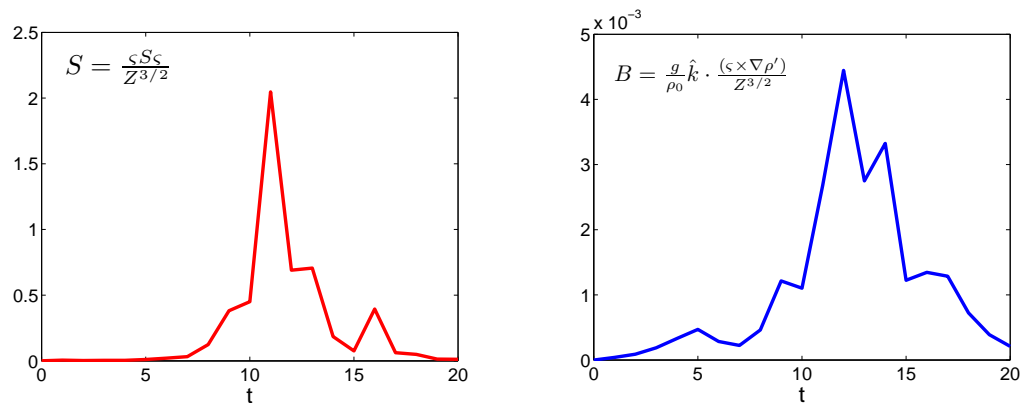


Figure 6.9: Time evolution of the maximum of the enstrophy production terms: vortex stretching (left panel) and baroclinic production (right panel).

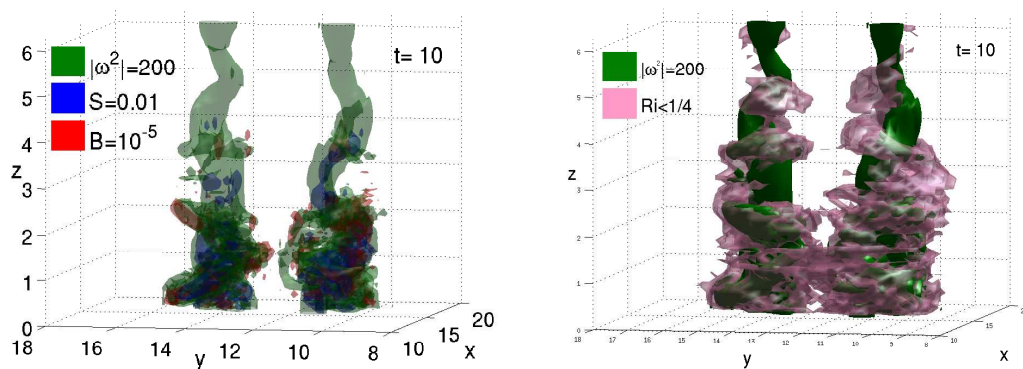


Figure 6.10: Left panel: isosurface of the enstrophy production term for  $t=10$ , both the stretching and the baroclinic term reach their maximum value where the spirals are formed. Right panel: region in which the Richardson number is smaller than  $1/4$ , i.e. where some Kelvin Helmholtz instability could occur.

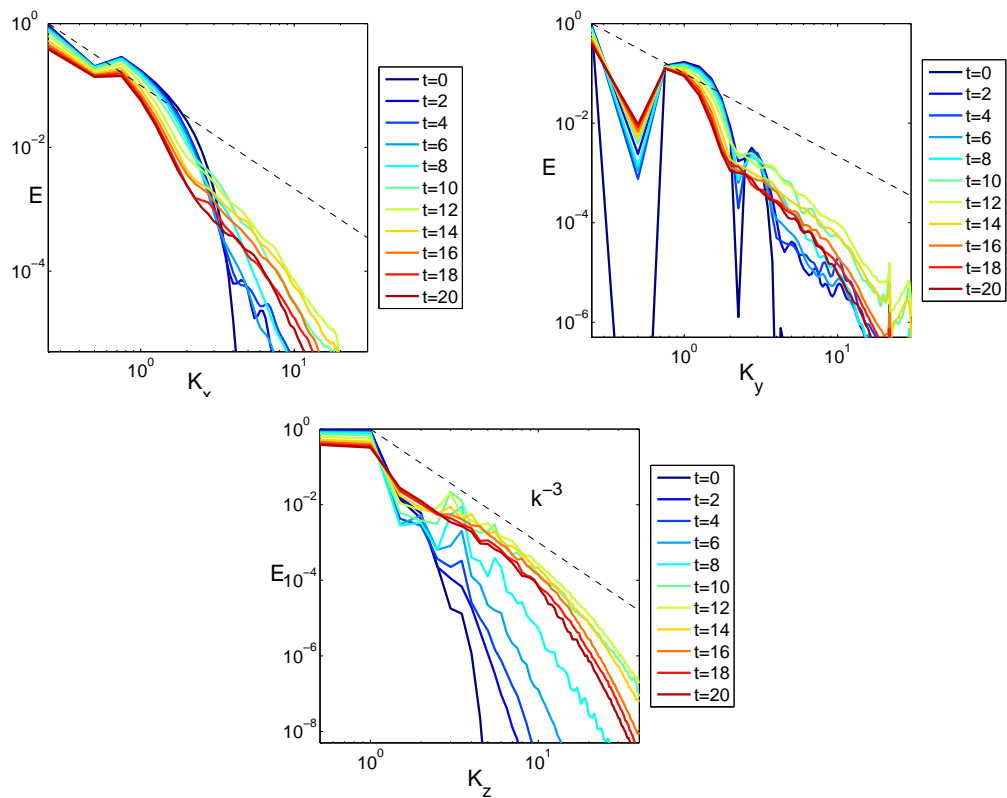


Figure 6.11: Unidirectional spectra in the different direction.

nately we had not enough computational time available to make an higher resolution strong stratified simulation, but we hope to be able to do it in the future.

## 6.5 Concluding remarks and future work

The evolution of a counter-rotating vortex pair in a stratified fluid has been extensively studied, in particular because it is one of the simplest flow on which the zig-zag instability develops and from which the buoyancy length scale naturally emerges as the vertical length [13, 14, 15]. Recently, Deloncle et al. [34], Waite and Smolarkiewicz [145] and Augier and Billant [3] have investigated the nonlinear development of the zigzag instability. They have shown that both the shear and gravitational instabilities appear at high buoyancy Reynolds number ( $R_b = Re Fr^2$ ) when the zig-zag instability has a finite amplitude leading to a transition to turbulence.

The first conclusion that we found is a faster instability mechanism on pairs of vertical vortices than those already proposed. The primary difference in the new initial condition is that the perturbations are not in the same vertical positions. This shift in the vertical allows a stronger horizontal density perturbation to form in a shorter time. The vertical layering observed in many calculations is reproduced and is identified with anti-parallel pairs of horizontal vortices propagating in different directions at different levels. The new configuration is then primed for developing a horizontal energy cascade that would start with the reconnection of these horizontal pairs. With this perturbation, following the formation of the first weak horizontal temperature gradients, the barotropic (stretching) and baroclinic (from horizontal temperature derivatives) vorticity production terms never cancel and it took only about 10 characteristic timescales for significant bends to form. Once the bends form, strong horizontal anti-parallel vorticity forms in the stream-wise direction at the tips of the bends, which then pulls these bends into the zig-zags.

Despite the initial conditions are very simple and very far from the turbulent state Augier, Chomaz and Billant [4] observe a  $-5/3$  horizontal spectra. The vertical spectra, instead, exhibits a  $-3$  slope in range of large scales ( power-law that seems to be due to the vertical deformations of the dipole induced by the zig-zag instability) and a  $-5/3$  slope for the small scales (indicating a return to isotropy). Moreover in previous study on column vortex dynamics on Euler equations and quantum turbulence [68] it seems that a second vortex reconnection is needed in order to see a  $-5/3$  spectrum. In the Billant et al. results a vortex reconnection doesn't appear, see Figure 6.12. We have tried to investigate if they miss to identify the reconnection or some other phenomena that can provide good physical explanation of the occurrence of such spectra. We are interested in whether it can be tied to other physics like, as the Lundgren model [83]. He proposed a model for the intermittent fine structure of high Reynolds number turbulence. The model consisted in slender axially strained spiral vortex solution of the Navier Stokes equations and lead to a  $k^{-5/3}$  energy spectrum consistent to the Kolmogorov ones. The cascade is produced by the tightening of the spiral turns by the differential rotation

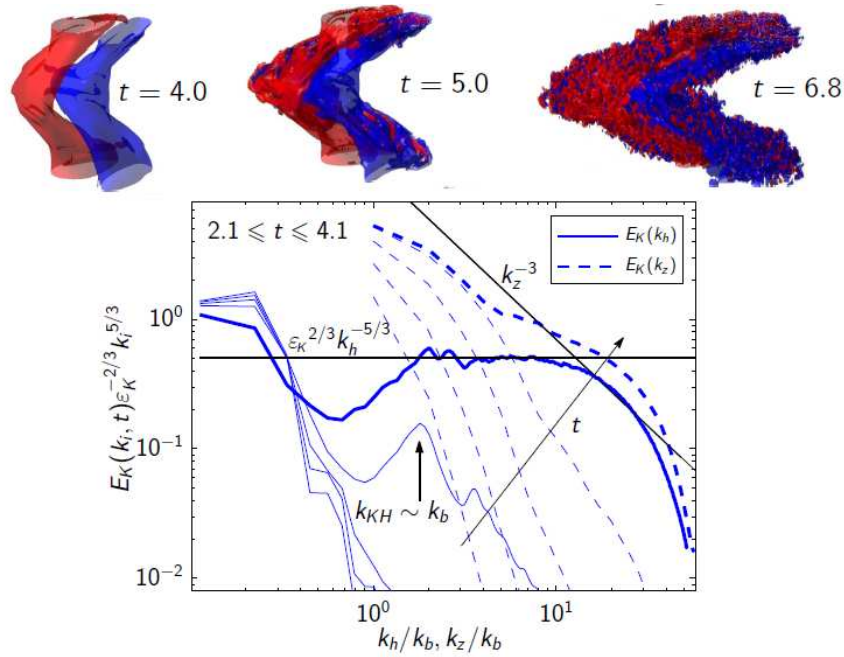


Figure 6.12: Spectral analysis of the transition to turbulence from a dipole in stratified fluid [4]

of the induced swirling velocity. Unfortunately this study has yet to be concluded. In fact, from our simulations we are able to see the formation of spirals and contribution given by the vortex stretching, but we do not reach the  $k^{-5/3}$  power law in the energy spectrum.

We have to perform simulations in a much bigger computational grid to proof our hypothesis, but at until now we have not had enough computational time available. With the bigger simulations we would like to clearly identify the secondary source of vortex stretching that is needed to generate the  $-5/3$ , from the Lundgren model. Moreover Waite and Smolarkiewicz [145] and Augier and Billant [3] find the Kelvin Helmholtz instability for really low value of the Froude number ( $Fr \leq 0.15$ ). As second goal we would like to consider whether the Froude number and Brunt Vaissala frequencies necessary for achieving the observed KH instability are physical, or in what context they will be. If we found that the real atmosphere is not as stratified as we will find is necessary in the vortex dipole calculations, then we need to think about what will give the KH instability without being this extreme. And finally the bigger questions of how this fits into the transition at roughly the synoptic scale when the atmosphere starts the transition from very large-scale nearly two-dimensional dynamics towards dynamics with a cascade of energy to small scales, even if it is not fully three-dimensional.

## Chapter 7

# Turbulent mixing in stratified flows. An application to cloud dynamics

Fluid entrained, or otherwise introduced in a turbulent region, is transported and dispersed across it by motions induced from the largest to the smallest eddies, where molecular diffusion has the opportunity to act, and where the ability of high Reynolds number turbulent flow to generate large interfacial surface area permits the otherwise slow molecular mixing to proceed effectively. Turbulent mixing can be viewed as a three-stage process of entrainment, dispersion, and diffusion, spanning the full spectrum of space-time scales of the flow.

The turbulent diffusion is complex and discrete structures or processes, spatially localized within the system, may exist. To obtain a better handling of fundamental issues, it has been adopted an approach where the turbulence self-diffusion is modelled by the interaction between two different isotropic turbulent fields. This simplifies the main mechanisms. In fact, it does not include the non-linear production of turbulent energy. However, it retains two of the most important features present in real flows: inhomogeneity and anisotropy.

Recent studies revealed the generation of small-scale anisotropy in non-stratified turbulence self-diffusion. A long-term interaction must be active to transfer to small scale the information on the anisotropy of the initial and boundary conditions [140]. Data from direct numerical simulations show that there is a departure of the longitudinal velocity derivative moments from the values found in homogeneous isotropic turbulence (HIT) and that the anisotropy induced by the presence of a kinetic energy gradient has a different pattern from the one generated by an homogeneous shear. Other results concern the relationship between the correlation length and intermittency.

A variation of the correlation length is not necessary to depart from Gaussianity [141, 138]. However, if the correlation length variation is concurrent with that of the energy, the mixing is enhanced, if is opposite, the mixing is decreased [138]. The transport of a passive scalar or a stable stratification added to the system highlight other phenomenology. The dimensionality



of the system is in particular of great relevance for some aspects (temporal mixing growth and vorticity suppression).

Mixing mechanisms in stratified fluids depend on the nature of the background stratification and are of course a more complex mechanism due to the inhibition of the vertical motions. As discussed in Chapter 5 stratification is very typical of atmospheric flows. In particular we are interested in the mixing process that involve clouds and clear air.

Warm clouds as stratocumuli swathe a significant part of earth's surface and play a major role in the global dynamics of atmosphere by strongly reflecting incoming solar radiation – thus contributing to the Earth's albedo – so that an accurate representation of their dynamics is important in large-scale analyses of atmospheric flows [149]. They are controlled by the tight interplay between radiative driving, turbulence, surface fluxes, latent heat release, and entrainment. Among them, the mixing and entrainment processes at the cloud top have been identified as fundamental to determine the internal structure of warm clouds, so that a clear and complete understanding of their physics is required [43]. As pointed out by Malinowsky *et al.* [88], data from most field campaigns and large-eddy simulations are too poorly resolved to allow to infer the details of the interfacial layer, even if they indicate that, in order to allow for entrainment, a high level of turbulence must be present. For this reason, in this chapter we study the local transport through a clear air/cloud interface through DNS (Direct Numerical Simulation). As our focus is on the dynamics of the smallest scales of the flow which influence the microphysics of warm clouds, we have simulated an idealized configuration to understand, under controlled conditions, some of the basic phenomena which occur at the cloud interface over length scales of the order of few meters. In these conditions, we solve scales from few meters down to few millimeters, that is, we resolve only the small scale part of the inertial range and the dissipative range of the power spectrum in a small portion ( $6\text{ m} \times 6\text{ m} \times 12\text{ m}$ ) of the atmosphere across the cloud - clear air interface. This allows us to investigate the dynamics of entrainment which occurs in a thin layer at the cloud top, which a smaller scale with respect to the scale explicitly resolved in large-eddy simulations of clouds [98]. This is a preliminary work, where we focus on two concomitant aspects of the cloud top mixing layer: the effect of the presence of a stratification and of a turbulent kinetic energy gradient. We do not consider the wind shear neither the phenomena linked to the processes of evaporation and condensation and radiative cooling which are important in conditions of buoyancy reversal [90, 91]. Therefore, our simulations were performed by applying the Boussinesq approximation to the Navier-Stokes momentum and energy equations together with a passive scalar transport equation which models the water vapour transport.

In next Section we contextualize and motivate better the present study. In Section 7.2 the physical problem is described; while the numerical results obtained are described in Section 7.3.

## 7.1 Rationale

Clouds cover about 70 percent of the Earth's surface and have an enormous effect on climate: Some clouds, especially low-lying hazy or puffy clouds, reflect sunshine and cool the planet; others, such as high, wispy clouds, trap heat emanating from Earth's surface and warm the planet. Clouds currently have an overall cooling effect on the planet, but as the Earth heats due to global warming, the type and position of clouds could change. So to predict climate change over the next 10 to 100 years, scientists need to be able to accurately predict what will happen to clouds. But despite simple ingredients—tiny droplets of water or ice crystals—clouds are extraordinarily complex entities governed by competing physical forces, and it takes a significant amount of computing power to calculate how they form and change. However, though scientists know the equations needed to model the physical processes that determine the formation and evolution of clouds, today's computers cannot handle the complex calculations that are required to simulate each and every cloud that forms across the globe. Instead, atmospheric scientists resort to dividing the planet into large boxes, or grid cells, ranging from 100 to 300 kilometres on each side. In each of these boxes, a computer algorithm calculates a coarse estimate of cloud formation and movement. This way the calculation becomes computationally feasible, but at the expense of fine detail. Since clouds are formed by small-scale atmospheric motions the interaction and combination of the different atmospheric motions—small and large—is difficult to be accurately represented in the large grid boxes. Because of this, clouds are not realistically simulated in current weather and climate models. The turbulence simulations could be used to develop more accurate statistical representations of clouds under different atmospheric conditions in larger grid boxes.

The effect of turbulence on cloud formation and precipitation is a controversial issue that has long divided the cloud physics community. The difficulty in measuring clouds at small scales and the lack of realistic cloud models that span all the relevant scales means that the precise effect of turbulence is hard to quantify (see Figure 7.1) and makes an assessment of its importance difficult. Nowadays this topic is a major research problem. Theoretical, computational and laboratory tools are applied to all scales of the problem [25]. A scheme of the length scales that characterize the atmospheric motions is shown in Figure 7.1. With this study we propose to investigate—through a toy problem—the mixing and entrainment that take place between clouds and the clean air surrounding [42]. Therefore we consider a problem with a length scale of the order of 10 meters. Compared to in situ measurement of the atmospheric energy spectra, as shown in Figure 7.2, we are able to simulate the lowest part of the inertial range and the dissipative one.

Since we are investigating an atmospheric flow motion we have also to make some consideration about the stratification. Usually, within the lower atmosphere (the troposphere) the air near the surface of the Earth is warmer than the air above it, largely because the atmosphere is heated from below as solar radiation warms the Earth's surface, which in turn then warms

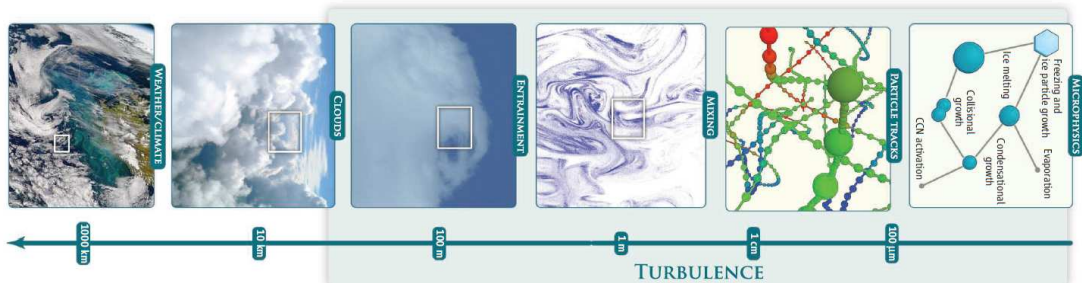


Figure 7.1: Turbulence on scales from hundreds of meters to fractions of millimetres effects the formation and dynamics of clouds, with consequences extending to the scale of weather and global climate (Picture taken from [18])

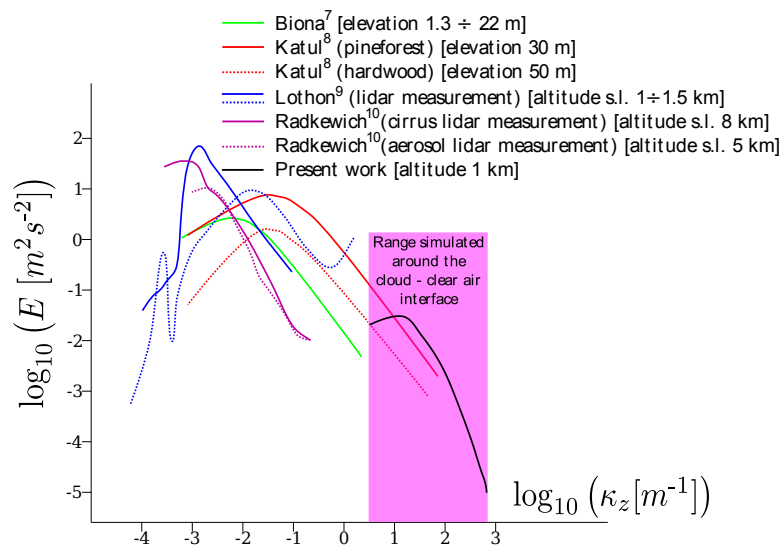


Figure 7.2: Kinetic energy spectra. Contextualization of present study (black spectra, small inertial and dissipative range) respect to spectra from in-situ atmospheric measurements [17, 62, 79, 113] (colored spectra, energy injection and low wave-number inertial scales).

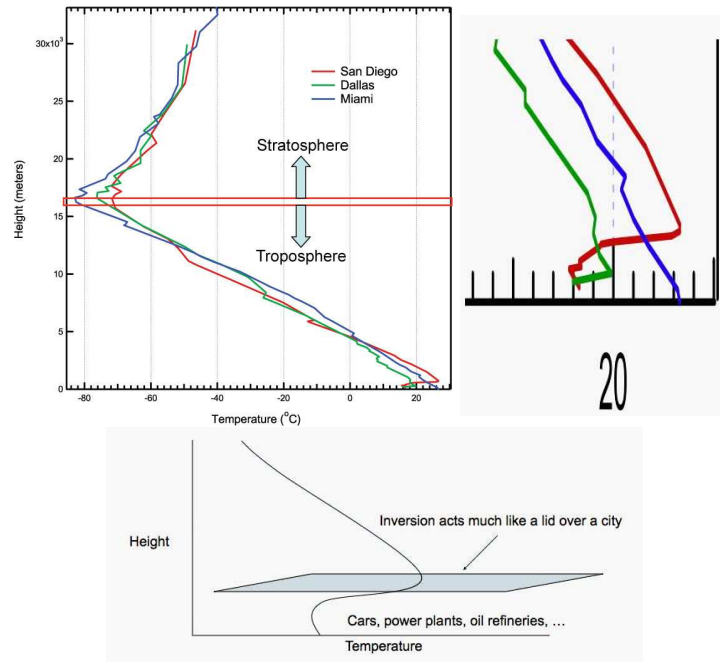


Figure 7.3: (*Top-Left*) Temperature as a function of height in the atmosphere measured by radiosondes at three different cities. Data from the University of Wyoming’s Department of Meteorology and from the University Center for Atmospheric Research RAP Real-Time Weather Data. (*Top-Right*) Zoom on the temperature inversion layers. (*Bottom*) Possible effect of an inversion layer.

the layer of the atmosphere directly above it, e.g., by thermals (convective heat transfer) [100]. Under certain conditions, the normal vertical temperature gradient is inverted such that the air is colder near the surface of the Earth. In wintertime, a temperature inversion occurs when cold air close to the ground is trapped by a layer of warmer air. In summer months it also occurs, but are a product of even hotter upper air trapping warm air close to the ground. An inversion layer acts as lid keeping the air beneath from penetrating higher into the atmosphere and limits the vertical extent of air mixing near the surface [9].

Figure 7.3 shows temperature as a function of height in the atmosphere measured by radiosondes at three different cities and the possible effect due to a temperature inversion.

The presence of these inversion layers plays an important role in atmospheric dynamics, as well as inhibiting the rates of vertical transport of scalars, such as water vapour contained inside the clouds. With our simulations we want to investigate how this kind of temperature profile affects the entrainment at the cloud - quiescent air interface.

## 7.2 The physical problem

We consider the interface between clear air and cloud in a  $6 m \times 6 m \times 12 m$  parallelepiped domain. As shown in figure 7.2, the system is composed by two homogeneous and isotropic turbulent regions that interact through a mixing layer, whose initial thickness has been set of the same order of the integral scale of the turbulence background  $\ell$ , here assumed equal to  $3 \cdot 10^{-2}$  m. The two isotropic regions have a different kinetic energy and we assumed that the kinetic energy is higher in the cloud than in the external region. The root mean square of the velocity inside the cloud is  $u_{rms} = 0.2$  m/s, and the energy ratio between the cloud energy  $E_1$  and the external region energy  $E_2$  is equal to 6.7. This energy ratio is of the same order of the ones measured in warm clouds (see, e.g., [88]) and, furthermore, it allows us to compare our results with experiments on shearless mixing (see [144, 139]) in absence of any stratification. In our simulations the Taylor microscale Reynolds number  $Re_\lambda$  of the higher energy region is equal to 250. The water vapour concentration  $\chi$  is considered as a passive scalar. The Prandtl ( $Pr = 0.74$ ) and the Schmidt number ( $Sc = 0.61$ ) considered refers to an altitude of 1000 m s.l.

Since we want to simulate what happens in the presence of an inversion layer the equation that describes a stratified flow, Eq. 5.23, has to be expressed in term of temperature instead of density:

$$\nabla \cdot \mathbf{u}' = 0 \quad (7.1)$$

$$\frac{\partial \mathbf{u}'}{\partial t} + (\mathbf{u}' \cdot \nabla) \mathbf{u}' = -\nabla \frac{\tilde{p}}{\rho} + \nu \nabla^2 \mathbf{u}' + \alpha \mathbf{g} \theta' \quad (7.2)$$

$$\frac{\partial \theta'}{\partial t} + \mathbf{u}' \cdot \nabla \theta' + u_3 G = \kappa \nabla^2 \theta' \quad (7.3)$$

$$\frac{\partial \chi}{\partial t} + \mathbf{u}' \cdot \nabla \chi = d_\chi \nabla^2 \chi, \quad (7.4)$$

Here the temperature  $\theta$  and pressure  $p$  are composed as the sum of a fluctuation ( $\theta'(\mathbf{x}, t)$ ,  $p'(\mathbf{x}, t)$ ), a static component ( $\tilde{\theta}(x_3) = Gx_3$ ,  $\tilde{p}(x_3) = \alpha \tilde{\theta}(x_3)G$ ) and a reference constant ( $\theta_0$ ,  $p_0$ ), where is the fluid-dynamic pressure,  $\alpha$  the thermal expansion coefficient,  $g$  the gravity acceleration),  $u'$  is the velocity fluctuation and  $\chi$  is the vapour concentration of the air - water vapour mixture present in the cloud, here considered as a passive scalar. The constant  $\kappa$  and  $d_\chi$  are respectively the thermal and water vapour diffusivity. The initial conditions for the temperature perturbation is described in Figure 7.2 and in Table 7.2. The ratio between inertial and buoyancy forces is expressed by the Froude number  $Fr$ , based on the maximum gradient within the initial interface, which ranges from 31.2 (negligible stratification) to 0.62 (strong stratification).

The simulations are performed using our home produced computational code that implements a pseudospectral Fourier-Galerkin spatial discretization and an explicit low storage fourth order Runge-Kutta time integration scheme. Evaluation of non-linear (advective) terms

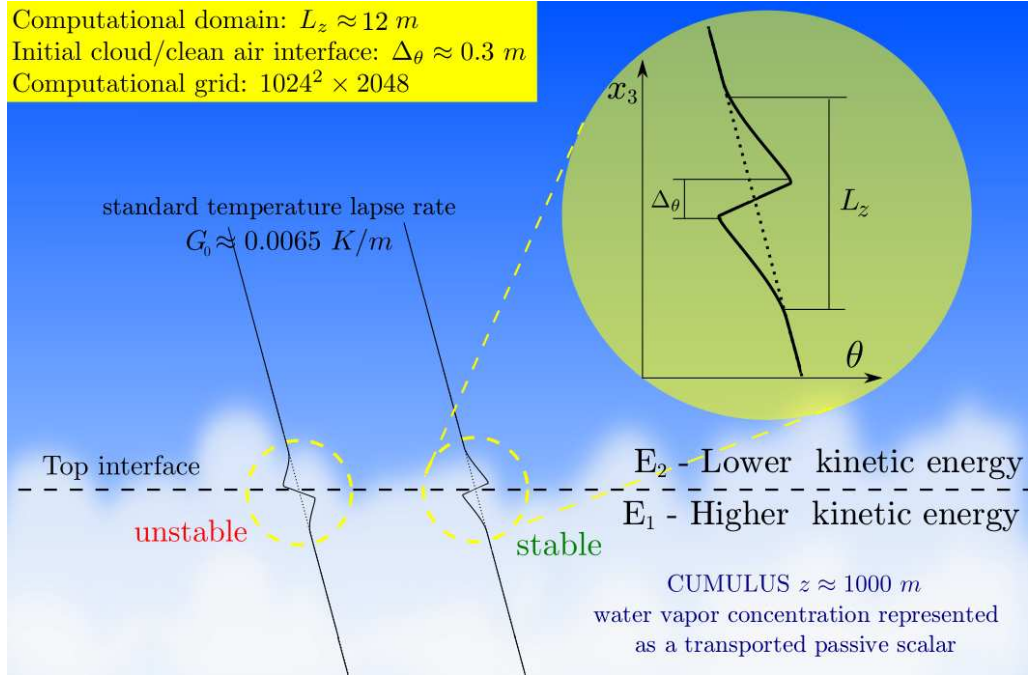


Figure 7.4: Scheme of the initial conditions.  $E_1$  is the mean initial turbulent kinetic energy of the bottom region (inside the cloud),  $E_2$  of the upper region (outside the cloud). For the top cloud mixing here presented we consider  $E_1/E_2 = 6.7$ . The water vapour is initially present only inside the cloud (bottom region). The zoom in the yellow circle is an example of initial temperature perturbation  $\theta'$  of the standard boundary layer lapse rate.

Table 7.1: Initial stratification level parameters.  $G$  is the maximum gradient of  $\theta$ , expressed in terms of the standard troposphere lapse rate  $G_0 = 0.0065 \text{ Km}^{-1}$ ;  $N_{ci} = \sqrt{\alpha \theta_0 g \frac{d\theta}{dx_3}}$  is the characteristic Brunt-Väisälä frequency of initial condition. The Froude number  $Fr = \frac{u'_{rms}}{N_{ci} \ell}$  and the Reynolds Buoyancy number  $Re_b = \frac{\varepsilon N^2}{\nu}$  give a measure of the order of magnitude of the buoyancy forces compared with the inertial terms ( $\varepsilon$  is the initial energy dissipation rate,  $\nu$  the kinematic viscosity).

$G$	$\Delta T$ [K]	$N_{ic}$ [ $s^{-1}$ ]	$Fr$	$Re_b$
$2G_0$	4.0e-3	2.13e-2	31.2	7
$30G_0$	6.0e-2	5.24e-2	12.7	112
$100G_0$	2.0e-1	1.50e-1	4.4	273
$500G_0$	1.0e0	3.35e-1	1.8	833
$5000G_0$	1.0e1	1.06e0	0.62	2635

Table 7.2: Simulations parameters.

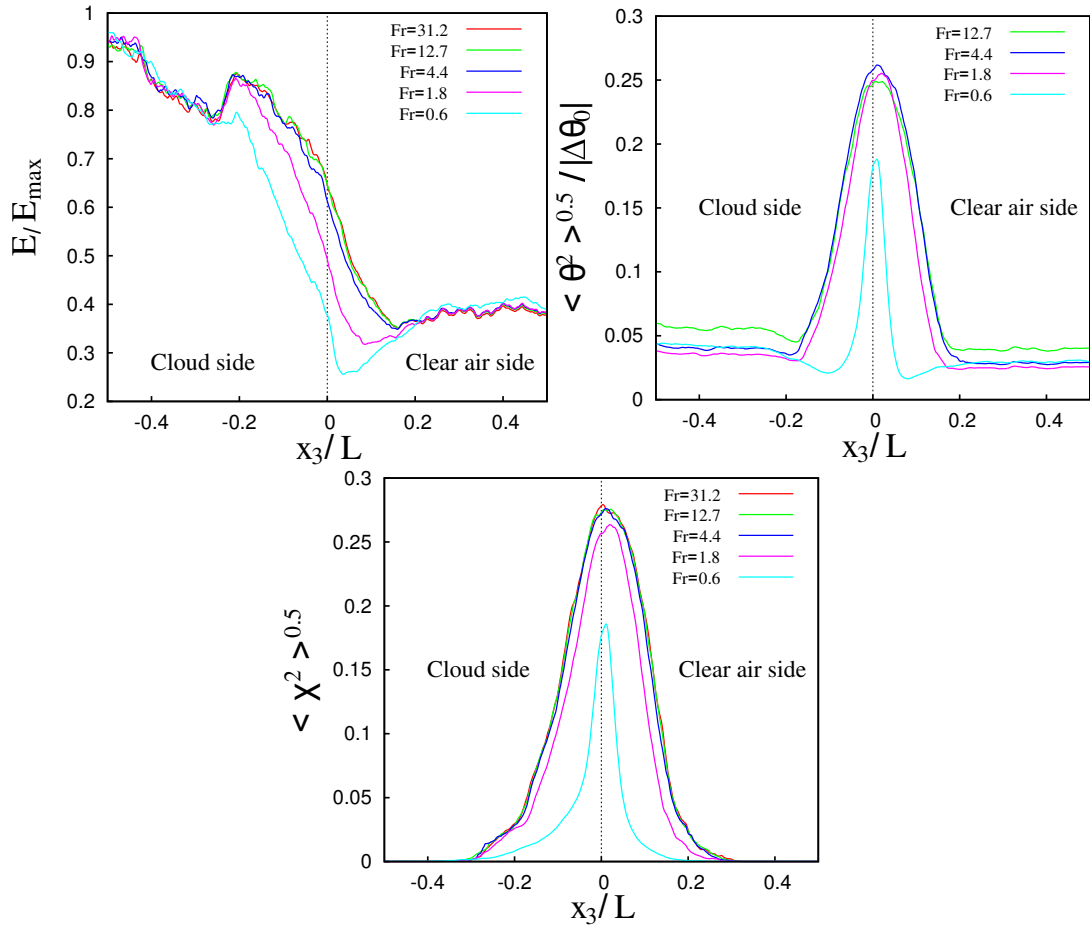


Figure 7.5: Spatial distribution along the vertical coordinate  $x_3$  of the kinetic energy (a), temperature variance (b) and water vapour concentration variance (c) at  $t/\tau \approx 6$  for different levels of stratification.

is performed through the 3/2 de-aliased method [59]. The initial conditions for the velocity field are obtained by a linear matching of two different isotropic homogeneous turbulent fields (that are randomly generated, respecting physical conditions imposing spectra, solenoidality, integral scale and kinetic energy)[138]. The grid has  $1024 \times 1024 \times 2048$  points, and allows to capture all the turbulent scales from the greatest (integral scale  $\ell$ ) to the smaller (Kolmogorov scale  $\eta$ ). The computational code uses a distributed memory paradigm through the MPI libraries: the simulation were performed at the TGCC Curie supercomputer within the PRACE project n° RA07732011 for a total of 3 million cpu-hours.

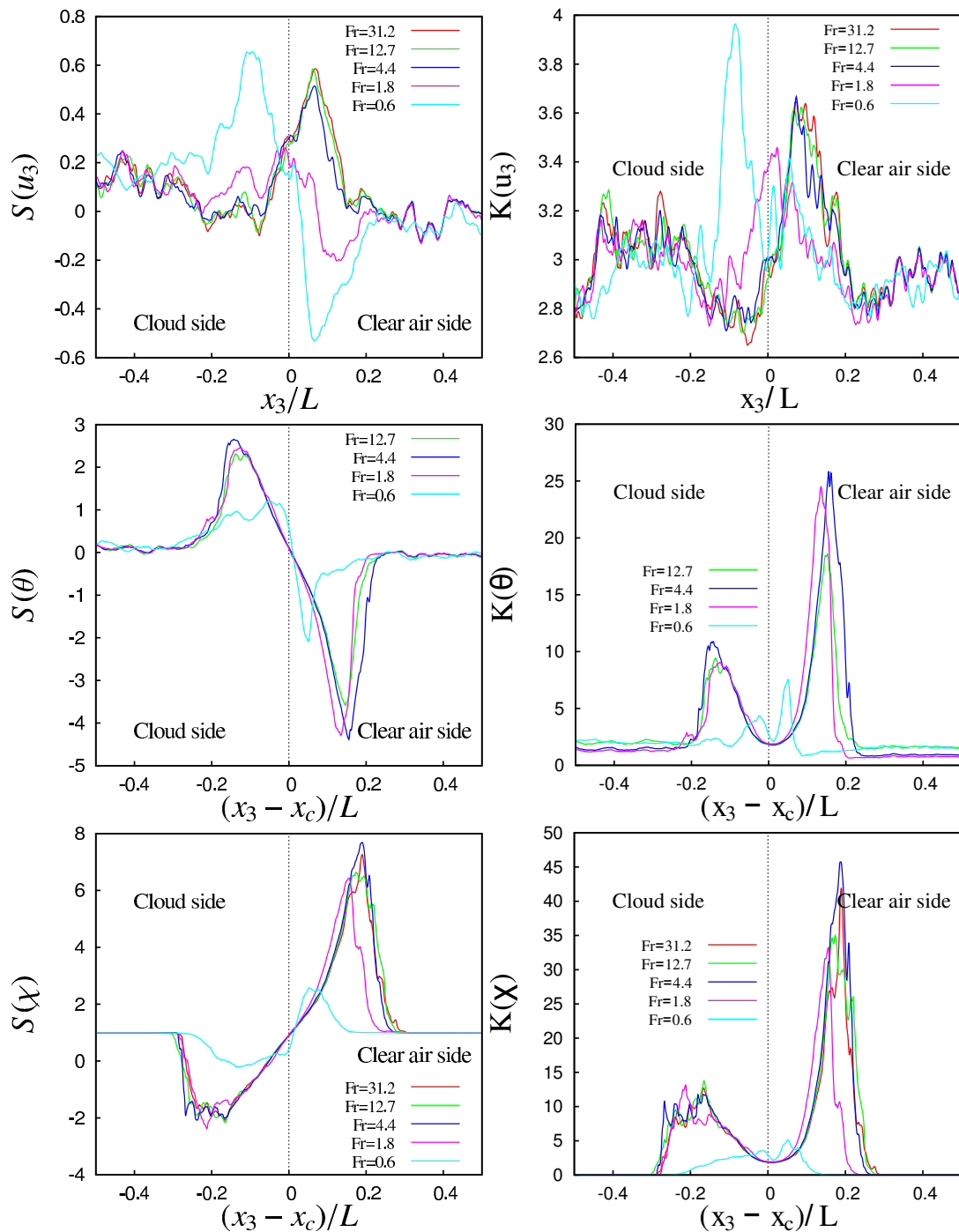


Figure 7.6: Spatial distribution in the vertical direction  $x_3$  of the skewness and the kurtosis of vertical component of the velocity (*a,b*), temperature (*c,d*) and water vapour concentration (*e,f*) at  $t/\tau = 6$  for different levels of stratification.



### 7.3 Results

According to the ratio between buoyancy force and kinematic forces (that are advection and diffusion), the evolution of the system can be split in two main stages. As long as the ratio remains small, there are no significant differences with respect to a non-stratified case. On the contrary, as the stratification perturbation level become higher, buoyancy effects are no more negligible: differences are present from both a quantitative and qualitative point of view. These considerations can be observed through the statistical analysis of the simulated fields. The statistics are computed by averaging the variables in the planes normal to the mixing direction (with a sample of  $1024 \times 1024$  data-points), focusing on the variation along the vertical (non-homogeneous) direction. The effects of the different stratification levels are clearly visible on the second order moment of velocity, temperature, and vapour as shown in Figure 7.5 (*a,b,c*). When the stratification level is mild ( $Fr > 4$ ) there are no relevant differences with respect the neutrally buoyant flow, while significant differences appears for intense stratification ( $Fr < 2$ ). In particular, in correspondence of the local temperature perturbation, the formation of a layer with a pit of kinetic energy can be observed. The presence of such a layer deeply changes the physics of the system, because in this situation two interfaces are produced. The first interface, (which is present also in the absence of stratification), now separates the high turbulent energy region from the pit, while the second one (not present without stratification) separates the low turbulent energy region from the center of the mixing layer. Therefore, a strong stratification induces a physical separation between the two external regions, greatly decreasing the interaction between them. Both interfaces present an intermittent behaviour, as shown in Figure 7.6 (*a,b*) by skewness and kurtosis distribution (respectively third and fourth moments normalized with the local variance). In fact, two peaks of skewness and kurtosis can be observed in the highly stratified case: one is placed inside the cloud, and the other is placed close to the position of the intermittency peak in case of absence of stratification, see data at  $Fr = 0.6$  in Figure 7.6 (*a*). Observing the magnitude of the kurtosis maximum in Figure 7.6 (*b*), it can be noted that the peak inside the cloud reaches values as high as 4, that are about the 10% larger than when the stratification is milder.

It can be also observed that higher levels of stratification produce a relevant reduction of intermittency in the flow, with a drop of about 70% in the peaks of skewness and kurtosis. The interaction between the two regions aside the interface is greatly reduced, so the fluctuation at the sides of the mixing layer are damped, preventing the formation of the intermittent layer typical of the passive scalar transport [84, 60]. This strong reduction in skewness and kurtosis is coupled with a slight increase in the higher order moments of vertical velocity – for sufficiently strong stratification – which is in fair agreement with the trend observed in [112]. Moreover, observing both Figures 7.5 and 7.6, it is clear that the thickness of the mixing layer is reduced in case of intense stratification (see next section for more details).

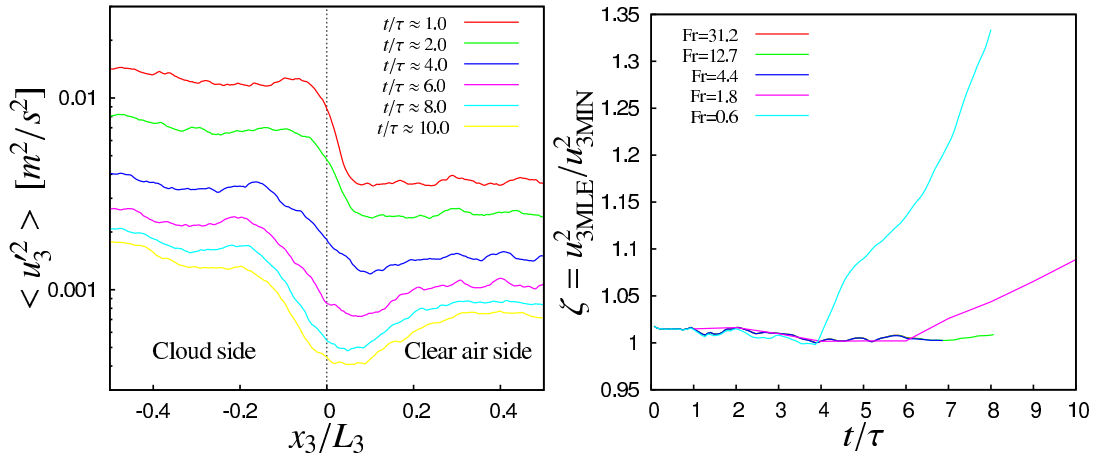


Figure 7.7: (a) Temporal evolution of the spatial distribution along the vertical direction  $x_3$  of the turbulent kinetic energy when  $Fr=1.8$ . A pit of energy appears after about 6 eddy turnover times in correspondence of the original interface. (b) Temporal evolution of the ratio  $\zeta$  between the mean vertical velocity variance in the lower energy (clear air side) region  $u_{3,MLE}$  and the minimum value of the vertical velocity  $u_{3,MIN}$ . When this ratio departs from 1, a pit of kinetic velocity appears as shown in (a).

### 7.3.1 The onset of a kinetic energy pit

As shown in Figure 7.7 (a), in case of high stratification level, in the center of the domain – where the initial temperature step is placed – the onset of a layer with a kinetic energy lower than both the external regions can be seen. This layer can be considered as a pit of kinetic energy. Varying the stratification intensity, the genesis and the evolution of such pit can be measured by considering the ratio  $\zeta$  between the variance of vertical velocity in the low energy region  $u_{3,MLE}^2$  (mean value) and in the center of the pit  $u_{3,MIN}^2$  (where the variance reaches its minimum); the temporal evolution of  $\zeta$  is shown in Figure 7.7 (b). Qualitatively similar results have been observed in the large-eddy simulations of stratocumulus-topped planetary boundary layer carried out by several physics of the atmosphere research group, as described in [97, fig.7(c) and 8(a) at pag. 11]: in particular, in the case of sufficiently strong stratification, the trend of our vertical velocity variance, in Figure 7.3.2 (a), is analogue to those observed in the LES carried out by the NCAR group (Deardoff TKE model [96]) and the WVU (ARAP TKE model [132]). In this simulations they consider the planetary boundary layer with  $Re_\lambda \approx 5500$  and  $Fr \approx 0.4$ .

A visualization of such phenomenology is represented in Figure 7.3.1, where the vertical velocity fluctuations in a vertical slice of the domain are represented using an elevation plot (where such elevation is proportional to the square of  $u_3$ ). In presence of a mild stratification,  $Fr = 12$ , even after 8 time scale, there is a smooth mixing layer between the high (left) and the low (right) energy regions. The differences in the case of strong stratification, with  $Fr = 0.62$ ,

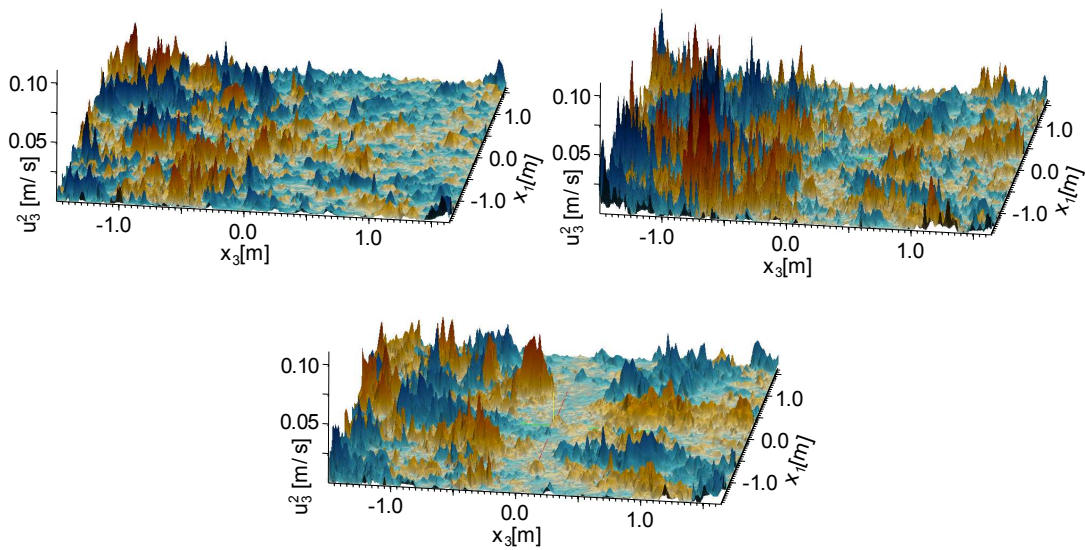


Figure 7.8: Visualization of the vertical component of the velocity in a vertical plane. The elevation is proportional to the square of vertical velocity fluctuations and the colors respect the velocity directions (blue for downward, red for upward) in various case:  $Fr = 12$  after 8 eddy turnover times (a) and for  $Fr=0.62$  after 4 and 8 eddy turnover times (panels b, c respectively). In the last two panels it can be observed the formation of the pit of kinetic energy.

after 4 time-scales (b) and 8 time scales (c), are clearly visible: a separation layer is present in the center of the domain, that becomes even more evident as the time pass by.

As said, the presence of the pit generates a physical separation between the two external regions, by damping the turbulent mixing, and thus reducing the exchange of information. As a consequence, there is a saturation of the thickening of the mixing layer  $\Delta_E$ ; such interruption of the growth is represented in Figure 7.9 (a)

Looking to the temperature mixing layer thickness  $\Delta_\theta$ , shown in Figure 7.9 (b), it can be seen that, for strong stratification, the thickening stops approximately after the same amount of times scale required by  $\Delta_E$ . In that case, contrary to what observed for the kinetic energy, the thickening does not stop suddenly, but rather with a transient that lasts a couple of time scales.

### 7.3.2 Entrainment

The entrainment of clear air inside the cloud is an important aspect of the top cloud interface as it concurs in the evaporation/condensation of droplets inside a cloud [149].

In any plane parallel to the interface, in absence of a mean velocity, only downward velocity fluctuations can transport clear air into the cloud. Their presence can be represented by a marker function  $\psi$  that is equal to 1 where  $u_3$  is negative, and 0 otherwise. Its average in each horizontal plane, shown in Figure 7.3.2 (a), shows a small deviation from the mean value of

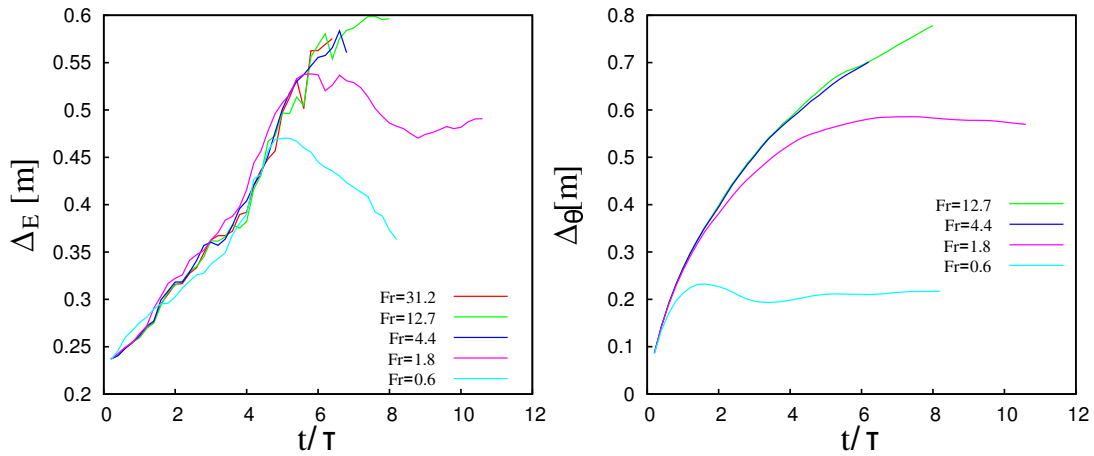


Figure 7.9: Thickness of the mixing layer of velocity (a) and temperature (b). For both fields, the mixing layer thickness is the same as defined in [60].

0.5 which would be observed in an homogeneous and isotropic flow. This implies that upward and downward fluctuations are almost equally distributed; the maximum departure from an homogeneous distribution is about 4%, and the spatial distribution of  $\psi$  looks like the one which has been observed in the third order moment of the velocity, see Figure 7.6 (a).

The entrainment of clear air is responsible of the growth of the cloud. In fact, the velocity  $w_e = dx_{3,i}/dt$  of the cloud top interface ( $\langle x_{3,i} \rangle$  is the mean vertical position of the cloud top, defined as the position where the mean vapor concentration is 25%) has often been used as a parameter to measure the entrainment rate [90, 98]. In Figure 7.3.2 (b), the temporal decay of  $w_e$  for different levels of stratification is represented. In presence of weak stratification, that is  $Fr$  larger than 4, its value gradually decreases with an almost exponential law, due to the decay of the kinetic energy. On the contrary, when the stratification is stronger, the damping of  $w_e$  is much faster, and the entrainment vanishes after few times scale, when the presence of the pit of kinetic energy substantially reduces the flux of clear air inside the cloud.

Figure 7.3.2 (c) shows the vertical derivative of the downward flux of clear air when  $Fr = 1.8$ . As the flow evolves, the downward flux reduces and its derivative, which represents the net variation of  $1 - \chi$  at a given instant, rapidly tends to zero inside the cloud. This implies that the entrainment of clear air is confined to a thin interfacial layer.

## 7.4 Conclusion

In this chapter we have carried out numerical simulations on the transport of energy and scalars in a turbulent shearless mixing layer associated to temporal perturbation of the temperature lapse rate across the clear air - cloud interface. The perturbation locally introduces a stable

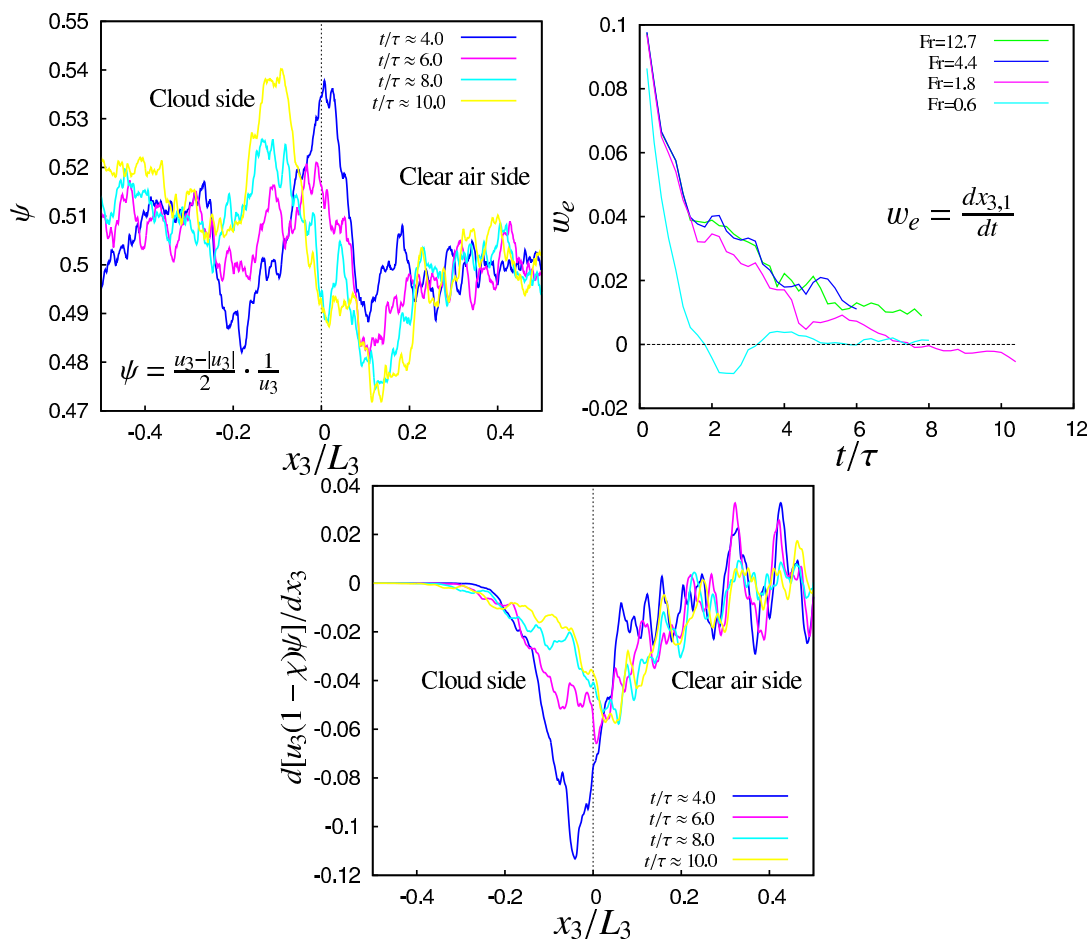


Figure 7.10: Evolution of the entrainment across the top cloud. Fraction  $\psi$  of downwards velocity (a) and vertical variation of the mean flux of clear air into the cloud (c) when with  $Fr=1.8$ . Evolution of entrainment velocity  $w_e$  normalized with the high kinetic energy  $E_1$  root mean square (b), see figure 7.2.

stratification. This idealized configuration models some of the phenomena which are present in the kinetic dynamics of the cloud and clear air interaction, namely those linked to turbulent mixing and entrainment.

We have shown that this flow configuration develops an horizontal layered structure characterized by a sublayer – with a kinetic energy lower than both the external regions – which acts as a barrier for the transport between the cloud and the external ambient. In our transient simulations, this flow structure appears when the buoyancy terms becomes of the same order of magnitude of the inertial ones, therefore the time needed for this transition becomes shorter when the stratification is more intense. Once buoyancy dominates and the new flow regime is reached, we observed two highly intermittent regions with opposite kinetic energy gradients. As a direct consequence, the entrainment is damped.

Results obtained so far seemingly support the large eddy simulations of stratocumulus - topped planetary boundary layers.

## Concluding Remarks

In this thesis we have presented interesting phenomenology on perturbation dynamics in both laminar and turbulent flows. Stability, transition and turbulence are the three main flows regime and in this thesis they have been investigated through an initial value problem.

First laminar two dimensional flows is considered. By varying the wave number over a large interval of values, we analyse the phase and group velocity of linear three-dimensional travelling waves both in the plane wake and channel flows. We solved the Orr-Sommerfeld and Squire eigenvalue problem and observe the least stable mode. At low wave numbers, we observe a dispersive behaviour amenable to the typical solution belonging to the left branch of the eigenvalue spectrum. By rising the wave number value, in both flows, we observe a sharp dispersive to nondispersive transition. This is located at a critical wave number of the order of the unity. Beyond this transition, the observed dominant mode belongs to the right branch of the spectrum.

We also focused on the transient behaviour of the phase velocity of small amplitude three-dimensional travelling waves. Given an arbitrary initial condition, we verified that the kind of transient highly depend on the wavelength value with respect to that of dispersion/nondispersion transition. Furthermore during the transient, the phase velocity may oscillate with a frequency which is equal to the width of the eigenvalue spectrum. These transients may show abrupt changes that are related to the Reynolds number, wave angle, symmetry and the vorticity distribution of the initial condition. The existence of an intermediate transient in which the solution becomes near-similar is empirically proved.

The intermediate transient is the most interesting period to investigate. Indeed, at these times the perturbations show interesting scaling properties. The velocity components profiles maintain the same shape every time inside this range, thus they show a self- similar behaviour.

Moreover we show that inside the intermediate term the kinetic energy distribution follows a power law that is very similar to the one observed in turbulent state, where the energy scales as  $k^{-5/3}$  (Kolmogorov 1941). Even if, of course, in this case the energy power law can not represent an energy cascade, these findings lead us to hypothesize that some properties considered typical of turbulent flow, such as self similarity and scaling of the energy spectrum, are instead a more general property of the Navier Stokes equations.

We have then considered a three-dimensional base flow that is the supercritical FSC cross-

flow boundary layer. We analyse the temporal evolution of individual three-dimensional travelling waves subject to near-optimal initial conditions and considered an extended portion of the parameter space. Our parametrization included the wave-number, the wave-angle, the cross-flow angle, the Hartree parameter and the Reynolds number. Special focus was given to the role played by the waveangle in inducing very steep initial transient growths in waves that proved to be stable in the long term. We found that the angular distribution of the asymptotically unstable waves and of the waves that show a transient growth depends greatly on the value of the cross flow angle and wave-angle as well as on the sign of the Hartree parameter, but depend much less on the Reynolds number. In the case of the decelerated boundary layer, at sufficiently short wavelengths, transient growths become much more rapid than the initial growth of the unstable waves. In all cases of transient growth, pressure perturbations at the wall are not synchronous with the kinetic energy of the perturbation.

The transition to turbulence is then considered through the dynamics of disturbances in the context of the zig-zag instability. In the presence of a stable stratification, a particular kind of instability can occur by perturbing two counter-rotating column vortices. The vortices are stretched and bended in such a way as to assume a zig-zag shape. This zig-zag shape in turn favours the occurrences of a second instability, the Kelvin Helmholtz instability, which leads to the formation of smaller scales. This brings us to a turbulent regime. Analysing this flow, we wondered if it was possible to explain and model the obtained inhomogeneous, anisotropic and stratified turbulence through the turbulent model proposed by Lundgren [83]. Unfortunately at the moment we have not yet succeeded in this aim.

Eventually for the turbulent regime, we considered a simplified physics of the cloud interface where condensation, evaporation and radiation are neglected and momentum, thermal energy and water vapour transport is represented in terms of the Boussinesq model coupled to a passive scalar transport equation for the vapour. The interface is modelled as a layer separating two isotropic turbulent regions with different kinetic energy and vapour concentration. In particular, we focus on the small scale part of the inertial range as well as on the dissipative range of scales which are important to the micro-physics of warm clouds. We have numerically investigated stably stratified interfaces by locally perturbing at an initial instant the standard temperature lapse rate at the cloud interface and then observing the temporal evolution of the system.

When the buoyancy term becomes of the same order of the inertial one, we observe a spatial redistribution of the kinetic energy which produces a concomitant pit of kinetic energy within the mixing layer. In this situation, the mixing layer contains two interfacial regions with opposite kinetic energy gradient, which in turn produces two intermittent sublayers in the velocity fluctuations field. This changes the structure of the field with respect to the corresponding non-stratified shearless mixing: the communication between the two turbulent regions is weak, and the growth of the mixing layer stops.



***Aknolegments***

I would like to thanks D. Tordella, J. J. Riley, W. O. Criminlae, R.R. Kerr, G. Staffilani and R. Rosales which provided me a scientific guidance.

My sincere thanks also goes to M. Iovieno, S. Scarsoglio, L. Gallana and F. Fraternali with whom I have worked well during the PhD.

I acknowledge the CTR Foundation and the Lagrange Project for granting my PhD scholarship.

Finally I want to thank my family for always supporting me.

# Bibliography

- [1] AMES, W. F. 1977 Numerical methods for partial differential equations. *Academic press*
- [2] ASAI, M. & FLORYAN, J. M. 2006 Experiments on the linear instability of flow in a wavy channel. *Eur. J. Mech. B/Fluids* **25**, 971–986.
- [3] AUGIER, P. & BILLANT, P. 2011 Onset of secondary instabilities on the zigzag instability in stratified fluids. *J. Fluid Mech.* **662**, 120–131.
- [4] AUGIER, P. CHOMAZ, J.M. & BILLANT, P. 2012 Spectral analysis of the transition to turbulence from a dipole in stratified fluid *J. Fluid Mech.* **713**, 86–108
- [5] BARKLEY, D. 2006 Linear analysis of the cylinder wake mean flow. *Europhys. Lett.* **75** 750–756.
- [6] BELAN, M. & TORDELLA, D. 2006 Convective instability in wake intermediate asymptotics. *J. Fluid Mech.* **552**, 127–136.
- [7] BENNEY, D. J. & GUSTAVSSON, L. H. 1981 A new mechanism for linear and non-linear hydrodynamic instability. *Stud. in Applied Math.* **64** (3), 185–209.
- [8] BERGSTRÖM, L. B. 2005 Nonmodal growth of three-dimensional disturbances on plane Couette-Poiseuille flows. *Phys. Fluids* **17**, 014105.
- [9] BERRONE, S., DE SANTI, F., PIERACCINI, S. & MARRO, M. 2012 Coupling traffic models on networks and urban dispersion models for simulating sustainable mobility strategies. *Comp. Mat. Appl.* **64**(6), 1975–1991.
- [10] BETCHOV, R. & CRIMINALE, W. O. 1967 Stability of parallel flows. *New York, Academic Press.*
- [11] BIAU, D. & BOTTARO, A. 2009 An optimal path to transition in a duct. *Phil. Trans. R. Soc. A* **367**, 529–544.
- [12] BILLANT, P. BRANCHER, P. & CHOMAZ, J.-M. 1999 Three-dimensional stability of a vortex pair. *Phys. Fluids* **11**, 20692077.
- [13] BILLANT, P. & CHOMAZ, J.-M. 2000 (a) Theoretical analysis of the zigzag instability of a vertical columnar vortex pair in a strongly stratified fluid. *J. Fluid Mech.* **419**, 29–63.
- [14] BILLANT, P. & CHOMAZ, J.-M. 2000 (b) Three-dimensional stability of a vertical columnar vortex pair in a stratified fluid. *J. Fluid Mech.* **419**, 65–91.

- [15] BILLANT, P. & CHOMAZ, J.-M. 2000 (c) Experimental evidence for a new instability of a vertical columnar vortex pair in a strongly stratified fluid. *J. Fluid Mech.* **418**, 167–188.
- [16] BILLANT, P. 2010 Zigzag instability of vortex pairs in stratified and rotating fluids. Part 1. General stability equations. *J. Fluid Mech.* **660**, 354–395.
- [17] BIONA, C.B., DRUILHET, A., BENECH, B. & LYRA, R. 2001 Diurnal cycle of temperature and wind fluctuations within an African equatorial rain forest. *Agric. Forest Meteor.* **109**(2), 135–141.
- [18] BODENSCHATZ, E., MALINOWSKI, S. P., SHAW, R. A., & STRATMANN, F. 2010 Can we understand clouds without turbulence?. *Science* **327**(5968), 970–971.
- [19] BOGACKI, P. & SHAMPINE, L. F. 1989 A 3(2) pair of Runge-Kutta formulas. *Appl. Math. Lett.* **2**, 1–9.
- [20] BREUER, K. S., KURAISHI, T. 1994 Transient growth in two and threedimensional boundary layers. *Phys. Fluids* **6**, 1983–1993.
- [21] BUTLER, K. M. & FARRELL, B. F. 1992 Three-dimensional optimal perturbations in viscous shear flow. *Phys. Fluids A* **4** (8), 1637–1650.
- [22] CERUTTI, S. & MENEVEAU, C. 2000 Statistics of filtered velocity in grid and wake turbulence. *Phys. Fluids* **12**, 1143–1165.
- [23] CHANDRASEKHAR, S. 1961 Hydrodynamic and Hydromagnetic Stability. *Oxford University Press*.
- [24] CHOMAZ, J. M., BONNETON, P., BUTET, A. & HOPFINGER, E. J. 1993 Vertical diffusion in the far wake of a sphere moving in a stratified fluid. *Phys. Fluids A* **5**, 2799–2806.
- [25] CHUNG, D. & MATHEOU, G. 2012 Direct numerical simulation of stationary homogeneous stratified sheared turbulence. *J. Fluid Mech.* **696** 434–467
- [26] COOKE, J. C. 1950 The boundary layer of a class of infinite yawed cylinders. *Proc. Camb. Phil. Soc.* **46**, 645–648.
- [27] CORBETT, P., BOTTARO, A. 2001 Optimal linear growth in swept boundary layers. *J. Fluid Mech.* **435**, 1–23.
- [28] CRIMINALE, W. O. & DRAZIN, P. G. 1990 The evolution of linearized perturbations of parallel shear flows. *Stud. Applied Math.* **83**, 123–157.
- [29] CRIMINALE, W. O., JACKSON, T. L., LASSEIGNE, D. G. & JOSLIN, R. D. 1997 Perturbation dynamics in viscous channel flows. *J. Fluid Mech.* **339**, 55–75.
- [30] CRIMINALE, W. O., JACKSON, T. L. & JOSLIN, R. D. 2003 *Theory and Computation in Hydrodynamic Stability*. Cambridge University Press.
- [31] CROW, S. C. 1970 Stability theory for a pair of trailing vortices. *AIAA J.* **8**, 2172–2178.
- [32] DE SANTI, F., SCARSOGLIO, S., CRIMINALE, W. O., & TORDELLA, D. 2015 Parametric perturbative study of the supercritical cross-flow boundary layer. *Int. J. Heat Fluid Flow* **52**, 64–71.

- [33] DELBENDE, I. & CHOMAZ, J. M. 1998 Nonlinear convective/absolute instabilities in parallel two-dimensional wakes. *Phys. Fluids* **10**, 2724–2736.
- [34] DELONCLE, A., CHOMAZ, J.-M. & AND BILLANT, P. 2007 Three-dimensional stability of a horizontally sheared flow in a stably stratified fluid. *J. Fluid Mech.* **570**, 297–305
- [35] DIPRIMA, R. C. & HABLETER, G. J. 1969 A completeness theorem for non-selfadjoint eigenvalue problems in hydrodynamic stability. *Archive for Rational Mechanics and Analysis* **34** 218–227
- [36] DRAZIN, P. G. 2002 *Introduction to hydrodynamic stability*. Cambridge, Cambridge University Press.
- [37] DUGUET, Y., BRANDT, L. & LARSSON, B. R. J. 2010 Towards minimal perturbations in transitional plane Couette flow. *Phys. Rev. E* **82**, 026316.
- [38] FAISST, H. & ECKHARDT, B. 2003 Traveling waves in pipe flow. *Phys. Rev. Lett.* **91**, 224502.
- [39] FINCHAM, A. M., MAXWORTHY, T. & SPEDDING, G. R. 1996 Energy dissipation and vortex structure in freely decaying stratified grid turbulence. *Dyn. Atmos. Oceans* **23**, 171–182.
- [40] FRATERNALE, F. 2013 Frequency transient of three-dimensional perturbations in shear flows. Similarity Properties and wave packets linear formation. *Politecnico di Torino, Master Thesis* Turin, March 2013.
- [41] FUKUMOTO, Y., & MIYAZAKI, T. 1991 Three-dimensional distortions of a vortex filament with axial velocity. *J. Fluid Mech.* **222**, 369–416.
- [42] GALLANA, L., DI SAVINO, S., DE SANTI, F., IOVIENO, M. & TORDELLA, D. 2014 Energy and water vapor transport across a simplified cloud - clear air interface. *J. Phys.: Conf. Ser.* **547**, 012042.
- [43] GERBER, H., FRICK, G., MALINOWSKI, SZYMON P., JONSSON, H., KHELIF, D. & KRUEGER, STEVEN K. 2013 Entrainment rates and microphysics in POST stratocumulus. *J. Geophys. Res. D* **118**(21), 12094–12109
- [44] GIANNETTI, F. & LUCHINI, P. 2007 Structural sensitivity of the first instability of the cylinder wake. *J. Fluid Mech.* **581** 167–197
- [45] GILL, A. E. 1982 *Atmosphere-ocean dynamics*. Academic Press, New York.
- [46] GREGG, M. C. 1987 Diapycnal mixing in the thermocline: a review. *J. Geophys. Res.* **92**, 5249–5286.
- [47] GREGORY, N., STUART, J. T., & WALKER, W. S. 1955 On the stability of three-dimensional boundary layers with application to the flow due to a rotating disk. *Philosophical Transactions of the Royal Society of London. Series A, Mathematical and Physical Sciences*, 155–199.
- [48] GROSCH, C. E., SALWEN, H. 1978 The continuous spectrum of the Orr-Sommerfeld equation. Part 1. The spectrum and the eigenfunctions. *J. Fluid Mech.* **87** 33–54
- [49] GUSTAVSSON, L.H. 1979 Initial-value problem for boundary layer flows. *Phys. Fluids* **22** (9), 1602-1605.

- [50] GUSTAVSSON, L.H. & HULTGREN, L.S. 1980 A resonance mechanism in plane Couette flow. *J. Fluid Mech.* **98**, 149-159.
- [51] GUSTAVSSON, L.H. 1981 Resonant growth of three-dimensional disturbances in plane Poiseuille flow. *J. Fluid Mech.* **112**, 253-26.
- [52] GUSTAVSSON, L. H. 1991 Energy growth of three-dimensional disturbances in plane Poiseuille flow. *J. Fluid Mech.* **224**, 241-260.
- [53] HEALY, J. J. 2006 A new convective instability of the rotating-disk boundary layer with growth normal to the disk. *J. Fluid Mech.* **560**, 279-310.
- [54] HELMHOLTZ, H. 1868 U ber discontinuirliche Flussigkeits-Bewegungen. Akad. Wiss., Berlin, *Monatsber.* **23**, 215-228. Translated by F. Guthrie, On discontinuous movements of fluids. *Phil. Mag.* **36** (4), 337-346.
- [55] HENNINGSON, D. S., LUNDBLADH, A. & JOHANSSON, A. V. 1993 A mechanism for bypass transition from localized disturbances in wall-bounded shear flows. *J. Fluid Mech.* **250**, 169-207.
- [56] HERRING, J. R. & MÉTAIS, O. 1989 Numerical simulations in forced stably stratified turbulence. *Ann. Rev. Fluid Mech.* **202**, 97-115.
- [57] HOF, B., VAN DOORNE, C. W. H., WESTERWEEL, J., NIEUWSTADT, F. T. M., FAISST, H., ECKHARDT, B., WEDIN, H., KERSWELL, R. R. & WALEFFE, F. 2004 Experimental observation of nonlinear traveling waves in turbulent pipe flow. *Science* **305**, 1594-1598.
- [58] HOWARD, L. N. 1961 Note on a paper of John W. Miles. *J. Fluid Mech* **10**(4), 509-512.  
in a laminar boundary layer. *Phys. Fluids* **24** (6), 1000-1004.
- [59] IOVIENO, M., CAVAZZONI, C. & TORDELLA, D. 2001 A new technique for a parallel dealiased pseudospectral Navier-Stokes code. *Comp.Phys.Comm.* **141**, 365-374.
- [60] IOVIENO, M., DI SAVINO, S., GALLANA, L. & TORDELLA, D. 2014 Mixing of a passive scalar across a thin shearless layer: concentration of intermittency on the sides of the turbulent interface. *J. Turb* **15**(5), 311-334.
- [61] ITO, N. 1974 *Trans. Japan Soc. Aero. Space Sci.* **17**, 65.
- [62] KATUL, G.G., GERON, C.D., HSIEH, C.I., VIDAKOVIC, B. & GUENTHER, A.B. 1998 Active turbulence and scalar transport near the forest-atmosphere interface. *J. Appl. Meteor.* **37**(12), 1533-1546.
- [63] KELVIN, LORD 1880 Vibrations of a columnar vortex. *Phil. Mag.* **10** (5), 155-168.
- [64] KELVIN LORD 1887a Rectilinear motion of viscous fluid between two parallel plates. *Math and Phys. Papers* **4**, 321-330.
- [65] KELVIN LORD 1887b Broad river flowing down an inclined plane bed. *Math. and Phys. Papers* **4**, 330-337.
- [66] KERR, R. M. 1985 Higher-order derivative correlations and the alignment of small-scale structures in isotropic numerical turbulence. *J. Fluid Mech.* **153**, 31-58.

- [67] KERR, R.M, DE SANTI, F., TORDELLA, D. & PARMAR A. 2012 Stratified zig-zags on vortex pairs using vertically shifted perturbations. **XXIII ICTAM**.
- [68] KERR, R. M. 2011 Vortex stretching as a mechanism for quantum kinetic energy decay. *Phys. rev. let.* **106**(22), 224501.
- [69] KERSWELL, R. R. 2002 Elliptical instability. *Annu. Rev. Fluid Mech.* **34**, 83-113.
- [70] KIMURA, Y. & HERRING, J. R. 1996 Diffusion in stably stratified turbulence. *Ann. Rev. Fluid Mech.* **328**, 253-269.
- [71] KOCH, W. 2002 On the spatio-temporal stability of primary and secondary crossflow vortices in a three-dimensional boundary layer. *J. Fluid Mech.* **456**,85-111.
- [72] LAPORTE, F. & CORJON, A. 2000 Direct numerical simulations of the elliptic instability of a vortex pair. *Phys. Fluids* **12**, 1016-1031.
- [73] LASSEIGNE, D. G., JOSLIN, R. D., JACKSON, T. L. & CRIMINALE, W. O. 1999 The transient period for boundary layer disturbances. *J. Fluid Mech.* **381**, 89-119.
- [74] LILLY, D. K. 1983 Stratified turbulence and the mesoscale variability of the atmosphere. *J. Atmos. Sci.* **40**, 749-761.
- [75] LIN, J. T. & PAO, Y. H. 1979 Wakes in stratified fluids: a review. *Ann. Rev. Fluid Mech.* **11**, 317-338.
- [76] LINDBORG, E. 2006 The energy cascade in a strongly stratified fluid. *J. Fluid Mech.* **550**, 207-242.
- [77] LINGWOOD, R. J. 1995 Absolute instability of the boundary layer on a rotating disk. *J. Fluid Mech.* **299**, 17-17.
- [78] LINGWOOD, R. J. 1997 Absolute instability of the Ekman layer and related rotating flows. *J. Fluid Mech.* **331**, 405-428.
- [79] LOTHON, M., LENSCHOW, D. H. & MAYOR, S. D. 2009 Doppler Lidar Measurements of Vertical Velocity Spectra in the Convective Planetary Boundary Layer. *Bound. Lay. Meteor.* **132**(2), 205-226.
- [80] LUCHINI, P. 1996 Reynolds-number-independent instability of the boundary layer over a flat surface. *J. Fluid Mech.* **327**, 101-115.
- [81] LUCHINI, P. & BOTTARO, A. 1998 Görtler vortices: a backward-in-time approach to the receptivity problem. *J. Fluid Mech.* **363**, 1-23.
- [82] LUCHINI, P. 2000 Reynolds-number-independent instability of the boundary layer over a flat surface: optimal perturbations. *J. Fluid Mech.* **404**(1), 289-309.
- [83] LUNDGREN, T. S. 1982 Strained spiral vortex model for turbulent fine structure. *Phys. Fluids* **25**(12), 2193-2203.
- [84] MA, B.K. & WARHAFT, Z. 1986 Some aspects of the thermal mixing layer in grid turbulence. *Phys. Fluids* **29**(10), 3114-3120.
- [85] MACK, L. M. 1976 A numerical study of the temporal eigenvalue spectrum of the Blasius boundary layer. *J. Fluid Mech.* **73**, 497-520.

- [86] MALIK, M. R., LI, F. & CHANG, C.-L. 1994 Crossflow disturbances in three-dimensional boundary layers: nonlinear development, wave interaction and secondary instability. *J. Fluid Mech.* **268**, 1–36
- [87] MALIK, M. R., LI, F. & CHANG, C.-L. 1999 Secondary instability of crossflow vortices and swept-wing boundary-layer transition. *J. Fluid Mech.* **399** 85–115
- [88] MALINOWSKI, S. P., GERBER, H., JEN-LA PLANTE, I., KOPEC, M. K., KUMALA, W., NUROWSKA, K., CHUANG, P. Y., KHELIF, D. & HAMAN, K. E. 2013 Physics of Stratocumulus Top (POST): turbulent mixing across capping inversion. *Atmos. Chem. Phys.*, **13**(24) 12171–12186.
- [89] MARAIS, C., GODOY-DIANA, R., BARKLEY, D. & WESFREID, J. E. 2011 Convective instability in inhomogeneous media: Impulse response in the subcritical cylinder wake. *Phys. Fluids* **23**, 014104.
- [90] MELLADO, J. P. 2010 The evaporatively driven cloud-top mixing layer. *J. Fluid Mech.* **660** 5–36.
- [91] MELLADO, J. P., STEVENS, B. & SCHMIDT, H. 2014 Wind Shear and Buoyancy Reversal at the Top of Stratocumulus. *J. Atmos. Sci* **71**(3), 1040–1057.
- [92] MÉTAIS, O. & HERRING, J. R. 1989 Numerical simulations of freely evolving turbulence in stably stratified fluids. *J. Fluid Mech.* **202**, 117–148.
- [93] MIKLAVCIC, M. & WILLIAMS, M. 1982 Stability of mean flows over an infinite flat plate. *Arch. Rational Mech. Anal.* **80**, 57–69.
- [94] MIKLAVCIC, M. 1983 Eigenvalues of the Orr-Sommerfeld equation in an unbounded domain. *Arch. Rational Mech. Anal.* **83**, 221–228.
- [95] MILES, J. W. 1961 On the stability of heterogeneous shear flows. *J. Fluid Mech.* **10**(04), 496–508.
- [96] MOENG, C.H. 1986 Large-eddy simulation of a stratus-topped boundary layer. *J. Atmos. Sci.* **43**, 2886–2900.
- [97] MOENG, C.H., COTTON, W.R., BRETHERTON, C., CHLOND, A., KHAIROUTDINOV, M., KRUEGER, S., LEWELLEN, W.S., MACVEAN, M.K., PASQUIER, J.R.M., RAND, H.A., SIEBESMA, A.P., STEVENS, B. & SYKES, R.I. 1996 Simulation of a stratocumulus-topped planetary boundary layer: Intercomparison among different numerical codes. *Bull. Am. Meteorol. Soc.* **77**(2), 261–278.
- [98] MOENG, C.H. 2000 Entrainment rate, cloud fraction, and liquid water path of PBL stratocumulus clouds. *J. Atmos. Sci.* **57**, 3627–3643.
- [99] MOSER, R. D., KIM, J., & MANSOUR, N. N. 1999 Direct numerical simulation of turbulent channel flow up to  $Re = 590$ . *Phys. Fluids* **11**, 943–945.
- [100] NAGLE, G., & GUINNESS, P. 2013 Cambridge International A and AS Level *Geography Revision Guide ePub*. Hachette UK.
- [101] NAKAMURA, H., NAKAMURA, M. & ANDERSON, J. L. 1997 The role of high- and low-frequency dynamics in blocking formation. *Mon. Weather Rev.* **125**, 2074–2093.

- [102] NASTROM, G. D. & GAGE, K. S. 1985 A climatology of atmospheric wavenumber spectra of wind and temperature observed by commercial aircraft. *J. Atmos. Sci.* **42**, 950-960.
- [103] NISHIOKA, M., IIDA, S. & ICHIKAWA, Y. 1975 An experimental investigation of the stability of plane Poiseuille flow. *J. Fluid Mech.* **72**, 731-751.
- [104] NISHIOKA, M. & SATO, H. 1974 Measurements of velocity distributions in the wake of a circular cylinder at low Reynolds numbers. *J. Fluid Mech.* **65** 97-112
- [105] NORBERG, C. 1994 An experimental study of the flow around a circular cylinder: Influence of aspect ratio. *J. Fluid Mech.* **258** 287-316
- [106] ONG, L. & WALLACE, J. 1996 The Velocity Field of the Turbulent Very Near Wake of a Circular Cylinder. *Exp. Fluids* **20**, 441-453.
- [107] ORR, W. M'F. 1907 a The stability or instability of the steady motions of a perfect liquid and a viscous liquid. Part I *Proc. R. Irish. Acad.* **27**, 9-68.
- [108] ORR, W. M'F. 1907 b The stability or instability of the steady motions of a perfect liquid and a viscous liquid. Part II *Proc. R. Irish. Acad.* **27**, 69-138.
- [109] PARANTHOËN, P., BROWNE, L.W.B., LEMASSON, S., LEMASSON, F. & LECORDIE, J.C 1999 Characteristics of the near wake of a cylinder at low Reynolds numbers. *Eur. J. Mech. B/Fluids* **18** 659-674
- [110] PIER, B. 2002 On the frequency selection of finite-amplitude vortex shedding in the cylinder wake. *J. Fluid Mech.* **458** 407-417
- [111] PIER, B. 2003 Finite-amplitude crossflow vortices, secondary instability and transition in the rotating-disk boundary layer. *J. Fluid Mech.* **487**, 315-343.
- [112] QIU, X., HUANG, Y., LU, Z. & LIU, Y. 2009 Large eddy simulation of turbulent statistical and transport properties in stably stratified flows. *App. Mat. and Mech* **30**(2), 153-162.
- [113] RADKEVICH, A., LOVEJOY, S., STRAWBRIDGE, K. B., SCHERTZER, D. & LILLEY, M. 2008 Scaling turbulent atmospheric stratification. III: Space-time stratification of passive scalars from lidar data. *Quart. J. Roy. Meteor. Soc.* **134**(631, B), 317-335.
- [114] RAYLEIGH, LORD 1880 On the stability or instability of certain fluid motions. *Proc. London Math. Soc.* **11**, 57-70. Also, *Scientific Papers* **1**, 474-487, 1899.
- [115] REDDY, S. C. & HENNINGSON, D. S. 1993 Energy growth in viscous channel flows. *J. Fluid Mech.* **252**, 209-238.
- [116] RILEY, J. J., METCALFE, R. W., & WEISSMAN, M. A. 1981 Direct numerical simulations of homogeneous turbulence in densitystratified fluids. In *Proc. AIP Conf. Non-linear Properties of Internal Waves* (ed. B. J. West). **76** 79-112.
- [117] RILEY, J. J. & DE BRUYN KOPS, S. M. 2003 Dynamics of turbulence strongly influenced by buoyancy. *Phys. Fluids* **15**(7), 20472059.
- [118] ROSHKO, A. 1954 On the Development of Turbulent Wakes from Vortex Streets. *NACA* 1932



- [119] SADDOUGH, S. G. & VEERAVALLI, S. V. 1994 Local isotropy in turbulent boundary layers at high Reynolds number. *J. Fluid Mech.* **268**, 333–372.
- [120] SALWEN, H. & GROSCH, C. E. 1981 The continuous spectrum of the Orr-Sommerfeld equation. Part 2. Eigenfunction expansions. *J. Fluid Mech.* **104**, 445–465.
- [121] SARIC, W. S., REED, H. L., WHITE, E. B. 2003 Stability and transition of three-dimensional boundary layers. *Annu. Rev. Fluid Mech.* **35**, 413–440.
- [122] SCARSOGLIO, S., TORDELLA, D. & CRIMINALE, W. O. 2009 An Exploratory Analysis of the Transient and Long-Term Behavior of Small Three-Dimensional Perturbations in the Circular Cylinder Wake. *Stud. Applied Math.* **123**, 153–173.
- [123] SCARSOGLIO, S., TORDELLA, D. & CRIMINALE, W. O. 2010 Role of long waves in the stability of the plane wake. *Phys. Rev. E* **81**, 036326.
- [124] SCHLICHTING, H. 1979 Boundary layer theory, 7<sup>th</sup> Edn. *McGraw-Hill*
- [125] SCHMID, P. J. & HENNINGSON, D. S. 2001 *Stability and Transition in Shear Flows*. Springer.
- [126] SCHRADER, L., BRANDT, L., HENNINGSON, D. S. 2009 Receptivity mechanisms in three-dimensional boundary-layer flows. *J. Fluid Mech.* **618**, 209–241.
- [127] SHAMPINE, L. F. & REICHEL, M. W. 1997 The MATLAB ODE Suite *SIAM J. Sci. Comput.* **18**, 1–22.
- [128] SOMMERFELD, A. 1908 Ein beitraz zur hydrodynamischen erklærung der turbulenten fluessigkeitsbewegungen. *Proc. Fourth Inter. Congr. Matematicians*, Rome, 116–124.
- [129] SQUIRE, H. B. 1933 On the stability for three-dimensional disturbances of viscous fluid flow between parallel walls. *Proc. Roy. Soc., Series A. Mathematical and Physical Sciences* **142**, 621–628.
- [130] STRYKOWSKI, P. J. & SREENIVASAN, K. R. 1990 On the formation and suppression of vortex shedding at low Reynolds numbers. *J. Fluid Mech.* **218**, 71–107.
- [131] SWANSON, K. L. 2002 Dynamical aspects of extratropical tropospheric low-frequency variability. *J. Climate* **15**, 2145–2162.
- [132] SYKES, R.I., LEWELLEN, W.S. & HENN, D.S. 1990 Numerical simulations of the boundary-layer eddy structure during the cold-air outbreak of GALE IOP 2. *Mon. Wea. Rev.* **118**, 363–373.
- [133] TAYLOR, B. J., PEAK, N. 1998 The long-time behaviour of incompressible swept-wing boundary layers subject to impulsive forcing. *J. Fluid Mech.* **355**, 359–38.
- [134] TEMPELMANN, D., HANIFI, A., HENNINGSON, D. S. 2010 Spatial optimal growth in three-dimensional boundary layers. *J. Fluid Mech.* **646**, 5–37.
- [135] THOMAS, P. J. & AUERBACH, D. 1994 The observation of the simultaneous development of a long and a short-wave instability mode on a vortex pair. *J. Fluid Mech.* **265**, 289–302.
- [136] TORDELLA, D. & BELAN, M. 2003 A new matched asymptotic expansion for the intermediate and far flow behind a finite body. *Phys. Fluids* **15**, 1897–1906

- [137] TORDELLA, D., SCARSOGLIO, S. & BELAN, M. 2006 A synthetic perturbative hypothesis for multiscale analysis of convective wake instability. *Phys. Fluids* **18** (5), 054105.
- [138] TORDELLA D. & IOVIENO, M. 2006 Numerical experiments on the intermediate asymptotics of shear-free turbulent transport and diffusion. *J.Fluid Mech.* **549**, 429–441 (2006)
- [139] TORDELLA, D. & IOVIENO M. 2011 Small scale anisotropy in the turbulent shearless mixings. *Phys. Rev. Lett.* **107**, 194501.
- [140] TORDELLA D. & IOVIENO, M. 2011 Small scale anisotropy in turbulent shearless mixing. *Phys. Rev. Letters* **107**, 194501
- [141] TORDELLA, D., IOVIENO, M. BAILEY P.R. 2008 A sufficient condition for Gaussian departure in turbulence. *Phys.Rev.E* **77**, 016309
- [142] TSINOBER, A. 2000 Vortex stretching versus production of strain/dissipation. *Proc: Turbulence Structure and Vortex Dynamics*, 164–191.
- [143] VALLIS, G. K. 2006 Atmospheric and Oceanic Fluid Dynamics: Fundamentals and Large-scale Circulation; electronic version. *Leiden: Cambridge Univ. Press.*
- [144] VEERAVALLI, S. & WARHAFT, Z. 1989 The shearless turbulence mixing layer. *J. Fluid Mech.* **207** 191–229.
- [145] WAITE, M. L. & P. K. SMOLARKIEWICZ 2008 Instability and breakdown of a vertical vortex pair in a strongly stratified fluid. *J. Fluid Mech.* **606**, 239–273.
- [146] WALEFFE, F. 1990 On the three-dimensional instability of strained vortices. *Phys. Fluids A* **2**, 76-80.
- [147] WATSON, J. 1960 On the non-linear mechanics of wave disturbances in stable and unstable parallel flows. Part 2. The development of a solution for plane Poiseuille flow and for plane Couette flow. *J. Fluid Mech.* **9**, 371-389.
- [148] WILLIAMSON, C. H. K. 1989 Oblique and parallel modes of vortex shedding in the wake of a circular cylinder at low Reynolds numbers. *J. Fluid Mech.* **206**, 579–627.
- [149] WOOD, R. 2012 Stratocumulus Clouds. *Mon. Weather Rev.* **8**, 2373–2423
- [150] ZEBIB, A. 1987 Stability of viscous flow past a circular cylinder. *J. Engng Maths*, **21** 155–165.